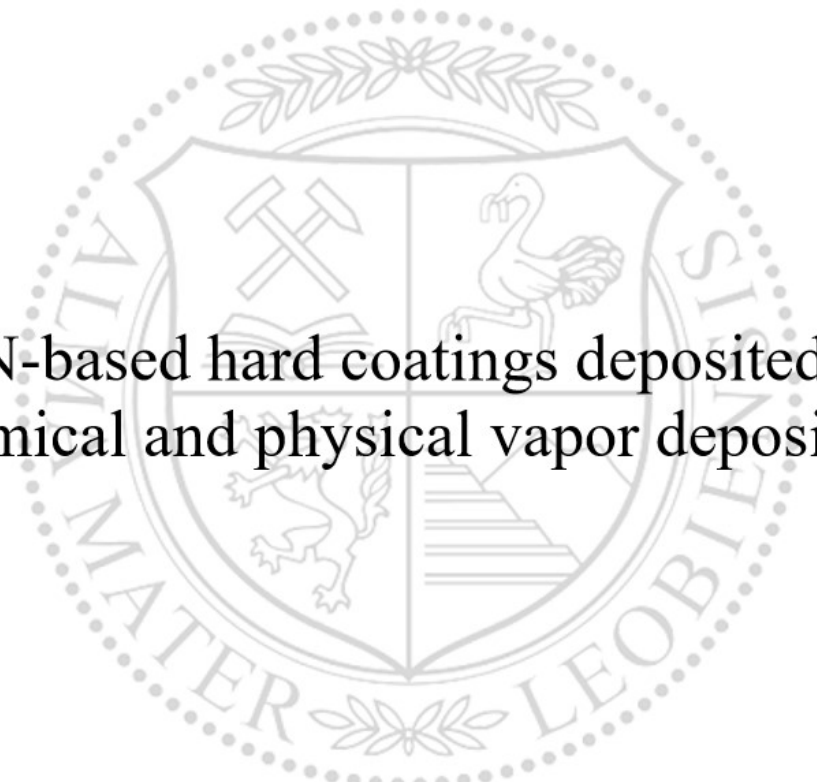Chair of Functional Materials and Materials Systems

Doctoral Thesis

ZrN-based hard coatings deposited by chemical and physical vapor deposition

Florian Frank, BSc MSc

July 2022

AFFIDAVIT

I declare on oath that I wrote this thesis independently, did not use other than the specified sources and aids, and did not otherwise use any unauthorized aids.

I declare that I have read, understood, and complied with the guidelines of the senate of the Montanuniversität Leoben for "Good Scientific Practice".

Furthermore, I declare that the electronic and printed version of the submitted thesis are identical, both, formally and with regard to content.

Date 29.07.2022

Signature Author
Florian Frank

Acknowledgments

First of all, I would like to express my sincerest gratitude to my supervisor Priv.-Doz. Dr. Nina Schalk for giving me the opportunity to work within the Christian Doppler Laboratory for advanced coated cutting tools and for her continuous guidance, patience, advice, motivation, support, and especially for the always honest feedback correcting my drafts during my time at the university. Furthermore, I would like to thank Prof. Dr. Christian Mitterer for the possibility to conduct the present thesis in the research group at the Department of Materials Science at the Montanuniversität Leoben.

I also would like to thank especially Dr. Michael Tkadletz and Dr. Christian Saringer for the countless discussions, insightful feedback and profound assistance with all kinds of advanced investigation and evaluation methods, as well as for always putting in their two cents when correcting my drafts. This work would not be the same without their contributions!

I would like to thank Assoc. Prof. Dr. Daniel Kiener for being my mentor for this thesis. Furthermore, I want to thank Prof. Dr. Jozef Keckes for giving me the opportunity to perform exciting experiments at the synchrotron facility.

Special thanks go to Dr. Christoph Czettl and Dr. Markus Pohler from CERATIZIT Austria GmbH, for providing a pleasant working atmosphere and for the fruitful discussions during our meetings.

I want to thank all my colleagues at the Chair of Functional Materials for providing a great working atmosphere and for all valuable discussions. Especially I want to thank my coworkers Dr. Christina Kainz, Helene Waldl and Fabian Konstantiniuk. It was a pleasure and great fun working with you all!

I also want to thank my family for their great support during my PhD thesis. Without their assistance, I would not be where I am today.

Last but not least, I want to thank the most important person in my life, my fiancée Yvonne. Thank you for your constant support, encouraging words, calming me during

stressful times, for your extraordinary scientific expertise and discussions that greatly benefit this work and, above all things, for your love! I love you $\lim\limits_{n\to\infty} \heartsuit^n$.

"The task is not to see what has never been seen before, but to think what has never been thought before about what you see everyday."

Arthur Schopenhauer

Abstract

Hard coatings have been widely used for several decades to enhance the performance and efficiency of cemented carbide cutting tools in machining applications. The requirements for these coatings are a high hardness and wear resistance, as well as a good thermal stability and oxidation resistance. Chemical and physical vapor deposition (CVD and PVD) are common methods to deposit these coatings.

The goal of this work is the development of ZrN-based hard coatings and the in-depth characterization of their microstructure, mechanical properties and thermal properties. In order to enhance the coating properties different approaches were applied. In the first approach, the influence of the addition of C to CVD ZrN on the mentioned properties was investigated. It was found that the hardness increases for coatings containing C, which can be attributed to grain refinement and stronger covalent bonding. A detailed investigation of the oxidation behavior with in-situ high-temperature synchrotron X-ray diffraction showed that the presence of C increases the oxidation stability, where the $ZrC_{0.4}N_{0.6}$ coating showed the highest oxidation onset temperature of ~570 °C. The higher oxidation resistance in $ZrC_{0.4}N_{0.6}$ and ZrC compared to ZrN can be attributed to the stabilization of the cubic and/or tetragonal ZrO_2 phase by residual amorphous C and a smaller grain size.

In the second approach, ZrN/Ti(Al)N multilayer coatings were deposited with PVD and the influence of the bilayer thickness on the microstructure and mechanical properties was investigated. Firstly, ZrN/TiN multilayer coatings with different bilayer thickness, as well as ZrN and TiN single-layer coatings were studied. It was found that the multilayer architecture increases the hardness, as well as the fracture stress compared to the single-layer coatings. Secondly, the microstructure and residual stress of a graded ZrN/$Ti_{0.33}Al_{0.67}N$ coating with constant $Ti_{0.33}Al_{0.67}N$ and stepwise increasing ZrN individual layer thickness was investigated in detail using position resolved cross-sectional X-ray nanodiffraction. A (semi-)coherent layer growth and an increasing grain

size, as well as a decreasing compressive residual stress state with increasing ZrN layer thickness was observed.

To summarize, this thesis highlights several approaches to enhance the properties of CVD and PVD ZrN-based coatings. Furthermore, the importance of advanced high-resolution in-situ and position resolved investigation methods for the characterization of hard coatings is emphasized, which contribute to a deeper understanding of the deposition-structure-property relation of ZrN-based hard coatings.

Kurzfassung

Hartstoffschichten werden seit mehreren Jahrzehnten verwendet, um die Leistungsfähigkeit und Effizienz von Hartmetall-Schneidwerkzeugen für Zerspanungsanwendungen zu verbessern. Die Anforderungen an diese Schichten sind sowohl eine hohe Härte und Verschleißbeständigkeit, als auch eine gute thermische Stabilität und Oxidationsbeständigkeit. Chemische- und physikalische Gasphasenabscheidung (englisch Chemical Vapor Deposition, CVD und Physical Vapor Deposition, PVD) sind häufig verwendete Methoden, um diese Hartstoffschichten abzuscheiden.

Das Ziel dieser Arbeit ist die Entwicklung von ZrN basierten Hartstoffschichten und die fundamentale Untersuchung ihrer Mikrostruktur, der mechanischen- und thermischen Eigenschaften. Um die Schichteigenschaften zu verbessern, wurden verschiedene Ansätze angewandt. Im ersten Ansatz wurde der Einfluss der Zugabe von C zu CVD ZrN auf die Schichteigenschaften untersucht. Es konnte gezeigt werden, dass die Härte der Schichten mit C Anteil steigt, was auf eine kleinere Korngröße und einen stärkeren Anteil kovalenter Bindungen zurückgeführt werden kann. Eine detaillierte Untersuchung des Oxidationsverhaltens mittels in-situ Hochtemperatur Synchrotron-Röntgendiffraktion hat gezeigt, dass das Vorliegen von C in den Schichten die Oxidationsstabilität erhöht, wobei $ZrC_{0.4}N_{0.6}$ den höchsten Beginn der Oxidation bei einer Temperatur von ~570 °C aufwies. Die höhere Oxidationsbeständigkeit von $ZrC_{0.4}N_{0.6}$ und ZrC gegenüber ZrN kann auf eine Stabilisierung der kubischen und/oder tetragonalen ZrO_2 Phase durch amorphen C und eine kleinere Korngröße zurückgeführt werden.

Im zweiten Ansatz wurden ZrN/Ti(Al)N Multilagenschichten mittels PVD abgeschieden und der Einfluss der Lagendicken auf die Mikrostruktur und die mechanischen Eigenschaften untersucht. Zuerst wurden ZrN/TiN Multilagenschichten mit unterschiedlichen Lagendicken, sowie ZrN und TiN Einzellagenschichten untersucht. Es hat sich gezeigt, dass die Multilagenarchitektur im Vergleich zu den

Einzellagenschichten die Härte sowie die Bruchfestigkeit erhöht. Zweitens wurde die Mikrostruktur und die Eigenspannungen einer gradierten ZrN/TiAlN Multilagenschicht mit konstanter TiAlN und schrittweise größer werdender ZrN Einzellagendicke detailliert mittels positionsaufgelöster Querschnitts-Röntgen-Nanodiffraktion untersucht. Die Schicht wies (semi-)kohärentes Lagenwachstum und eine größer werdende Korngröße sowie sinkende Druckeigenspannungen mit zunehmender ZrN Einzellagendicke auf.

Zusammenfassend hebt diese Doktorarbeit etliche Ansätze hervor, um die Eigenschaften von CVD und PVD ZrN basierten Schichten zu verbessern. Außerdem wird die Bedeutung von fortschrittlichen hochauflösenden in-situ und positionsaufgelösten Charakterisierungsmethoden für die Untersuchung von Hartstoffschichten hervorgehoben, welche zu einem tieferen Verständnis der Beschichtungs-Struktur-Eigenschaften Beziehung von ZrN basierten Hartstoffschichten beiträgt.

Content

1 Introduction

Hard and wear resistant coatings are frequently used to enhance the performance and lifetime of cutting tools for different machining applications [1,2]. The coatings usually exhibit a thickness of a few μm and are typically deposited by chemical or physical vapor deposition (CVD or PVD) methods.

Different coating materials can be used, depending on the destined application. Probably the most well-known and intensively investigated hard coating material is TiN. It can be synthesized using CVD or PVD and has been used for several decades owing to its combination of good mechanical properties and decent thermal properties [3–9]. However, due to the ever increasing demands of the cutting industry towards higher performance and production throughput, as well as towards cost efficiency and lower energy consumption of the machining tools, new materials have to be explored to meet these requirements. One alternative to TiN is ZrN, which shows comparable mechanical properties, while exhibiting a higher oxidation resistance, as well as a lower surface roughness and electrical resistivity [7–15].

The properties of the binary transition metal nitride coatings can be further increased by addition of different alloying elements to form ternary coatings such as $ZrC_{1-x}N_x$, $TiC_{1-x}N_x$ or $Ti_{1-x}Al_xN$. $TiC_{1-x}N_x$ is commonly deposited in a multilayer approach using CVD, where it provides mechanical support under an Al_2O_3 top layer [16–18]. However, one drawback of this coating system is the formation of thermal cracks during cooling down to room temperature after the deposition at high temperatures of up to 1000 °C [19]. Recent reports suggest that $ZrC_{1-x}N_x$ is a good alternative to $TiC_{1-x}N_x$, as it reduces the formation of micro-cracks after the deposition process and shows better performance under cyclic thermo-mechanical loads, as well as in micromechanical investigations [17,20–22].

Another way to enhance the properties of protective hard coatings is by combining two or more different materials in a multilayer approach [23–26]. By adjusting the layer

architecture, e.g. number of bilayers and the individual layer thickness, the microstructure, mechanical and fracture properties can be adjusted to achieve the optimum performance of the cutting tools [25,27,28], which is accomplished by interfaces between the different layer constituents that prevent dislocation motion or lead to crack deflection [29–31]. Additionally, coherency stress and strain fields that develop mainly in multilayer coatings that exhibit coherent growth, also contribute to an improvement of these properties [26,32–36].

The aim of this thesis is the further development and detailed characterization of ZrN-based hard coatings for industrial machining applications. Hereby, the focus was laid on the exploration of ternary $ZrC_{1-x}N_x$ coatings, as well as multilayer coatings with a combination of ZrN and $Ti_{1-x}Al_xN$ layers. Thus, within publication I of this thesis, CVD $ZrC_{1-x}N_x$ coatings are investigated regarding their microstructure and mechanical properties. Furthermore, the oxidation behavior is studied in detail using in-situ synchrotron X-ray diffraction in publication II. Publication III and IV deal with the influence of the bilayer thickness on the coating properties, whereby special emphasis is laid on the fracture behavior, as well as the residual stress state of the coatings. In particular, in publication III the microstructure, mechanical properties and the fracture behavior of PVD ZrN/TiN coatings with different layer architectures are determined. In publication IV, the microstructure of a graded PVD $ZrN/Ti_{0.33}Al_{0.67}N$ multilayer coating with stepwise increasing ZrN and constant TiAlN layer thickness is investigated using cross-sectional X-ray nanodiffraction to assess the influence of the coating architecture on the microstructure, texture and especially the residual stress state.

2 Coating deposition

Hard coatings are commonly synthesized applying either chemical vapor deposition (CVD) or physical vapor deposition (PVD). For both, CVD and PVD, the deposition process can be described in three steps. The first step is the formation of vapor of the depositing species. In the second step, the vapor is transported from the source towards the substrate (e.g. cutting tool) and in the third step, the vapor is deposited on the substrate, leading to the coating nucleation and growth. The most common PVD processes used for the deposition of hard coatings are sputter deposition and cathodic arc evaporation (CAE) [37]. As the coatings in this work were synthesized by thermally activated CVD and by CAE, these two deposition methods will be described in more detail in the following.

2.1 Chemical vapor deposition

In CVD, solid coatings are formed due to the reaction of volatile precursors at the substrate surface, a process which takes place in a reaction chamber. The precursors can be present in solid, liquid or gaseous form at room temperature and ambient pressure and have to be transferred to the vapor phase upon introduction into the reaction chamber [38]. For example, solid precursors (e.g. Al, Zr, Hf) are commonly chlorinated in external reactors to form halide precursor gases (e.g. $AlCl_3$, $ZrCl_4$ and $HfCl_4$), which are then transferred into the main reaction chamber. The reaction of the precursors is mostly thermally activated and for the deposition of hard coatings usually hot-wall CVD plants are used [39]. In hot-wall CVD, the walls of the deposition plant are heated, whereby the substrates and the feed gas of the deposition plant are heated indirectly. In contrast, in cold-wall CVD the substrates are heated inductively or by lasers and the reaction chamber wall is not heated [1,39,40]. Typical temperatures for deposition of hard coatings using thermally activated CVD are in the range of 700-1100 °C. In addition to thermal activation, surface reactions can also be activated kinetically by plasma or microwaves. By the

combination of thermal and kinetically activated CVD, the deposition temperature can be lowered and the deposition rates can be increased [40,41].

The main steps for the formation of coatings in the CVD process are illustrated in Fig. 1 [41]. Besides the deposition temperature, the deposition pressure is an important process parameter that influences not only the gas stream velocities and thus, the residence times of the precursor gases in the reactor, but also the boundary-layer thickness, which determines the precursor diffusion to the substrate surface [1,39–41]. While the boundary-layer thickness increases with increasing pressure and temperature, the gas velocity decreases. At high deposition temperature, high pressure and low gas velocity, the boundary layer is thick and the diffusion of the reactants towards the substrate is low. At these conditions, reactions can occur in the gas phase, forming undesired powder through a homogeneous gas phase reaction. The deposition rate is limited by the mass transport to the surface. Due to the high thermal energy, reactions occur instantly when the gas molecules reach the surface. If the deposition temperature and pressure are low and the gas velocity is high, the boundary layer is thin. Due to the lower thermal energy, a homogeneous gas phase reaction is less likely and the reactants diffuse through the boundary layer towards the substrate and adsorption at the surface occurs. Chemical reactions occur at the substrate surface leading to nucleation and coating growth. However, due to the lower thermal energy, reactions may not occur on the surface, leading to desorption of the molecules. Therefore, the deposition rate is determined by surface kinetics. The deposition in the surface kinetics controlled regime is usually favored over the mass transport regime, as it results in more uniform deposition within the whole deposition chamber. Finally, desorption of the by-products occurs, which are then exhausted from the deposition chamber [1,39–41].
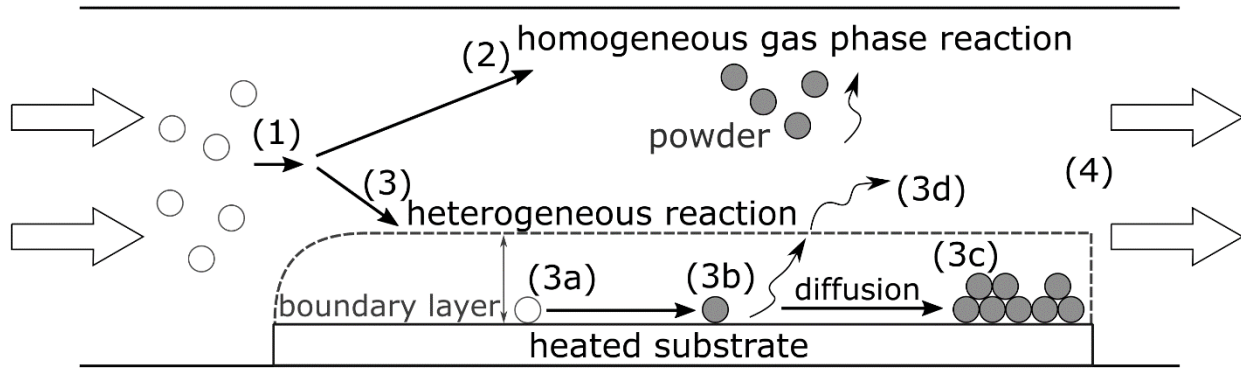
Fig. 1: Schematic illustration of the basic steps for chemical vapor deposition (CVD). (1) Precursor

gas feed, (2) homogeneous gas phase reaction, (3) heterogeneous reaction, (4) gas exhaust.

The steps of the heterogeneous reaction are: (3a) adsorption of the reactants at the substrate

surface, (3b) surface reactions, (3c) nucleation and growth, (3d) desorption of molecules or

by-products. Redrawn after [41].

In contrast to PVD, CVD has a high throwing power, making it possible to coat substrates with complex three dimensional geometries. Furthermore, CVD offers the possibility to simultaneously coat large numbers of substrates with high coating thicknesses [40]. A disadvantage of especially thermally activated CVD is, however, the high deposition temperatures needed for the precursor dissociation, which limits the possible substrate materials [42]. Furthermore, CVD coatings often exhibit a high surface roughness and tensile residual stress, which deteriorate the performance in cutting applications. Thus, CVD coatings are commonly post-treated to overcome these issues. [43,44].

2.2 Cathodic arc evaporation

In CAE, solid materials, the so called targets, are transferred to the vapor phase by a high current and low voltage electric discharge between the target material (i.e. cathode) and the deposition chamber wall (i.e. anode). The arc discharge is triggered by a short-time contact between the two electrodes using a mechanical igniter. A nanometer to micrometer-sized arc spot of high current density (up to 10^{12} A/m^2) is formed at the

cathode surface that is successively extinct and reignited rapidly at random locations in the near proximity of the previous spot, resulting in an apparent motion of the spot over the cathode surface [45,46]. This random spot motion is confined by the insulating border surrounding the cathode and can be guided by magnetic fields. Due to the high current density of the arc spot, the cathode surface is heated up rapidly, resulting in explosion-like evaporation and ionization of the target material [1]. The kinetic energy of the ions depends on the element and is between 20 eV and 200 eV for light and heavy elements, respectively [1,46]. Cathodic arc plasmas contain highly ionized ions and the distribution of the ionization states can be shifted to higher charge states by both, increasing the arc current and by applying strong magnetic fields [47,48]. Due to the high charge state, kinetic energy and degree of plasma ionization, uniform and dense coatings can be grown at relatively low substrate temperatures. To further tune the properties such as hardness, density and residual stress of the coatings, the energy of the ions arriving at the substrate can be tailored by applying a so-called bias voltage to the substrate, which is a negative voltage between the substrate and the deposition chamber [1,39,49]. This technique is especially powerful in CAE, since the degree of ionization in the plasma is high (up to 100 %, depending on the material) [39,46]. In addition to the working as (e.g. Ar), CAE offers the possibility to introduce reactive gases, such as N_2 or O_2, into the deposition chamber, which react with the evaporated target material and lead to the formation of e.g. nitride or oxide coatings [50]. One drawback of CAE is the emission of macroparticles, so-called droplets, which are particles of molten target material generated during the target evaporation process. These droplets are incorporated into the coating as defects which weaken the coating performance [51]. A possibility to prevent the incorporation of droplets in the coating is magnetic filtering, where the ion flux is guided by a magnetic field along a bent trajectory. The ions are hereby separated from the heavier droplets which have a too high mass-to-charge ratio to follow the magnetic field lines and move along a straight path [46]. This technique, however, is rarely used for the deposition of

hard coatings on cutting tools [39]. Another point to consider is that CAE is a line-of-sight deposition process, which means that the substrate is only coated at the side that is directly facing the target.

2.3 Coating growth

The coating growth can be described by the steps schematically shown in Fig. 2. Incoming particles from the gas phase hit the substrate surface, where they are either immediately reflected or condense on the surface. After diffusion for some dwell time, the loosely bonded atoms can either desorb or adsorb at energetically favorable sites e.g. lattice defects, ledges or kinks or grain boundaries [37,50,52]. Adsorbed particles may diffuse towards other adsorbed particles to form clusters that continue to grow, a process which is called nucleation. Through inter-diffusion the coating particles may interact with the substrate material.
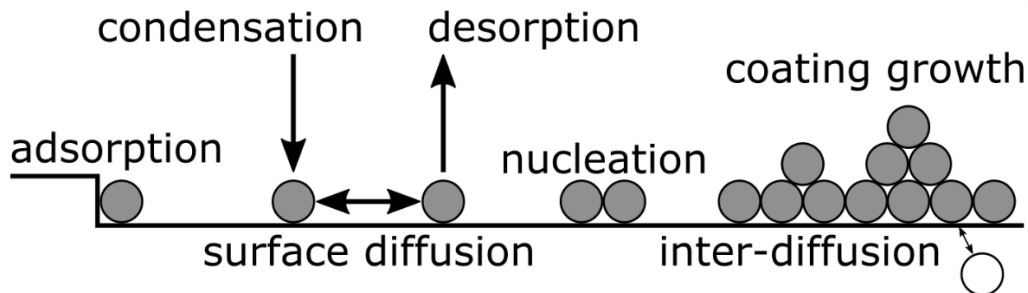

Fig. 2: Schematic of the principle steps of coating growth. Redrawn after [52].

Depending on the coating and substrate materials, three different growth modes can be distinguished. A schematic of the different growth modes can be found in Fig. 3, which are known as (i) island growth (Volmer-Weber), (ii) layer growth (Frank-Van der Merwe) and (iii) a combination of island and layer growth (Stranksi-Krastanov) [37,50,52][37,52]. Island growth occurs, when the binding energy between the atoms or molecules in the coating is higher than to the substrate. Hereby, nucleation occurs in three dimensions. Layer growth shows the exact opposite behavior, where the atoms and molecules are more bound to the substrate than to each other. The nucleation develops mainly in two dimensions. Stranski-Krastanov growth shows layer growth for the first

couple of monolayers, which is then followed by the energetically more favorable island growth [37,50,52]. The most common growth mode observed for hard coatings is island growth [53].
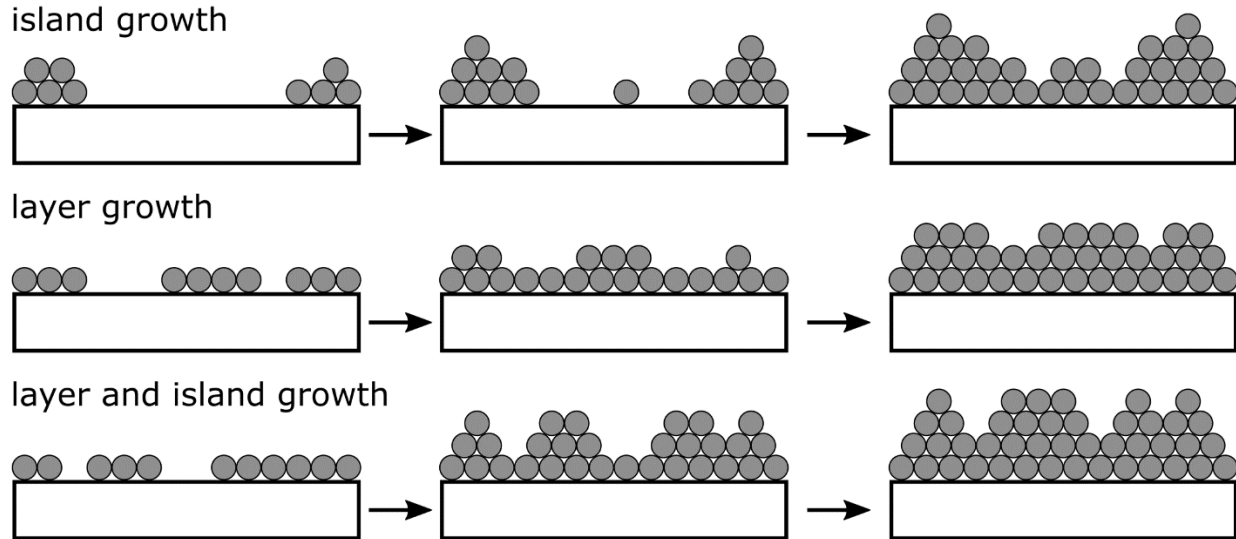

Fig. 3. Different growth modes for coating growth on substrates. Redrawn after [50].

Besides the used coating and substrate materials, also the deposition conditions affect the growth kinetics and consequently the coating microstructure. The relation between the different deposition parameters, e.g. deposition temperature, pressure and bias voltage, and the coating microstructure is described in so-called structure zone models (SZM) [54]. Depending on the deposition method, there exist different SZMs. The first SZM was introduced by Movchan and Demchishin for thermally evaporated thick coatings, where they related the structure of the coatings to only one parameter, the so-called homologous temperature T_h, which is the substrate temperature divided by the melting temperature of the coating material [55]. They categorized the resulting structure in three different zones. Zone 1 describes a porous structure of the coatings that forms due to a low surface mobility of the atoms at $T_h < 0.3$. For higher temperatures $0.3 < T_h < 0.5$, in zone 2, the surface mobility is increased and surface diffusion processes lead to dense coatings with uniform columnar grains. For $T_h > 0.5$ dense coatings with large equiaxed grains are formed due to bulk diffusion and recrystallization [55]. Later, this model was

adapted by several authors and more deposition parameters were included. Thornton extended the SZM by adding the pressure of the sputtering gas. He also introduced another zone for $0.2 < T_h < 0.4$, the so-called zone T, a transition zone with a high surface diffusion, but limited grain boundary diffusion, resulting in competitive growth with V-shaped grains [53]. Besides the deposition pressure, also the substrate bias voltage is an important deposition parameter for PVD processes. Messier et al. included the substrate bias voltage in the original SZM by Movchan and Demchishin [56]. In order to find a universal model to describe the relation between the deposition parameters and the microstructure, Anders adapted Thornton's SZM by generalizing the meaning of the model axes and adding the coating thickness as third axis [54]. A graphical representation of the SZM proposed by Anders is shown in Fig 4a. The T_h axis of Thornton's SZM is replaced by the generalized temperature T^*, which includes T_h, as well as a temperature shift that is caused by the potential energy of particles arriving at the surface. The linear pressure axis is replaced by a normalized energy E^*, which describes the displacement and heating effects of particles bombarding the surface due to their kinetic energy [54].

An SZM for CVD, similar to Movchan and Demchishin's for PVD, is shown in Fig. 4b [40]. The microstructure of CVD coatings can be classified in three zones, depending on the deposition temperature, pressure, supersaturation, coating thickness and the feed gas composition. With decreasing deposition temperature and pressure and increasing supersaturation, the microstructure changes from columnar grains with dome-like caps (zone 1) over columnar and facetted grains (zone 2) to globular grains (zone 3). The changes in microstructure can also be related to a change in the surface diffusion, which is the highest for high deposition temperatures in zone 1 and the lowest for low deposition temperatures in zone 3 [40].
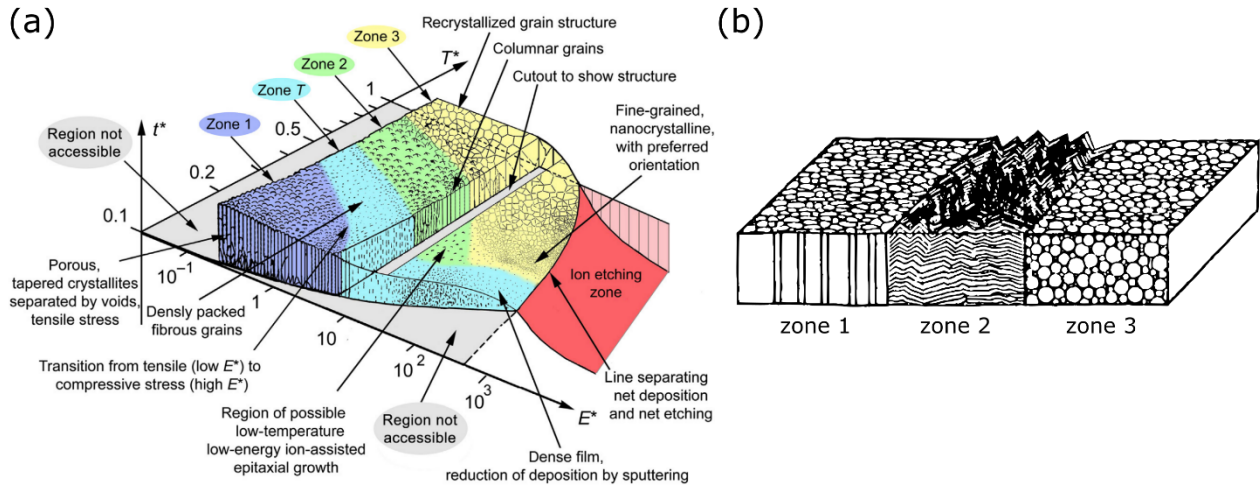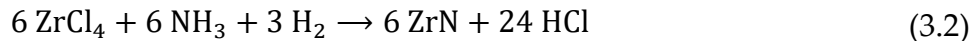
Fig. 4: (a) Structure zone model (SZM) describing the relation between generalized deposition parameters and the resulting coating microstructure. E* is the normalized energy flux, T* the generalized temperature and t* the coating thickness [54]. *(b) SZM for CVD. Depending on the deposition conditions, the microstructure changes from columnar grains (zone 1) to facetted columnar grains (zone 2) to globular grains (zone 3). Adapted after* [40].

3 Coating materials

3.1 ZrN

Compared to the intensively investigated and widely used TiN coatings, ZrN exhibits a higher oxidation resistance, a lower electrical resistivity and a lower surface roughness, while maintaining comparable mechanical properties, making it a material that is perfectly suitable for protective hard coatings for cutting applications [7,8,58,9–15,57]. ZrN shows a face-centered cubic (fcc) rock salt crystal structure and, similar to TiN, predominant covalent bonding between the non-metal p-states from the N and the metal d-states from Zr, with minor metal-metal contributions but typically no non-metal to non-metal bonding [59,60]. ZrN coatings can be synthesized by CVD and PVD. CVD ZrN coatings are typically obtained by chlorinating the metallic Zr precursor with HCl forming gaseous $ZrCl_4$, which is brought in the main deposition chamber using H_2 as carrier gas. With the addition of N_2, NH_3 or a mixture of these two precursors to the precursor mixture, ZrN coatings are synthesized following the simplified reaction equations 3.1 and 3.2:

$$2\,ZrCl_4 + N_2 + 4\,H_2 \longrightarrow 2\,ZrN + 8\,HCl. \tag{3.1}$$

$$6\,ZrCl_4 + 6\,NH_3 + 3\,H_2 \longrightarrow 6\,ZrN + 24\,HCl \tag{3.2}$$

The deposition temperature using these precursors lies between 800 to 1000 °C [61]. However, the deposition of ZrN at 800 °C seems to be problematic and higher deposition temperatures should be chosen, since the undesired incorporation of Cl especially at the grain boundaries increases with decreasing deposition temperature. This behavior can be related to the increasing thermal decomposition rate of the $ZrCl_4$ precursor with temperature, an effect which was also observed for the decomposition of $TiCl_4$ for the deposition of TiN coatings [61–65]. This Cl contamination can significantly impair the mechanical properties [62,65–69]. In addition to the deposition temperature, H_2 plays an important role in the decomposition of $ZrCl_4$ as it acts not only as carrier gas but also as reducing agent for the reduction of Zr^{4+} in $ZrCl_4$ to Zr^{3+} in ZrN, a reaction which

is hindered at deposition temperatures below 900 °C [61]. Using NH_3 instead of N_2 as nitrogen providing precursor increases the deposition rate and enables the deposition at lower temperatures, which can be related to a higher reactivity of NH_3. Although the use of N_2 or a mixture of N_2 and NH_3 instead of only NH_3 leads to a lower deposition rate, it may be beneficial to add N_2, as a more homogeneous distribution of the coating thickness within the reaction chamber was observed by Rauchenwald et al. [61].

Several PVD methods are commonly used for the deposition of ZrN, such as magnetron sputter deposition [13,70–77], pulsed laser deposition [78], plasma-assisted pulsed vacuum arc discharge [79] or cathodic arc evaporation [80–85] from metallic Zr targets that react with N_2 gas. Usually PVD ZrN coatings exhibit columnar grains, where the grain size can be tuned by adapting the deposition parameters. For example, for CAE ZrN coatings, as seen in the SZM (Fig. 4a), the grain size decreases with decreasing deposition temperature, leading to an increase in hardness due to Hall-Petch strengthening [14,86]. Another method to decrease the grain size is by increasing the negative bias voltage, which was shown for magnetron sputtering and cathodic arc evaporation [86–88]. Furthermore, the grain size can also be influenced by the nitrogen pressure and increases with increasing deposition pressure [89,90]. Besides the grain size, also the crystallographic texture can be adjusted with the bias voltage. A <111> texture is often observed for CAE coatings deposited at high bias voltages, while a lower bias voltage leads to a <100> texture [14,26,83,91–93]. This characteristic can be attributed to the rising number of defects caused by the high energy of the incoming ions, which induces re-nucleation of the grains during coating growth [26,94].

3.2 $ZrC_{1-x}N_x$

Similar to the deposition of CVD ZrN coatings, CVD ZrCN and ZrC coatings are deposited from a chlorinated $ZrCl_4$ precursor, N and/or C providing precursors, H_2 and occasionally Ar. For the synthesis of ZrC typically CH_4, C_2H_2 or C_3H_6 are used as C feeding precursors [95–101]. Although CVD ZrCN coatings could be deposited by a combination

of C and N providing precursor, such as CH_4 or CH_3 for C and N_2, NH_3 or NH_4 for N, no reports of the use of these precursors could be found in literature and the deposition from CH_3CN as C and N providing precursor is usually chosen for the ZrCN deposition [65,102]. One reason for the application of the CH_3CN precursor is the possibility to deposit coatings at lower temperatures due to its low dissociation energy compared to the other named C and N providing precursors [103–105]. Common deposition temperatures for CVD ZrCN coatings are between 850 and 1000 °C [22,65,102,106]. PVD $ZrC_{1-x}N_x$ coatings are usually deposited from metal Zr targets and a gas mixture of Ar, N_2 as N donor and C_4H_{10}, C_2H_4, C_2H_2 or CH_4 as C donor [107–111] or from ZrC targets and N_2 gas [112]. By adjusting the gas flow ratios, the C/(C+N) ratio in the coatings can be varied [107,108,110].

With the addition of a third element such as C to ZrN, the coating properties can be further enhanced, leading to better mechanical properties or enhanced oxidation and corrosion resistance [17,20,108,111,113–115]. Adding C to the ZrN lattice results typically in the formation of a solid solution, where the C and N atoms occupy the octahedral interstitial sites in the fcc structure [60]. Ivashchenko et al. confirmed the full miscibility of ZrN and ZrC over the whole compositional range using density functional theory calculations [116]. The calculations show that the lattice parameter of ZrN increases linearly with the addition of C, which is in agreement with experimental results [108,116,117]. Coatings in the $ZrC_{1-x}N_x$ system, where $0 \leq x \leq 1$, are not as thoroughly investigated as their intensively studied and widely used counterparts from the $TiC_{1-x}N_x$ system [25,69,118–122]. However, $ZrC_{1-x}N_x$ coatings deposited by CVD and PVD have shown advantageous mechanical properties over $TiC_{1-x}N_x$ coatings [20,22,65,76,123,124]. Performance tests of $ZrC_{1-x}N_x$ and $TiC_{1-x}N_x$ under cyclic thermal loads by Garcia et al. [20,21] and Moreno et al. [17] and micro-mechanical investigations by El Azhari et al. [22] and Moreno et al. [17] revealed a superior performance of $ZrC_{1-x}N_x$ coatings due to a mix of high hardness, better intrinsic plasticity and higher cohesive strength compared to

$TiC_{1-x}N_x$ coatings. Besides the mechanical properties, also the oxidation resistance is an important property of hard coatings. The oxidation stability of $ZrC_{1-x}N_x$ coatings is discussed in detail in publication II [115]. There, the phase evolution was monitored in-situ using synchrotron X-ray diffraction and it was found that the oxidation starts with the formation of cubic and/or tetragonal (c/t)-ZrO_2. This phase then transforms to the monoclinic (m)-ZrO_2 phase, which is more stable for temperatures below 1170 °C [125]. The highest oxidation resistance and stability was observed for $ZrC_{0.4}N_{0.6}$, followed by ZrC and ZrN. The improved oxidation behavior was found to correlate with a higher relative c/t-ZrO_2 phase content in $ZrC_{0.4}N_{0.6}$ and ZrC compared to ZrN, which can be related to a stabilization of the c/t-ZrO_2 phase due to residual C and/or a smaller grain size in $ZrC_{0.4}N_{0.6}$ and ZrC [115]. As a result of this c/t-ZrO_2 phase stabilization, less grains undergo the c/t-$ZrO_2 \rightarrow$ m-ZrO_2 phase transformation, which is accompanied by a volume expansion of about 5 % [126,127]. This volume expansion leads to the formation of oxygen diffusion paths due to crack formation in the oxide scale of the coating, which decreases the oxidation resistance [115,128].

3.3 Multilayer coatings

Multilayer coatings consist of two or more layers of different materials with different intrinsic properties. By choosing an adequate combination of materials, the multilayer coatings can achieve properties superior to their single-layer counterparts. For example, hard material layers with a low oxidation resistance can be protected by layers of a material less prone to oxidation, in order to enhance the oxidation resistance of the whole multilayer coating [129–131]. Furthermore, the mechanical properties and especially the fracture behavior can be enhanced by the combination of hard and soft layers, as well as by a combination of layers with different elastic properties or strength [23]. There are several mechanisms that may occur in multilayer coatings that amplify the fracture properties, which are schematically displayed in Fig. 5. The first displayed mechanism is crack deflection at the interface, which hinders the crack propagation in the

material. The second mechanism is the delamination or generation of a void at the interface during cracking, which reduces the stress concentration at the interface. The third mechanism is dissipation of energy due to plastic deformation at the interface [29–31]. Another mechanism of crack deflection at the interface might occur for alternating strain fields in multilayer coatings [32–36]. These strain fields may develop due to coherency strains between the individual layers as a result of different lattice parameters and/or due to differences in elastic properties between the layer constituents [23,33]. Besides these mechanisms, also stress induced phase transformations may hinder crack propagation [31]. One example is the transformation of the c/t-ZrO_2 phase to the m-ZrO_2 phase, induced by the stress field around the crack tip, which is accompanied by a volume increase of ~5 %. In further consequence this volume expansion results in the development of a strain field, which absorbs the fracture energy and hinders crack propagation [31].
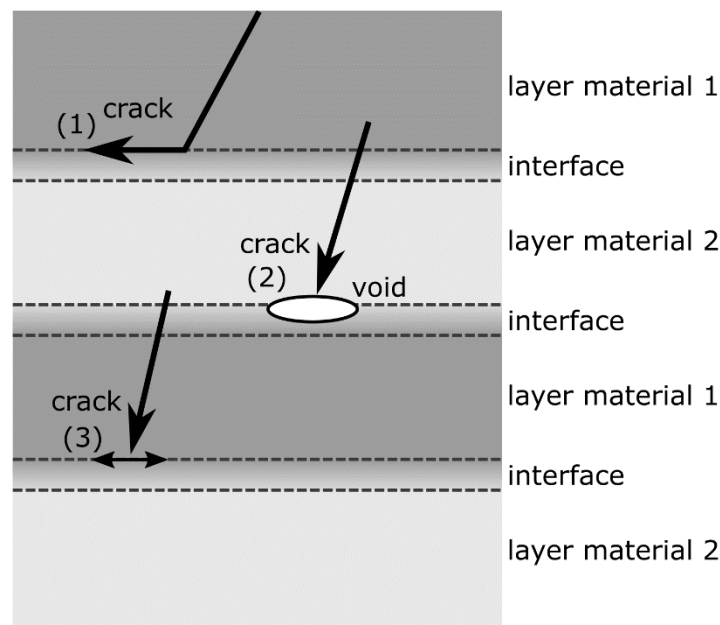

Fig. 5: Toughening mechanisms in multilayer coatings: (1) crack deflection at the interface, (2) delamination or void generation, (3) plastic deformation. Redrawn after [29].

TiN and TiAlN are two materials that are frequently used as protective hard coatings. While TiN has been commonly used in the cutting industry for several decades

due to its good hardness and adequate thermal stability and oxidation resistance up to ~500 °C, TiAlN shows even higher mechanical and thermal properties [6,132–136], making both coatings excellent candidates for the deposition of multilayer ZrN/TiN and ZrN/TiAlN coatings [92,137–145]. While ZrN and TiN coatings exhibit a fcc structure, TiAlN can be present in either fcc- or hexagonal structure, depending on the Al content and the deposition conditions [136,146–148]. The lattice parameter mismatch is ~7-8 % for fcc-ZrN and fcc-TiN [140,149] and ~9 % for fcc-ZrN and fcc-TiAlN [150]. Due to this lattice mismatch, a $ZrN/TiAl_{1-x}N_x$ multilayer architecture leads to the generation of misfit dislocations at the interface and/or coherency strains, which may increase the mechanical properties of the multilayer coatings compared to their single-layer counterparts. CAE ZrN/TiN and ZrN/TiAlN multilayer systems are investigated in publication III [26] and IV [150], respectively. Both publications show the formation of semi-coherent interfaces between the ZrN and $Ti_{1-x}Al_xN$ layers. In publication III, the focus was laid on the exploration of the influence of the bilayer thickness on the microstructure and mechanical properties with a special emphasis on the fracture behavior [26]. It was found that the grain size, as well as the <111> texture increase with decreasing ZrN/TiN bilayer thickness, which led to a rise in hardness and fracture stress compared to both, single-layer ZrN and TiN coatings [26]. The aim of publication IV was to study the influence of the individual ZrN layer thickness on the microstructure with special focus on the residual stress state [150]. There, a CAE ZrN/TiAlN multilayer coating with individual ZrN layer thickness increasing from the substrate towards the surface and constant TiAlN layer thickness was investigated using high-resolution techniques, such as cross-sectional X-ray nanodiffraction (CSnanoXRD) and high-resolution transmission electron microscopy. The investigations revealed that an increasing ZrN layer thickness leads to rising grain size and a decrease in residual stress [150].

4 Advanced characterization techniques for hard coatings

4.1 Cross-sectional X-ray nanodiffraction

In order to develop and improve state of the art hard coatings it is crucial to determine their functional properties as exact as possible. Especially for multilayer coatings with microstructural depth gradients or nanocomposite materials it is important to know how the microstructure changes along the coatings cross-section. Over the last decade, CSnanoXRD, a method which uses high energy synchrotron radiation to probe the microstructure of the coating along the cross-section, has become a powerful tool to investigate changes of the phase composition, residual stress and strain state, grain size and texture as a function of the coatings thickness [44,151–157]. In order to achieve a high spatial resolution, focused synchrotron beams with beam diameters < 100 nm are used [44,151,152].

A schematic CSnanoXRD experimental setup is shown in Fig. 6. A thin lamella, prepared using focused ion beam (FIB) milling, is placed in the synchrotron beam with the surface parallel to the incident beam and the cross-section of the coating is scanned in transmission geometry in the growth direction of the coating ("linescan"). Debye-Scherrer rings, arising from the individual phases of the coating, are recorded for each scanning position using a two-dimensional detector. To gain knowledge about the microstructure of the coatings, the resulting 2D diffractograms have to be further processed using software programs such as Fit2D [158] or PyFAI [159,160].
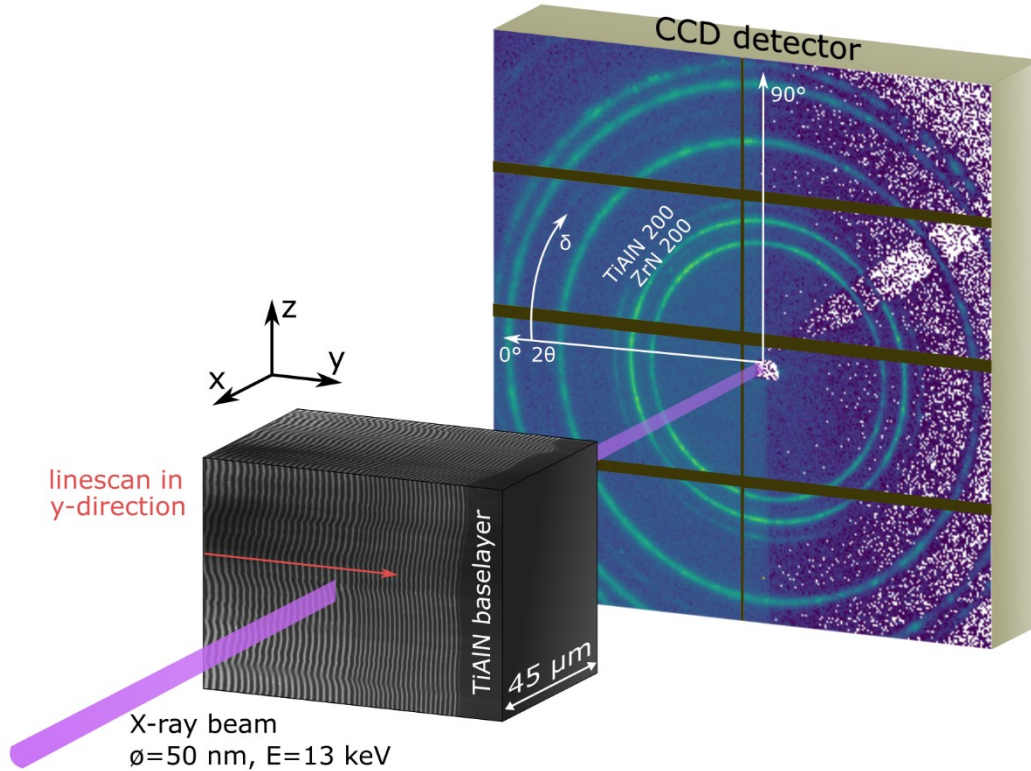
Fig. 6: Cross-sectional X-ray nanodiffraction (CSnanoXRD) setup. A focused ion beam (FIB) prepared lamella of a ZrN/TiAlN multilayer coating is scanned with an X-ray beam position resolved along the cross-section. Diffraction rings are recorded by a two-dimensional charged-coupled device (CCD) detector [own work].

In order to ensure a correct data evaluation, the experimental set-up has to be calibrated regarding the sample-to-detector distance, the beam center on the detector, the tilt and rotation angle of the detector, which is done by measuring a reference material such as LaB_6 or Al_2O_3 powder [161,162]. Taking the calibration into account, the diffraction data can be further processed.

The necessary steps to determine the phase composition, residual stress and strain state, as well as texture will be briefly outlined in the following. To determine the depth resolved evolution of phase composition, the Debye-Scherrer rings are integrated azimuthally along the δ angle (see Fig. 6), resulting in 1D diffractograms for each measurement position along the linescan. The diffractograms are usually presented in a

phase plot. An exemplary phase plot is displayed in Fig. 7a. By evaluating the distortion of the Debye-Scherrer rings, the strain in the coating can be determined if the unstrained d-spacing and the Poisson's ratio are known, using a method equivalent to the $\sin^2\psi$ method [163,164]. From the strains, the residual stress can be calculated by applying the X-ray elastic constants of the investigated material. With the assumption of a biaxial strain state it is sufficient to provide one X-ray elastic constant $\frac{1}{2}s_2^{hkl}$ to calculate the in-plane residual stress. The texture of the coating can be qualitatively determined by plotting the azimuthal intensity distribution of the integrated intensity of specific peaks from the Debye-Scherrer rings as a function of the azimuthal angle δ [152]. In Fig. 7b, three azimuthal intensity distributions of the ZrN 111, 200 and 220 peaks of a CAE ZrN/TiAlN multilayer coating are displayed. For this coating, a strong <100> texture can be observed. Details about the coating can be found in publication IV. Another method to quantify the texture is by Rietveld refinement, e.g. with the software package Materials Analysis Using Diffraction (MAUD) [165] or with MTEX [166]. These evaluation methods have the advantage that the orientation distribution function is calculated, making it possible to display the texture at selected depths with inverse pole figures [151,167]. And last but not least, in order to assess properties such as grain size, microstrains and structural defects, evaluation of the full width at half maximum (FWHM) of the diffraction peaks is necessary. The FWHM is influenced by the size of coherently diffracting domains as well as by strains of second and third order, which arise due to the presence of structural defects such as lattice distortions and dislocations [168–171]. While qualitative trends in microstructure can be observed from changes in the FWHM, a quantitative Rietveld refinement of the diffraction data can help to differentiate between the contributions of the domain size and the strains to the FWHM [172–174].
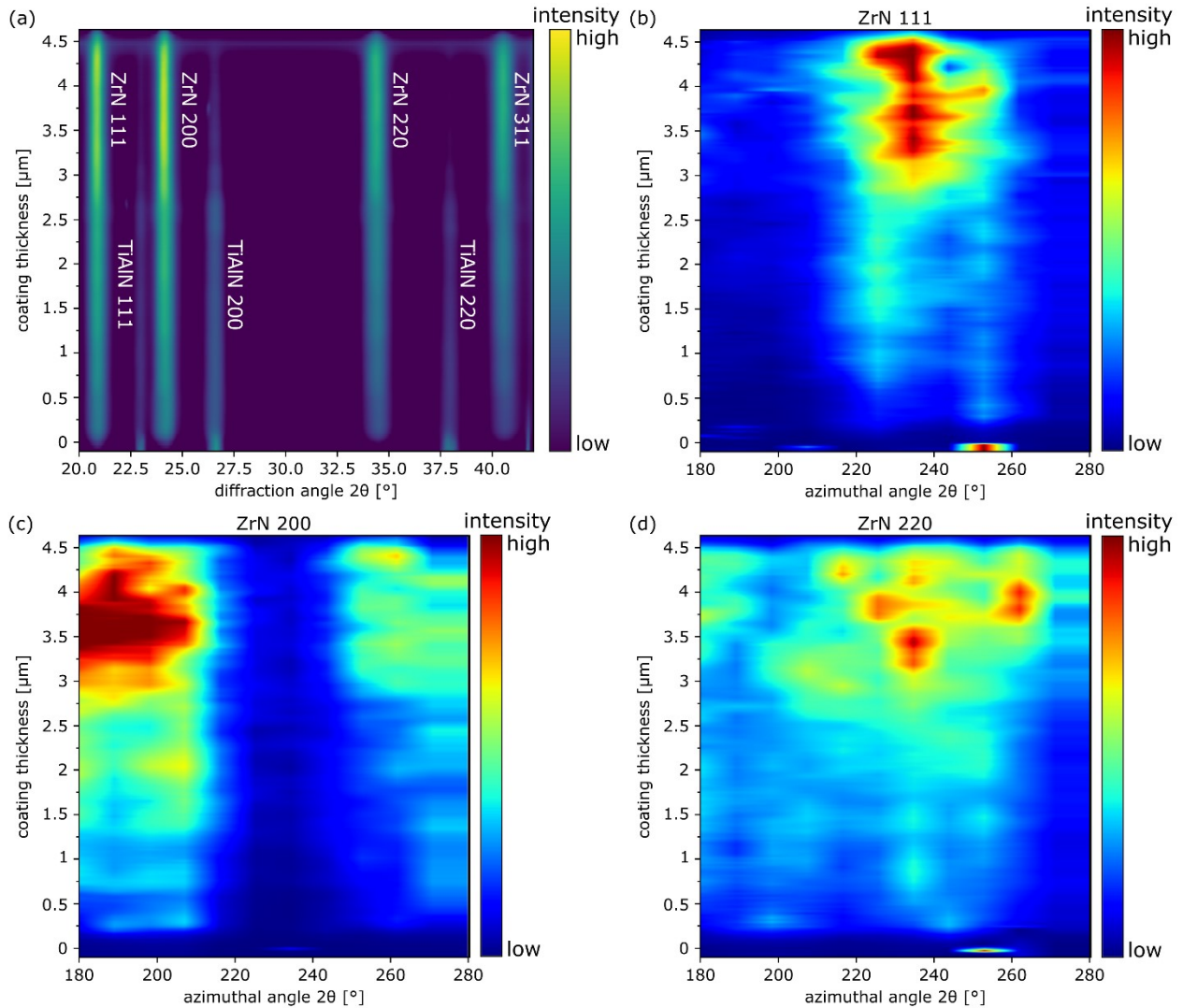
Fig. 7: (a) Exemplary phase plot of a PVD ZrN/TiAlN multilayer coating, obtained from the CSnanoXRD investigation. Azimuthal intensity distributions of the (b) ZrN 111, (c) ZrN 200 and (d) ZrN 220 peaks [own work].

4.2   In-situ high-temperature synchrotron X-ray diffraction

Besides the microstructure, also the thermal properties and the oxidation behavior are important for the design of hard coatings, since the temperatures in modern cutting applications may exceed 1000 °C due to the friction between the work piece material and the machining tool [175]. High-energy synchrotron XRD offers the possibility to determine the temperature-dependent phase evolution during oxidation by heating specimens in special designed furnaces [176]. The high brilliance of the synchrotron beam

offers the possibility for a fast data acquisition of only few seconds for each temperature step, allowing for a precise determination of phase transition temperatures under oxidizing conditions. Although it is also possible to perform high temperature in-situ experiments on a laboratory XRD [177–179], this conventional technique cannot compete with in-situ measurements using high-energy synchrotron radiation due to the aforementioned high brilliance, fast data acquisition and high energy resolution of the latter [176,180]. In order to correlate the diffraction data with other measurement techniques to detect phase transitions such as differential scanning calorimetry, the in-situ experiments are usually conducted using powdered coatings. By measuring the powdered coatings, also the influence of substrate interaction with the coatings can be excluded and the high temperature behavior of the coating only can be investigated [115,176,178,181]. Similar to the nanodiffraction experiments, Debye-Scherrer rings are recorded for each temperature step on a 2D-detector. After the azimuthal integration of the 2D diffractograms, the resulting 1D diffractograms can be depicted in a temperature dependent phase plot, as exemplarily shown in Fig. 8 for a CVD ZrN coating. A detailed description of the architecture of the coating and interpretation of the measurements can be found in publications I and II [115,182]. The quantitative phase evolution can be determined using Rietveld refinement of all individual recorded diffraction patterns. This refinement process can be performed in an automated manner using sequential or parametric Rietveld refinement [183].
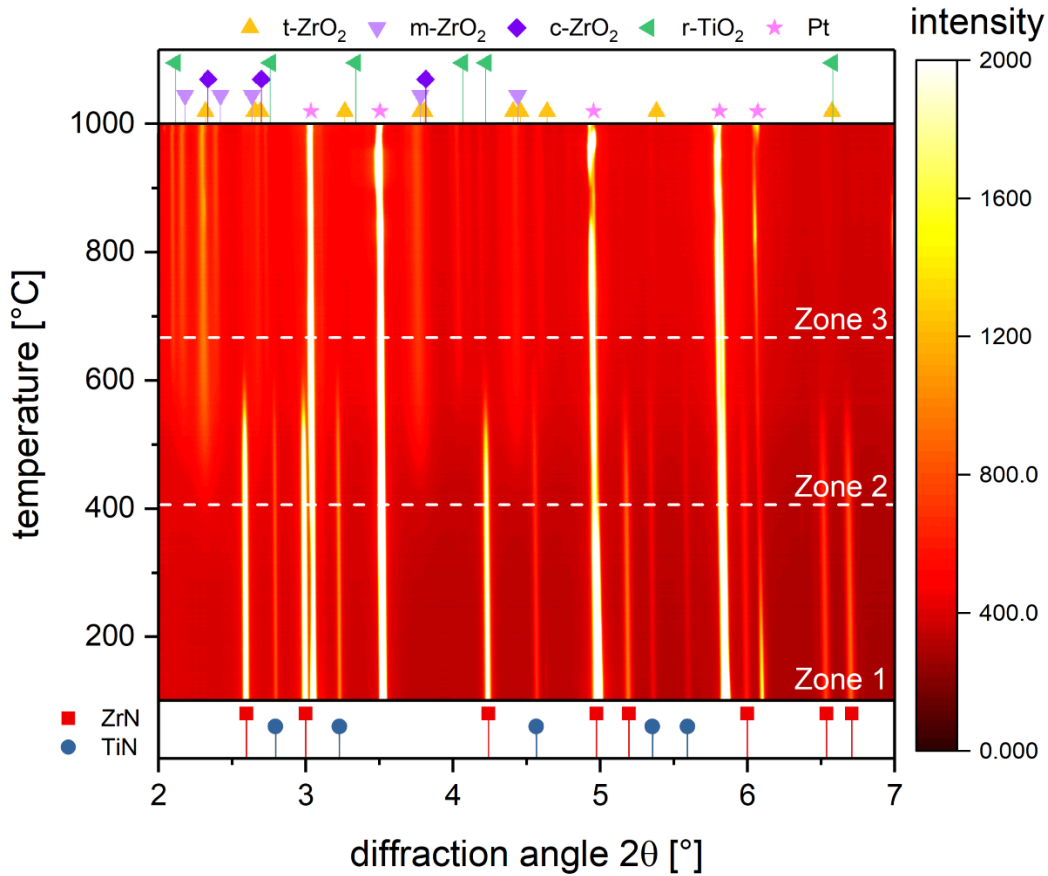
Fig. 8: Exemplary temperature dependent phase evolution of a CVD ZrN powdered coating under oxidizing atmosphere, measured by in-situ synchrotron X-ray diffraction [adapted after [115]].

4.3 Micro-mechanical bending tests

The mechanical properties of hard coatings are important to assess the performance during machining applications. Nanoindentation provides a well-established and easily accessible method to determine the hardness and the Young's modulus of the coatings. However, besides these two properties, also the fracture properties are crucial when estimating the effectiveness of hard coatings for various cutting applications [23,184,185]. The fracture properties comprise the fracture stress and the fracture toughness, which is also known as the critical stress intensity factor K_{IC}. The fracture stress and toughness describe the resistance of a material to crack initiation and propagation, respectively. Determining the fracture behavior is not a straight forward

method, as significant preparation time and knowledge is necessary to prepare the specimens in a suitable way to perform the experiments. The fracture properties can be determined from micro-sized cantilevers that are prepared from the coatings by FIB milling. The cantilevers are loaded with a nanoindenter tip in-situ (in a scanning or transmission electron microscope) [23,24,186] or ex-situ until fracture occurs [170,187–190]. The loading is performed in displacement-controlled mode and the load-displacement curves are recorded, which are used to evaluate the fracture properties. The fracture stress can be determined from unnotched specimens [191,192]. Cantilevers with a sharp notch near the cantilever beam support are used to evaluate the fracture toughness of the coatings [191–193]. Due to the absence of significant plastic deformation in the fracture of hard coatings, evaluation can be conducted according to the linear-elastic bending beam theory [194].

5   Summary and conclusions

The aim of this thesis was to develop and to thoroughly analyze ZrN-based hard coatings suitable for cutting applications, using a wide variety of advanced characterization techniques, with the final target of establishing structure-property relationships. In a first step, chemical vapor deposition was used to synthesize ZrN, ZrCN and ZrC coatings. Besides a characterization of the microstructure and mechanical properties, the oxidation behavior was studied in detail using in-situ synchrotron X-ray diffraction. The results of these studies are presented in publications I and II. The presence of C leads to a decrease of tensile residual stresses arising due to the mismatch in the coefficient of thermal expansion between the substrate and the coating material and further significantly enhances the hardness of the coatings, which can be attributed to a decreasing grain size and a stronger covalent bonding character. The oxidation study of the ZrN, ZrCN and ZrC coatings also revealed favorable properties upon C addition, since the ZrCN coating was found to exhibit the highest oxidation onset temperature of ~570 °C, followed by ZrC at ~530 °C and ZrN at only 400 °C. The oxidation mechanism was determined to be similar for all three coatings, showing the initial formation of cubic and/or tetragonal $c/t-ZrO_2$ phases, which transform into monoclinic $m-ZrO_2$ phase at higher temperatures. The temperature dependent phase composition determined by parametric Rietveld refinement was, however, different, since ZrCN and ZrC showed the highest $c/t-ZrO_2$ phase fractions, indicating that these phases were stabilized, possibly due to residual amorphous C and a smaller grain size in the ZrCN and ZrC samples. In a next step, the microstructure and mechanical properties of physical vapor deposited ZrN/Ti(Al)N multilayer coatings was investigated in detail. In publication III, special focus was placed on evaluating the fracture behavior of ZrN/TiN coatings with different bilayer thicknesses (Λ) and to compare it to the respective ZrN and TiN single layer coatings. The ZrN/TiN multilayer sample with the lowest Λ of 35 nm exhibited the highest hardness of 28.0 ± 1.1 GPa, which is similar to the hardness value determined for the TiN

single-layer but significantly higher compared to the ZrN single-layer. ZrN exhibited the highest fracture toughness, while the ZrN/TiN multilayer coatings revealed—regardless of the respective Λ—higher fracture stress values in comparison to the TiN and ZrN single-layers. In the final step of this thesis, again multilayer coatings were investigated, focusing on evaluating the microstructure and residual stress state of a physical vapor deposited graded ZrN/TiAlN multilayer coating with constant TiAlN and stepwise increasing ZrN individual layer thickness. The microstructural investigations discussed in publication IV showed an increasing grain size for thicker ZrN layers, additionally a (semi-)coherent growth of layers was observed. The position resolved evaluation of the residual stress state by cross-sectional X-ray nanodiffraction revealed decreasing compressive stress with increasing ZrN layer thickness, owing to larger grain sizes and therefore a lower number of grain boundaries. Furthermore, for ZrN layers <24 nm the ZrN phase exhibited significantly higher residual stress than TiAlN, while for ZrN layers >24 nm the stresses in both phases were nearly identical, which can be explained by the dominating effect of coherency stress fields for thin ZrN layers.

Applying a combination of several advanced characterization methods, the investigations within this thesis significantly contribute to the fundamental understanding of the deposition-structure-property relation of ZrN-based coatings. The enhancement of coating properties with different approaches such as alloying elements and multilayer architecture is explored, which enables a knowledge based design of protective hard coatings for machining applications.

6 References

[1]   C. Mitterer, PVD and CVD Hard Coatings, in: V.K.. Sarin (Ed.), Compr. Hard Mater., Vol. 2, Elsevier Ltd, Amsterdam, 2014: pp. 449–467. https://doi.org/10.1016/B978-0-08-096527-7.00035-0.

[2]   N. Schalk, M. Tkadletz, C. Mitterer, Hard coatings for cutting applications: Physical vs. chemical vapor deposition and future challenges for the coatings community, Surf. Coatings Technol. 429 (2022) 127949. https://doi.org/10.1016/j.surfcoat.2021.127949.

[3]   J.E. Sundgren, Structure and properties of TiN coatings, Thin Solid Films. 128 (1985) 21–44. https://doi.org/10.1016/0040-6090(85)90333-5.

[4]   H. Holleck, Material selection for hard coatings, J. Vac. Sci. Technol. A Vacuum, Surfaces, Film. 4 (1986) 2661–2669. https://doi.org/10.1116/1.573700.

[5]   H. Holleck, H. Schulz, Advanced Layer Material Constitution, Thin Solid Films. 153 (1987) 11–17.

[6]   O. Knotek, W.D. Münz, T. Leyendecker, Industrial deposition of binary, ternary, and quaternary nitrides of titanium, zirconium, and aluminum, J. Vac. Sci. Technol. A Vacuum, Surfaces, Film. 5 (1987) 2173–2179. https://doi.org/10.1116/1.574948.

[7]   D.F. Arias, Y.C. Arango, A. Devia, Study of TiN and ZrN thin films grown by cathodic arc technique, Appl. Surf. Sci. 253 (2006) 1683–1690. https://doi.org/10.1016/j.apsusc.2006.03.017.

[8]   B. Navinšek, A. Zalar, P. Panjan, I. Milošev, A. Cvelbar, Oxidation of TiN, ZrN, TiZrN, CrN, TiCrN and TiN/CrN multilayer hard coatings reactively sputtered at low temperature, Thin Solid Films. 281–282 (1996) 298–301. https://doi.org/10.1016/0040-6090(96)08663-4.

[9]   I. Milosev, H.-H. Strehblow, B. Navinsek, Comparison of TiN, ZrN, and CrN coatings under oxidation, Thin Solid Films. (1997) 246–254.

[10]   Z. Gao, Y. Chen, J. Kulczyk-Malecka, P. Kelly, Y. Zeng, X. Zhang, C. Li, H. Liu, N.

Rohbeck, P. Xiao, Comparison of the oxidation behavior of a zirconium nitride coating in water vapor and air at high temperature, Corros. Sci. 138 (2018) 242–251. https://doi.org/10.1016/j.corsci.2018.04.015.

[11]   L. Krusin-Elbaum, M. Wittmer, Oxidation kinetics of ZrN thin films, Thin Solid Films. 107 (1983) 111–116. https://doi.org/10.1016/0040-6090(83)90013-5.

[12]   D. Pilloud, A.S. Dehlinger, J.F. Pierson, A. Roman, L. Pichon, Reactively sputtered zirconium nitride coatings: Structural, mechanical, optical and electrical characteristics, Surf. Coatings Technol. 174–175 (2003) 338–344. https://doi.org/10.1016/S0257-8972(03)00613-3.

[13]   G. López, M.H. Staia, High-temperature tribological characterization of zirconium nitride coatings, Surf. Coatings Technol. 200 (2005) 2092–2099. https://doi.org/10.1016/j.surfcoat.2004.08.221.

[14]   J.A. Sue, H.H. Troue, Influence of crystallographic orientation, residual strains, crystallite size and microhardness on erosion in ZrN coating, Surf. Coatings Technol. 39/40 (1989) 421–434.

[15]   L. Li, X.Z. Yang, E.W. Niu, S.Z. Yang, X.Z. Li, G.H. Lv, H. Chen, Characterization of Ti–Zr–N films deposited by cathodic vacuum arc with different substrate bias, Appl. Surf. Sci. 254 (2007) 3909–3914. https://doi.org/10.1016/j.apsusc.2007.12.022.

[16]   S. Ruppi, Advances in chemically vapour deposited wear resistant coatings, J. Phys. IV JP. 11 (2001). https://doi.org/10.1051/jp4:20013106.

[17]   M. Moreno, I. El Azhari, D. Apel, M. Meixner, W. Wan, H. Pinto, F. Soldera, F. Mücklich, J. García, Design of Comb Crack Resistant Milling Inserts: A Comparison of Stresses, Crack Propagation, and Deformation Behavior between Ti(C,N)/α-Al2O3 and Zr(C,N)/α-Al2O3 CVD Coatings, Crystals. 11 (2021) 493. https://doi.org/10.3390/cryst11050493.

[18]   D. Hochauer, C. Mitterer, M. Penoy, C. Michotte, H.P. Martinz, M. Kathrein, Thermal stability of doped CVD κ-Al2O3 coatings, Surf. Coatings Technol. 204

(2010) 3713–3722. https://doi.org/10.1016/j.surfcoat.2010.04.056.

[19] R. Stylianou, D. Velic, W. Daves, W. Ecker, M. Tkadletz, N. Schalk, C. Czettl, C. Mitterer, Thermal crack formation in TiCN/α-Al$_2$O$_3$ bilayer coatings grown by thermal CVD on WC-Co substrates with varied Co content, Surf. Coatings Technol. 392 (2020) 125687. https://doi.org/10.1016/j.surfcoat.2020.125687.

[20] J. Garcia, M.F. Moreno, J. Östby, J. Persson, H.C. Pinto, Design of coated cemented carbides with improved comb crack resistance, 19th Plansee Semin. 2017. (2017) 1–8.

[21] J. García, M. Moreno, W. Wan, D. Apel, H. Pinto, M. Meixner, M. Klaus, C. Genzel, In situ investigations on stress and microstructure evolution in polycrystalline Ti(C,N)/α-Al$_2$O$_3$ CVD coatings under thermal cycling loads, Crystals. 11 (2021) 1–18. https://doi.org/10.3390/cryst11020158.

[22] I. El Azhari, J. Garcia, M. Zamanzade, F. Soldera, C. Pauly, L. Llanes, F. Mücklich, Investigations on micro-mechanical properties of polycrystalline Ti(C,N) and Zr(C,N) coatings, Acta Mater. 149 (2018) 364–376. https://doi.org/10.1016/j.actamat.2018.02.053.

[23] R. Daniel, M. Meindlhumer, J. Zalesak, B. Sartory, A. Zeilinger, C. Mitterer, J. Keckes, Fracture toughness enhancement of brittle nanostructured materials by spatial heterogeneity: A micromechanical proof for CrN/Cr and TiN/SiO$_x$ multilayers, Mater. Des. 104 (2016) 227–234. https://doi.org/10.1016/j.matdes.2016.05.029.

[24] R. Daniel, M. Meindlhumer, W. Baumegger, J. Zalesak, B. Sartory, M. Burghammer, C. Mitterer, J. Keckes, Grain boundary design of thin films: Using tilted brittle interfaces for multiple crack deflection toughening, Acta Mater. 122 (2017) 130–137. https://doi.org/10.1016/j.actamat.2016.09.027.

[25] C. Kainz, N. Schalk, M. Tkadletz, C. Mitterer, C. Czettl, Microstructure and mechanical properties of CVD TiN/TiBN multilayer coatings, Surf. Coatings

Technol. 370 (2019) 311–319. https://doi.org/10.1016/j.surfcoat.2019.04.086.

[26]   F. Frank, C. Kainz, M. Tkadletz, C. Czettl, M. Pohler, N. Schalk, Microstructural and micro-mechanical investigation of cathodic arc evaporated ZrN/TiN multilayer coatings with varying bilayer thickness, Surf. Coatings Technol. 432 (2022) 128070. https://doi.org/10.1016/j.surfcoat.2021.128070.

[27]   J.M. González-Carmona, J.D. Triviño, Gómez-Ovalle, C. Ortega, J.M. Alvarado-Orozco, H. Sánchez-Sthepa, A. Avila, Wear mechanisms identification using Kelvin probe force microscopy in TiN, ZrN and TiN/ZrN hard ceramic multilayers coatings,   Ceram.   Int.   46   (2020)   24592–24604. https://doi.org/10.1016/j.ceramint.2020.06.248.

[28]   Y.X. Xu, L. Chen, F. Pei, K.K. Chang, Y. Du, Effect of the modulation ratio on the interface structure of TiAlN/TiN and TiAlN/ZrN multilayers: First-principles and experimental   investigations,   Acta   Mater.   130   (2017)   281–288. https://doi.org/10.1016/j.actamat.2017.03.053.

[29]   H. Holleck, V. Schier, Multilayer PVD coatings for wear protection, Surf. Coatings Technol. 76–77 (1995) 328–336. https://doi.org/10.1016/0257-8972(95)02555-3.

[30]   G.S. Was, T. Foecke, Deformation and fracture in microlaminates, Thin Solid Films. 286 (1996) 1–31. https://doi.org/10.1016/S0040-6090(96)08905-5.

[31]   S. Zhang, D. Sun, Y. Fu, H. Du, Toughening of hard nanostructural thin films: A critical   review,   Surf.   Coatings   Technol.   198   (2005)   2–8. https://doi.org/10.1016/j.surfcoat.2004.10.020.

[32]   A.J. Blattner, R. Lakshminarayanan, D.K. Shetty, Toughening of layered ceramic composites with residual surface compression: Effects of layer thickness, Eng. Fract. Mech. 68 (2001) 1–7. https://doi.org/10.1016/S0013-7944(00)00096-5.

[33]   L. Geyang, H. Zenghu, T. Jiawan, X. Junhua, G. Mingyuan, Alternating stress field and superhardness effect in TiN/NbN superlattice films, J. Vac. Sci. Technol. A Vacuum, Surfaces, Film. 20 (2002) 674–677. https://doi.org/10.1116/1.1460887.

[34]   C. Ziebert, S. Ulrich, Hard multilayer coatings containing TiN and/or ZrN: A review and recent progress in their nanoscale characterization, J. Vac. Sci. Technol. A Vacuum, Surfaces, Film. 24 (2006) 554–583. https://doi.org/10.1116/1.2194031.

[35]   C.R. Chen, J. Pascual, F.D. Fischer, O. Kolednik, R. Danzer, Prediction of the fracture toughness of a ceramic multilayer composite - Modeling and experiments, Acta Mater. 55 (2007) 409–421. https://doi.org/10.1016/j.actamat.2006.07.046.

[36]   L. Yang, Y. Chen, J. Chen, C. Wang, G. He, Anisotropic deformation and fracture mechanisms of physical vapor deposited TiN/ZrN multilayers, Ceram. Int. 46 (2020) 15502–15509. https://doi.org/10.1016/j.ceramint.2020.03.095.

[37]   R.F. Bunshah, Handbook of deposition technologies for films and coatings: Science, technology, and applications, 2nd ed., Noyes Publications, Park Ridge, N.J., 1994.

[38]   H.O. Pierson, Handbook of Refractory Carbides and Nitrides: Properties, Characteristics, Processing and Applications, 1st ed., Noyes Publications, New York, 1996.

[39]   N. Schalk, M. Tkadletz, C. Mitterer, Hard Coatings for Cutting Applications: Physical vs. Chemical Vapor Deposition and Future Challenges for the Coatings Communtity, Surf. Coatings Technol. 429 (2021) 127949. https://doi.org/10.1016/j.surfcoat.2021.127949.

[40]   H.O. Pierson, Handbook of chemical vapor deposition (CVD), 2nd ed., Noyes Publications, Park Ridge, 1999. https://doi.org/10.1002/adma.19930050522.

[41]   K.L. Choy, Chemical vapour deposition of coatings, Prog. Mater. Sci. 48 (2003) 57–170. https://doi.org/10.1016/S0079-6425(01)00009-3.

[42]   H.G. Prengel, W.R. Pfouts, A.T. Santhanam, State of the art in hard coatings for carbide cutting tools, Surf. Coatings Technol. 102 (1998) 183–190. https://doi.org/10.1016/S0257-8972(96)03061-7.

[43]   N. Schalk, C. Mitterer, C. Czettl, B. Sartory, M. Penoy, C. Michotte, Dry-Blasting of α- and κ-Al$_2$O$_3$ CVD Hard Coatings: Friction Behaviour and Thermal Stress

Relaxation, Tribol. Lett. 52 (2013) 147–154. https://doi.org/10.1007/s11249-013-0201-3.

[44]   M. Tkadletz, J. Keckes, N. Schalk, I. Krajinovic, M. Burghammer, C. Czettl, C. Mitterer, Residual stress gradients in α-Al$_2$O$_3$ hard coatings determined by pencil-beam X-ray nanodiffraction: The influence of blasting media, Surf. Coatings Technol. 262 (2015) 134–140. https://doi.org/10.1016/j.surfcoat.2014.12.028.

[45]   A. Anders, Cathodic Arcs: From Fractal Spots to Energetic Condensation, Springer, New York, NY, 2008. https://doi.org/https://doi.org/10.1007/978-0-387-79108-1.

[46]   D.M. Sanders, A. Anders, Review of cathodic arc deposition technology at the start of the new millennium, Surf. Coatings Technol. 133–134 (2000) 78–90. https://doi.org/10.1016/S0257-8972(00)00879-3.

[47]   E.M. Oks, I.G. Brown, M.R. Dickinson, R.A. MacGill, H. Emig, P. Spädtke, B.H. Wolf, Elevated ion charge states in vacuum arc plasmas in a magnetic field, Appl. Phys. Lett. 67 (1995) 200. https://doi.org/10.1063/1.114666.

[48]   E.M. Oks, A. Anders, L.G. Brown, M.R. Dickinson, R.A. MacGill, Ion charge state distributions in high current vacuum arc plasmas in a magnetic field, IEEE Trans. Plasma Sci. 24 (1996) 1174–1183. https://doi.org/10.1109/27.533127.

[49]   P.H. Mayrhofer, C. Mitterer, L. Hultman, H. Clemens, Microstructural design of hard coatings, Prog. Mater. Sci. 51 (2006) 1032–1114. https://doi.org/10.1016/j.pmatsci.2006.02.002.

[50]   M. Ohring, Materials Science of Thin Films: Depositon & Structure, 2nd ed., Academic Press, San Diego, 2002.

[51]   M. Tkadletz, C. Mitterer, B. Sartory, I. Letofsky-Papst, C. Czettl, C. Michotte, The effect of droplets in arc evaporated TiAlTaN hard coatings on the wear behavior, Surf. Coatings Technol. 257 (2014) 95–101. https://doi.org/10.1016/j.surfcoat.2014.01.010.

[52]   H. Lüth, Solid Surfaces, Interfaces and Thin Films, 5th ed., Springer Berlin,

Heidelberg, 2010. https://doi.org/https://doi.org/10.1007/978-3-642-13592-7.

[53]   P.B. Barna, M. Adamik, Fundamental structure forming phenomena of polycrystalline films and the structure zone models, Thin Solid Films. 317 (1998) 27–33. https://doi.org/10.1016/S0040-6090(97)00503-8.

[54]   A. Anders, A structure zone diagram including plasma-based deposition and ion etching, Thin Solid Films. 518 (2010) 4087–4090. https://doi.org/10.1016/j.tsf.2009.10.145.

[55]   B.A. Movchan, A. V Demchishin, STRUCTURE AND PROPERTIES OF THICK CONDENSATES OF NICKEL, TITANIUM, TUNGSTEN, ALUMINUM OXIDES, AND ZIRCONIUM DIOXIDE IN VACUUM., Fiz. Met. Met. 28 653-60 (Oct 1969). (n.d.). https://www.osti.gov/biblio/4181669.

[56]   R. Messier, A.P. Giri, R.A. Roy, Revised structure zone model for thin film physical structure, J. Vac. Sci. Technol. A Vacuum, Surfaces, Film. 2 (1984) 500–503. https://doi.org/10.1116/1.572604.

[57]   E. Atar, E.S. Kayali, H. Cimenoglu, Sliding wear behaviour of ZrN and (Zr, 12 wt% Hf)N coatings, Tribol. Int. 39 (2006) 297–302. https://doi.org/10.1016/j.triboint.2005.01.038.

[58]   W.-J. Chou, G.-P. Yu, J.-H. Huang, Bias effect of ion-plated zirconium nitride film on Si(100), Thin Solid Films. 405 (2002) 162–169. https://doi.org/10.1016/S0040-6090(01)01762-X.

[59]   J. -E. Sundgren, H.T.G. Hentzell, A review of the present state of art in hard coatings grown from the vapor phase, J. Vac. Sci. Technol. A Vacuum, Surfaces, Film. 4 (1986) 2259–2279. https://doi.org/10.1116/1.574062.

[60]   R.W. Harrison, W.E. Lee, Processing and properties of ZrC, ZrN and ZrCN ceramics: a review, Adv. Appl. Ceram. 115 (2015) 294–307. https://doi.org/10.1179/1743676115y.0000000061.

[61]   E. Rauchenwald, M. Lessiak, R. Weissenbacher, R. Haubner, Chemical vapor

deposition of ZrN using in situ produced $ZrCl_4$ as a precursor, Ceram. Int. 45 (2019) 9410–9414. https://doi.org/10.1016/J.CERAMINT.2018.08.191.

[62]   K. Kawata, H. Sugimura, O. Takai, Effects of chlorine on tribological properties of TiN films prepared by pulsed d.c. plasma-enhanced chemical vapor deposition, Thin Solid Films. 407 (2002) 38–44. https://doi.org/10.1016/S0040-6090(02)00009-3.

[63]   N. Ramanuja, R.A. Levy, S.N. Dharmadhikari, E. Ramos, C.W. Pearce, S.C. Menasian, P.C. Schamberger, C.C. Collins, Synthesis and characterization of low pressure chemically vapor deposited titanium nitride films using TiCl4 and NH3, Mater. Lett. 57 (2002) 261–269. https://doi.org/10.1016/S0167-577X(02)00776-0.

[64]   M. Stoiber, E. Badisch, C. Lugmair, C. Mitterer, Low-friction TiN coatings deposited by PACVD, Surf. Coatings Technol. 163–164 (2003) 451–456. https://doi.org/10.1016/S0257-8972(02)00642-4.

[65]   I. El Azhari, J. Barrirero, J. García, F. Soldera, L. Llanes, F. Mücklich, Atom Probe Tomography investigations on grain boundary segregation in polycrystalline Ti(C,N) and Zr(C,N) CVD coatings, Scr. Mater. 162 (2019) 335–340. https://doi.org/10.1016/j.scriptamat.2018.11.041.

[66]   K.H. Kim, S.H. Lee, Comparative studies of TiN and $Ti_{1-x}Al_xN$ by plasma-assisted chemical vapor deposition using a $TiCl_4/AlCl_3/N_2/H_2/Ar$ gas mixture, Thin Solid Films. 283 (1996) 165–170. https://doi.org/10.1016/0040-6090(96)08766-4.

[67]   K.T. Rie, A. Gebauer, J. Woehle, Investigation of PA-CVD of TiN: Relations between process parameters, spectroscopic measurements and layer properties, Surf. Coatings Technol. 60 (1993) 385–388. https://doi.org/10.1016/0257-8972(93)90118-8.

[68]   S. Anderbouhr, V. Ghetta, E. Blanquet, C. Chabrol, F. Schuster, C. Bernard, R. Madar, LPCVD and PACVD (Ti,Al)N films: Morphology and mechanical properties, Surf. Coatings Technol. 115 (1999) 103–110. https://doi.org/10.1016/S0257-8972(99)00062-6.

[69]   K.T. Rie, A. Gebauer, J. Wöhle, Plasma assisted CVD for low temperature coatings

to improve the wear and corrosion resistance, Surf. Coatings Technol. 86–87 (1996) 498–506. https://doi.org/10.1016/S0257-8972(96)03177-5.

[70]   W.D. Sproul, Very high rate reactive sputtering of TiN, ZrN and HfN, Thin Solid Films. 107 (1983) 141–147. https://doi.org/10.1016/0040-6090(83)90016-0.

[71]   C. Mitterer, P.H. Mayrhofer, W. Waldhauser, E. Kelesoglu, P. Losbichler, The influence of the ion bombardment on the optical properties of TiN$_x$ and ZrN$_x$ coatings, Surf. Coatings Technol. 108–109 (1998) 230–235. https://doi.org/10.1016/S0257-8972(98)00651-3.

[72]   M. Meindlhumer, S. Klima, N. Jäger, A. Star, H. Hruby, C. Mitterer, J. Keckes, Stress-controlled decomposition routes in cubic AlCrN films assessed high-energy grazing incidence transmission X-ray diffraction, Sci. Rep. 9 (2019) 18027. https://doi.org/10.1038/s41598-019-54307-7.

[73]   D. Roman, J. Bernardi, C.L.G.D. Amorim, F.S. De Souza, A. Spinelli, C. Giacomelli, C.A. Figueroa, I.J.R. Baumvol, R.L.O. Basso, Effect of deposition temperature on microstructure and corrosion resistance of ZrN thin films deposited by DC reactive magnetron sputtering, Mater. Chem. Phys. 130 (2011) 147–153. https://doi.org/10.1016/j.matchemphys.2011.06.013.

[74]   Y.C. Chieh, W.Z. Lo, F.H. Lu, Microstructure evolution of ZrN films annealed in vacuum, Surf. Coatings Technol. 200 (2006) 3336–3340. https://doi.org/10.1016/j.surfcoat.2005.07.048.

[75]   C.P. Liu, H.G. Yang, Deposition temperature and thickness effects on the characteristics of dc-sputtered ZrNxfilms, Mater. Chem. Phys. 86 (2004) 370–374. https://doi.org/10.1016/j.matchemphys.2004.03.026.

[76]   J.H. Huang, K.L. Kuo, G.P. Yu, Oxidation behavior and corrosion resistance of vacuum annealed ZrN-coated stainless steel, Surf. Coatings Technol. 358 (2019) 308–319. https://doi.org/10.1016/j.surfcoat.2018.11.054.

[77]   F.-H. Lu, W.-Z. Lo, Degradation of ZrN films at high temperature under controlled

atmosphere, J. Vac. Sci. Technol. A Vacuum, Surfaces, Film. 22 (2004) 2071–2076. https://doi.org/10.1116/1.1786308.

[78] H. Spillmann, P.R. Willmott, M. Morstein, P.J. Uggowitzer, ZrN, Zr_xAl_yN and Zr_xGa_yN thin films-novel materials for hard coatings grown using pulsed laser deposition, Appl. Phys. A Mater. Sci. Process. 73 (2001) 441–450. https://doi.org/10.1007/s003390100780.

[79] H. Jiménez, E. Restrepo, A. Devia, Effect of the substrate temperature in ZrN coatings grown by the pulsed arc technique studied by XRD, Surf. Coatings Technol. 201 (2006) 1594–1601. https://doi.org/10.1016/j.surfcoat.2006.02.030.

[80] K.A. Gruss, T. Zheleva, R.F. Davis, T.R. Watkins, Characterization of zirconium nitride coatings deposited by cathodic arc sputtering, Surf. Coatings Technol. 107 (1998) 115–124. https://doi.org/10.1016/S0257-8972(98)00584-2.

[81] M.A. Vasylyev, B.N. Mordyuk, S.I. Sidorenko, S.M. Voloshko, A.P. Burmak, I.O. Kruhlov, V.I. Zakiev, Characterization of ZrN coating low-temperature deposited on the preliminary Ar+ ions treated 2024 Al-alloy, Surf. Coatings Technol. 361 (2019) 413–424. https://doi.org/10.1016/j.surfcoat.2018.12.010.

[82] E. Atar, E.S. Kayali, H. Cimenoglu, Reciprocating wear behaviour of (Zr, Hf)N coatings, Wear. 257 (2004) 633–639. https://doi.org/10.1016/j.wear.2004.03.005.

[83] E.W. Niu, G.H. Lv, W.R. Feng, S.H. Fan, X.Z. Yang, S.Z. Yang, L. Li, H. Chen, Influence of substrate bias on the structure and properties of ZrN films deposited by cathodic vacuum arc, Mater. Sci. Eng. A. 460–461 (2007) 135–139. https://doi.org/10.1016/j.msea.2007.02.085.

[84] J. Musil, I. Štěpánek, J.J. Musil, M. Kolego, O. Bláhová, J. Vyskočil, J. Kasl, Properties of TiN, ZrN and ZrTiN coatings prepared by cathodic arc evaporation, Mater. Sci. Eng. A. 163 (1993) 211–214. https://doi.org/10.1016/0921-5093(93)90792-d.

[85] O.A. Johansen, J.H. Dontje, R.L.D. Zenner, Reactive arc vapor ion deposition of TiN, ZrN and HfN, Thin Solid Films. 153 (1987) 75–82. https://doi.org/10.1016/0040-

6090(87)90171-4.

[86]   V.N. Zhitomirsky, I. Grimberg, R.L. Boxman, N.A. Travitzky, S. Goldsmith, B.Z. Weiss, Vacuum arc deposition and microstructure of ZrN-based coatings, Surf. Coatings Technol. 94–95 (1997) 207–212. https://doi.org/10.1016/S0257-8972(97)00422-2.

[87]   Z.B. Qi, P. Sun, F.P. Zhu, Z.C. Wang, D.L. Peng, C.H. Wu, The inverse Hall-Petch effect in nanocrystalline ZrN coatings, Surf. Coatings Technol. 205 (2011) 3692–3697. https://doi.org/10.1016/j.surfcoat.2011.01.021.

[88]   Q.N. Meng, M. Wen, C.Q. Qu, C.Q. Hu, W.T. Zheng, Preferred orientation, phase transition and hardness for sputtered zirconium nitride films grown at different substrate biases, Surf. Coatings Technol. 205 (2011) 2865–2870. https://doi.org/10.1016/j.surfcoat.2010.10.060.

[89]   J.H. Huang, C.H. Ho, G.P. Yu, Effect of nitrogen flow rate on the structure and mechanical properties of ZrN thin films on Si(1 0 0) and stainless steel substrates, Mater. Chem. Phys. 102 (2007) 31–38. https://doi.org/10.1016/j.matchemphys.2006.10.007.

[90]   B. Abdallah, M. Naddaf, M. A-Kharroub, Structural, mechanical, electrical and wetting properties of ZrN_x films deposited by Ar/N_2 vacuum arc discharge: Effect of nitrogen partial pressure, Nucl. Instruments Methods Phys. Res. Sect. B Beam Interact. with Mater. Atoms. 298 (2013) 55–60. https://doi.org/10.1016/j.nimb.2013.01.003.

[91]   H.M. Tung, J.H. Huang, D.G. Tsai, C.F. Ai, G.P. Yu, Hardness and residual stress in nanocrystalline ZrN films: Effect of bias voltage and heat treatment, Mater. Sci. Eng. A. 500 (2009) 104–108. https://doi.org/10.1016/j.msea.2008.09.006.

[92]   Y.O. Kravchenko, E. Coy, B. Peplińska, I. Iatsunskyi, K. Załęski, M. Kempiǹski, V.M. Beresnev, A. V. Pshyk, A.D. Pogrebnjak, Micro-mechanical investigation of (Al50Ti50)N coatings enhanced by ZrN layers in the nanolaminate architecture,

Appl. Surf. Sci. 534 (2020) 147573. https://doi.org/10.1016/j.apsusc.2020.147573.

[93]   Y.W. Lin, H.A. Chen, G.P. Yu, J.H. Huang, Effect of bias on the structure and properties of TiZrN thin films deposited by unbalanced magnetron sputtering, Thin Solid Films. 618 (2016) 13–20. https://doi.org/10.1016/j.tsf.2016.05.021.

[94]   G. Abadias, Y.Y. Tse, P. Guérin, V. Pelosin, Interdependence between stress, preferred orientation, and surface morphology of nanocrystalline TiN thin films deposited by dual ion beam sputtering, J. Appl. Phys. 99 (2006) 113519. https://doi.org/10.1063/1.2197287.

[95]   Y. Zhu, L. Cheng, B. Ma, S. Gao, W. Feng, Y. Liu, L. Zhang, Calculation and synthesis of ZrC by CVD from $ZrCl_4$–C_3H_6–H_2–Ar system with high H_2 percentage, Appl. Surf. Sci. 332 (2015) 591–598. https://doi.org/10.1016/J.APSUSC.2015.01.175.

[96]   W. Sun, X. Xiong, B.Y. Huang, G.D. Li, H.B. Zhang, P. Xiao, Z.K. Chen, X.L. Zheng, Microstructural Control of Zirconium Carbide Coating Prepared by Chemical Vapor Deposition, ECS Trans. 25 (2009) 291–299.

[97]   Y. Long, A. Javed, J. Chen, Z. Chen, X. Xiong, Phase composition, microstructure and mechanical properties of ZrC coatings produced by chemical vapor deposition, Ceram. Int. 40 (2014) 707–713. https://doi.org/10.1016/J.CERAMINT.2013.06.059.

[98]   Q. Liu, L. Zhang, L. Cheng, Y. Wang, Morphologies and growth mechanisms of zirconium carbide films by chemical vapor deposition, J. Coatings Technol. Res. 6 (2009) 269–273. https://doi.org/10.1007/s11998-008-9117-5.

[99]   Y. Wang, Q. Liu, J. Liu, L. Zhang, L. Cheng, Deposition mechanism for chemical vapor deposition of zirconium carbide coatings, J. Am. Ceram. Soc. 91 (2008) 1249–1252. https://doi.org/10.1111/j.1551-2916.2007.02253.x.

[100] S.-L. Wang, K.-Z. Li, H.-J. Li, Y.-L. Zhang, Y.-J. Wang, Effects of microstructures on the ablation behaviors of ZrC deposited by CVD, Surf. Coatings Technol. 240 (2014) 450–455. https://doi.org/10.1016/J.SURFCOAT.2013.12.074.

[101] J.H. Park, C.H. Jung, D.J. Kim, J.Y. Park, Effect of H_2 dilution gas on the growth of

ZrC during low pressure chemical vapor deposition in the ZrCl$_4$-CH$_4$-Ar system, Surf. Coatings Technol. 203 (2008) 87–90. https://doi.org/10.1016/j.surfcoat.2008.08.004.

[102] S. Kudapa, K. Narasimhan, P. Boppana, W.C.C. Russell, Characterization and properties of MTCVD TiCN and MTCVD ZrCN coatings, Surf. Coatings Technol. 120–121 (1999) 259–264. https://doi.org/10.1016/S0257-8972(99)00484-3.

[103] A. Larsson, S. Ruppi, Microstructure and properties of Ti(C,N) coatings produced by moderate temperature chemical vapour deposition, Thin Solid Films. 402 (2002) 203–210. https://doi.org/10.1016/S0040-6090(01)01712-6.

[104] R.S. Bonetti, H. Wiprächtiger, E. Mohn, CVD of titanium carbonitride at moderate temperature: Properties and applications, Met. Powder Rep. 45 (1990) 837–840. https://doi.org/10.1016/0026-0657(90)90575-2.

[105] I. Dreiling, A. Haug, H. Holzschuh, T. Chassé, Raman spectroscopy as a tool to study cubic Ti-C-N CVD coatings, Surf. Coatings Technol. 204 (2009) 1008–1012. https://doi.org/10.1016/j.surfcoat.2009.05.029.

[106] I. El Azhari, J. García, M. Zamanzade, F. Soldera, C. Pauly, C. Motz, L. Llanes, F. Mücklich, Micromechanical investigations of CVD coated WC-Co cemented carbide by micropillar compression, Mater. Des. 186 (2020) 108283. https://doi.org/10.1016/j.matdes.2019.108283.

[107] F. Zhou, K. Fu, B. Liao, J. Yu, C. Yang, X. Zhang, Effect of carbon content on nanostructural, mechanical and electrochemical characteristics of self-organized nc-ZrCN/a-CN$_x$ nanocomposite films, Appl. Surf. Sci. 327 (2015) 350–357. https://doi.org/10.1016/j.apsusc.2014.11.181.

[108] M.M. Larijani, M.B. Zanjanbar, A. Majdabadi, The effect of carbon fraction in Zr(C, N) films on the nano-structural properties and hardness, J. Alloys Compd. 492 (2010) 735–738. https://doi.org/10.1016/j.jallcom.2009.12.035.

[109] M. Braic, A. Popescu, R. Ripeanu, A. Kiss, V. Braic, C.N. Zoita, M. Balaceanu, A.

Vladescu, Structure and properties of Zr/ZrCN coatings deposited by cathodic arc method, Mater. Chem. Phys. 126 (2011) 818–825. https://doi.org/10.1016/j.matchemphys.2010.12.036.

[110] E. Grigore, C. Ruset, X. Li, H. Dong, Zirconium carbonitride films deposited by combined magnetron sputtering and ion implantation (CMSII), Surf. Coatings Technol. 204 (2010) 1889–1892. https://doi.org/10.1016/j.surfcoat.2009.11.012.

[111] J. De Gu, P.L. Chen, Investigation of the corrosion resistance of ZrCN hard coatings fabricated by advanced controlled arc plasma deposition, Surf. Coatings Technol. 200 (2006) 3341–3346. https://doi.org/10.1016/j.surfcoat.2005.07.049.

[112] C.-S. Chen, C.-P. Liu, Diffusion barrier properties of amorphous ZrCN films for copper metallization, J. Non. Cryst. Solids. 351 (2005) 3725–3729. https://doi.org/10.1016/J.JNONCRYSOL.2005.09.032.

[113] S. Calderon V., E. Silva, C. Palacio, M. Rebelo de Figueiredo, R. Franz, C. Mitterer, S. Carvalho, A. Espinosa, R. Escobar Galindo, Structure–property relations in ZrCN coatings for tribological applications, Surf. Coatings Technol. 205 (2010) 2134–2141. https://doi.org/10.1016/j.surfcoat.2010.08.126.

[114] S.H. Huang, C.Y. Tong, T.E. Hsieh, J.W. Lee, Microstructure and mechanical properties evaluation of cathodic arc deposited CrCN/ZrCN multilayer coatings, J. Alloys Compd. 803 (2019) 1005–1015. https://doi.org/10.1016/j.jallcom.2019.06.370.

[115] F. Frank, M. Tkadletz, C. Saringer, A. Stark, N. Schell, M. Deluca, C. Czettl, N. Schalk, In-Situ Investigation of the Oxidation Behaviour of Chemical Vapour Deposited Zr(C,N) Hard Coatings Using Synchrotron X-ray Diffraction, Coatings. 11 (2021) 264. https://doi.org/10.3390/coatings11030264.

[116] V.I. Ivashchenko, P.E.A. Turchi, V.I. Shevchenko, First-principles study of elastic and stability properties of ZrC-ZrN and ZrC-TiC alloys, J. Phys. Condens. Matter. 21 (2009) 395503. https://doi.org/10.1088/0953-8984/21/39/395503.

[117] W. Lengauer, S. Binder, K. Aigner, P. Ettmayer, A. Guillou, J. Debuigne, G. Groboth,

Solid state properties of group IVb carbonitrides, J. Alloys Compd. 217 (1995) 137–147. https://doi.org/10.1016/0925-8388(94)01315-9.

[118] W. Schintlmeister, W. Wallgram, J. Kranz, K. Gigl, Cutting tool materials coated by chemical vapour deposition, Wear. 100 (1984) 153–169.

[119] C. Kainz, N. Schalk, M. Tkadletz, C. Mitterer, C. Czettl, The effect of B and C addition on microstructure and mechanical properties of TiN hard coatings grown by chemical vapor deposition, Thin Solid Films. (2019). https://doi.org/10.1016/j.tsf.2019.05.002.

[120] J. Wagner, C. Mitterer, M. Penoy, C. Michotte, W. Wallgram, M. Kathrein, The effect of deposition temperature on microstructure and properties of thermal CVD TiN coatings, Int. J. Refract. Met. Hard Mater. 26 (2008) 120–126. https://doi.org/10.1016/j.ijrmhm.2007.01.010.

[121] K.-T. Rie, J. Wöhle, Plasma-CVD of TiCN and ZrCN films on light metals, Surf. Coatings Technol. 112 (1999) 226–229. https://doi.org/10.1016/S0257-8972(98)00803-2.

[122] R. Haubner, E. Rauchenwald, M. Lessiak, R. Pitonak, R. Weissenbacher, Novel high-performance CVD coatings for machining applications, Powder Metall. Prog. 18 (2018) 128–138. https://doi.org/10.1515/pmp-2018-0015.

[123] A. Ul-Hamid, Microstructure, Properties and Applications of Zr-Carbide, Zr-Nitride and Zr-Carbonitride Coatings - A Review, Mater. Adv. (2020). https://doi.org/10.1039/d0ma00233j.

[124] I. El Azhari, J. García, F. Soldera, S. Suarez, E. Jiménez-Piqué, F. Mücklich, L. Llanes, Contact damage investigation of CVD carbonitride hard coatings deposited on cemented carbides, Int. J. Refract. Met. Hard Mater. 86 (2020) 105050. https://doi.org/10.1016/j.ijrmhm.2019.105050.

[125] W.D. Kingery, H.K. Bowen, D.R. Uhlmann, Introduction to Ceramics, 2nd ed., Wiley, New York, 1976.

[126] S. Shukla, S. Seal, Mechanisms of room temperature metastable tetragonal phase stabilisation in Zirconia, Int. Mater. Rev. 50 (2005) 45–64. https://doi.org/10.1179/174328005X14267.

[127] H.F. Garces, B.S. Senturk, N.P. Padture, In situ Raman spectroscopy studies of high-temperature degradation of thermal barrier coatings by molten silicate deposits, Scr. Mater. 76 (2014) 29–32. https://doi.org/10.1016/j.scriptamat.2013.12.008.

[128] Z.B. Qi, Z.T. Wu, H.F. Liang, D.F. Zhang, J.H. Wang, Z.C. Wang, In situ and ex situ studies of microstructure evolution during high-temperature oxidation of ZrN hard coating, Scr. Mater. 97 (2015) 9–12. https://doi.org/10.1016/J.SCRIPTAMAT.2014.10.024.

[129] I. Wadsworth, I.J. Smith, L.A. Donohue, W.-D. Münz, Thermal stability and oxidation resistance of TiAlN/CrN multilayer coatings, Surf. Coatings Technol. 94–95 (1997) 315–321. https://doi.org/10.1016/S0257-8972(97)00353-8.

[130] J.W. Du, L. Chen, J. Chen, Y. Du, Mechanical properties, thermal stability and oxidation resistance of TiN/CrN multilayer coatings, Vacuum. 179 (2020) 109468. https://doi.org/10.1016/j.vacuum.2020.109468.

[131] N. Fukumoto, H. Ezura, T. Suzuki, Synthesis and oxidation resistance of TiAlSiN and multilayer TiAlSiN/CrAlN coating, Surf. Coatings Technol. 204 (2009) 902–906. https://doi.org/10.1016/j.surfcoat.2009.04.027.

[132] W.D. Sproul, Reactively sputtered nitrides and carbides of titanium, zirconium, and hafnium, J. Vac. Sci. Technol. A Vacuum, Surfaces, Film. 4 (1986) 2874–2878. https://doi.org/10.1116/1.573651.

[133] W. Münz, Titanium aluminum nitride films: A new alternative to TiN coatings, J. Vac. Sci. Technol. A Vacuum, Surfaces, Film. 4 (1986) 2717–2725. https://doi.org/10.1116/1.573713.

[134] H. Çalişkan, P. Panjan, S. Paskvale, Monitoring of Wear Characteristics of TiN and TiAlN Coatings at Long Sliding Distances, Tribol. Trans. 57 (2014) 496–502.

https://doi.org/10.1080/10402004.2014.884254.

[135] P.H. Mayrhofer, J. Sjölén, T. Larsson, L. Karlsson, L. Hultman, A. Hörling, C. Mitterer, Self-organized nanostructures in the Ti–Al–N system, Appl. Phys. Lett. 83 (2003) 2049–2051. https://doi.org/10.1063/1.1608464.

[136] P.H. Mayrhofer, L. Hultman, J.M. Schneider, P. Staron, H. Clemens, Spinodal decomposition of cubic $Ti_{1-x}Al_xN$: Comparison between experiments and modeling, Int. J. Mater. Res. 98 (2007) 1054–1059. https://doi.org/10.3139/146.101570.

[137] W.H. Soe, R. Yamamoto, Mechanical properties of ceramic multilayers: TiN/CrN, TiN/ZrN, and TiN/TaN, Mater. Chem. Phys. 50 (1997) 176–181. https://doi.org/10.1016/S0254-0584(97)80256-8.

[138] W.H. Soe, R. Yamamoto, Elastic and plastic properties of TiN based ceramic multilayers: TiN/CrN, TiN/ZrN, and TiN/TaN, Radiat. Eff. Defects Solids. 148 (1999) 213–231. https://doi.org/10.1080/10420159908229095.

[139] S. Ulrich, C. Ziebert, M. Stüber, E. Nold, H. Holleck, M. Göken, E. Schweitzer, P. Schlooßmacher, Correlation between constitution, properties and machining performance of TiN/ZrN multilayers, Surf. Coatings Technol. 188–189 (2004) 331–337. https://doi.org/10.1016/j.surfcoat.2004.08.056.

[140] X.M. Xu, J. Wang, Q.Y. Zhang, J. An, Y. Zhao, Effect of modulation structure on the growth behavior and mechanical properties of TiN/ZrN multilayers, Surf. Coatings Technol. 201 (2007) 5582–5586. https://doi.org/10.1016/j.surfcoat.2006.07.132.

[141] M. Naddaf, B. Abdallah, M. Ahmad, M. A-Kharroub, Influence of N_2 partial pressure on structural and microhardness properties of TiN/ZrN multilayers deposited by Ar/N_2 vacuum arc discharge, Nucl. Instruments Methods Phys. Res. Sect. B Beam Interact. with Mater. Atoms. 381 (2016) 90–95. https://doi.org/10.1016/j.nimb.2016.05.029.

[142] A. Pogrebnjak, V. Beresnev, K. Załęski, O. Sobol, V. Ivashchenko, E. Coy, O. Bondar, P. Konarski, S. Jurga, B. Postolnyi, Multilayered vacuum-arc nanocomposite

TiN/ZrN coatings before and after annealing: Structure, properties, first-principles calculations, Mater. Charact. 134 (2017) 55–63. https://doi.org/10.1016/j.matchar.2017.10.016.

[143] J.M. González-Carmona, J.D. Triviño, Gómez-Ovalle, C. Ortega, J.M. Alvarado-Orozco, H. Sánchez-Sthepa, A. Avila, Wear mechanisms identification using Kelvin probe force microscopy in TiN, ZrN and TiN/ZrN hard ceramic multilayers coatings, Ceram. Int. 46 (2020) 0–1. https://doi.org/10.1016/j.ceramint.2020.06.248.

[144] D.J. Li, M. Cao, X.Y. Deng, X. Sun, W.H. Chang, W.M. Lau, Multilayered coatings with alternate ZrN and TiAlN superlattices, Appl. Phys. Lett. 91 (2007) 7–10. https://doi.org/10.1063/1.2826284.

[145] Z. Lei, Y. Liu, F. Ma, Z. Song, Y. Li, Oxidation resistance of TiAlN/ZrN multilayer coatings, Vacuum. 127 (2016) 22–29. https://doi.org/10.1016/j.vacuum.2016.02.004.

[146] A. Kimura, H. Hasegawa, K. Yamada, T. Suzuki, Effects of Al content on hardness, lattice parameter and microstructure of $Ti_{1-x}Al_xN$ films, Surf. Coatings Technol. 120–121 (1999) 438–441. https://doi.org/10.1016/S0257-8972(99)00491-0.

[147] C. Wüstefeld, D. Rafaja, V. Klemm, C. Michotte, M. Kathrein, Effect of the aluminium content and the bias voltage on the microstructure formation in $Ti_{1-x}Al_xN$ protective coatings grown by cathodic arc evaporation, Surf. Coatings Technol. 205 (2010) 1345–1349. https://doi.org/10.1016/j.surfcoat.2010.07.057.

[148] A. Kimura, H. Hasegawa, K. Yamada, T. Suzuki, Metastable Ti1-xAlxN films with different Al content, J. Mater. Sci. Lett. 19 (2000) 601–602. https://doi.org/10.1023/A:1006738514096.

[149] C.J. Tavares, L. Rebouta, B. Almeida, J. Bessa E Sousa, Structural characterization of multilayered sputtered TiN/ZrN coatings, Surf. Coatings Technol. 100–101 (1998) 65–71. https://doi.org/10.1016/S0257-8972(97)00589-6.

[150] F. Frank, M. Tkadletz, C. Saringer, C. Czettl, M. Pohler, M. Burghammer, J. Todt, J. Zalesak, J. Keckes, N. Schalk, Investigation of the microstructure of a graded

ZrN/Ti0.33Al0.67N multilayer coating using cross-sectional characterization methods, Submitt. Publ. Surf. Coatings Technol. (2022).

[151] J. Keckes, M. Bartosik, R. Daniel, C. Mitterer, G. Maier, W. Ecker, J. Vila-Comamala, C. David, S. Schoeder, M. Burghammer, X-ray nanodiffraction reveals strain and microstructure evolution in nanocrystalline thin films, Scr. Mater. 67 (2012) 748–751. https://doi.org/10.1016/j.scriptamat.2012.07.034.

[152] J. Keckes, R. Daniel, J. Todt, J. Zalesak, B. Sartory, S. Braun, J. Gluch, M. Rosenthal, M. Burghammer, C. Mitterer, S. Niese, A. Kubec, 30 nm X-ray focusing correlates oscillatory stress, texture and structural defect gradients across multilayered TiN-SiO$_x$ thin film, Acta Mater. 144 (2018) 862–873. https://doi.org/10.1016/j.actamat.2017.11.049.

[153] A. Zeilinger, R. Daniel, T. Schöberl, M. Stefenelli, B. Sartory, J. Keckes, C. Mitterer, Resolving depth evolution of microstructure and hardness in sputtered CrN film, Thin Solid Films. 581 (2015) 75–79. https://doi.org/10.1016/j.tsf.2014.10.106.

[154] M. Meindlhumer, J. Zalesak, W. Ecker, M. Rosenthal, S. Niese, P. Gawlitza, H. Hruby, C. Mitterer, R. Daniel, J. Keckes, J. Todt, Nanoscale stress distributions and microstructural changes at scratch track cross-sections of a deformed brittle-ductile CrN-Cr bilayer, Mater. Des. 195 (2020) 109023. https://doi.org/10.1016/j.matdes.2020.109023.

[155] M. Meindlhumer, N. Jäger, S. Spor, M. Rosenthal, J.F. Keckes, H. Hruby, C. Mitterer, R. Daniel, J. Keckes, J. Todt, Nanoscale residual stress and microstructure gradients across the cutting edge area of a TiN coating on WC-Co, Scr. Mater. 182 (2020) 11–15. https://doi.org/10.1016/j.scriptamat.2020.02.031.

[156] N. Schalk, M. Tkadletz, V.L. Terziyska, M. Deluca, I. Letofsky-Papst, J. Keckes, C. Mitterer, Evolution of microstructure and mechanical properties of a graded TiAlON thin film investigated by cross-sectional characterization techniques, Surf. Coatings Technol. 359 (2019) 155–161. https://doi.org/10.1016/j.surfcoat.2018.12.058.

[157] M. Stefenelli, R. Daniel, W. Ecker, D. Kiener, J. Todt, A. Zeilinger, C. Mitterer, M. Burghammer, J. Keckes, X-ray nanodiffraction reveals stress distribution across an indented multilayered CrN–Cr thin film, Acta Mater. 85 (2015) 24–31. https://doi.org/10.1016/J.ACTAMAT.2014.11.011.

[158] A.P. Hammersley, S.O. Svensson, M. Hanfland, A.N. Fitch, D. Häusermann, Two-dimensional detector software: From real detector to idealised image or two-theta scan, High Press. Res. 14 (1996) 235–248. https://doi.org/10.1080/08957959608201408.

[159] J. Kieffer, D. Karkoulis, PyFAI, a versatile library for azimuthal regrouping, J. Phys. Conf. Ser. 425 (2013). https://doi.org/10.1088/1742-6596/425/20/202012.

[160] G. Ashiotis, A. Deschildre, Z. Nawaz, J.P. Wright, D. Karkoulis, F.E. Picca, J. Kieffer, The fast azimuthal integration Python library: PyFAI, J. Appl. Crystallogr. 48 (2015) 510–519. https://doi.org/10.1107/S1600576715004306.

[161] NIST 660c certificate, (n.d.). https://www-s.nist.gov/srmors/view_detail.cfm?srm=660c (accessed August 25, 2020).

[162] NIST 676a certificate, (n.d.). https://www-s.nist.gov/m-srmors/certificates/676a.pdf (accessed May 27, 2022).

[163] U. Welzel, J. Ligot, P. Lamparter, A.C. Vermeulen, E.J. Mittemeijer, Stress analysis of polycrystalline thin films and surface regions by X-ray diffraction, J. Appl. Crystallogr. 38 (2005) 1–29. https://doi.org/10.1107/S0021889804029516.

[164] I.C. Noyan, J.B. Cohen, Residual Stress: Measurement by Diffraction and Interpretation, illustrate, Springer, New York, 1987.

[165] L. Lutterotti, RietveldRefinements_LucaLutterotti.pdf, (2013) 1–56. http://www.ing.unitn.it/~luttero/laboratoriomateriali/RietveldRefinements.pdf.

[166] F. Bachmann, R. Hielscher, H. Schaeben, Texture analysis with MTEX - free and open source software toolbox, Solid State Phenom. 160 (2010) 63–68. https://doi.org/10.4028/www.scientific.net/SSP.160.63.

[167] L. Lutterotti, R. Vasin, H.R. Wenk, Rietveld texture analysis from synchrotron diffraction images. I. Calibration and basic analysis, Powder Diffr. 29 (2014) 76–84. https://doi.org/10.1017/S0885715613001346.

[168] Y. Kim, Y. Cho, S. Hong, S. Bühlmann, H. Park, D.K. Min, S.H. Kim, K. No, Correlation between grain size and domain size distributions in ferroelectric media for probe storage applications, Appl. Phys. Lett. 89 (2006). https://doi.org/10.1063/1.2363942.

[169] W. Cao, C.A. Randall, Grain size and domain size relations in bulk ceramic ferroelectric materials, J. Phys. Chem. Solids. 57 (1996) 1499–1505. https://doi.org/10.1016/0022-3697(96)00019-4.

[170] Y. Moritz, C. Kainz, M. Tkadletz, C. Czettl, M. Pohler, N. Schalk, Microstructure and mechanical properties of arc evaporated Ti(Al,Si)N coatings, Surf. Coatings Technol. 421 (2021) 127461. https://doi.org/10.1016/j.surfcoat.2021.127461.

[171] C. Kainz, M. Pohler, G.C. Gruber, M. Tkadletz, A. Sophie, C. Czettl, N. Schalk, Influence of bias voltage on microstructure, mechanical properties and thermal stability of arc evaporated $Cr_{0.74}Ta_{0.26}N$ coatings, Surf. Coatings Technol. 417 (2021) 127212. https://doi.org/10.1016/j.surfcoat.2021.127212.

[172] H.M. Rietveld, A profile refinement method for nuclear and magnetic structures, J. Appl. Crystallogr. 2 (1969) 65–71. https://doi.org/10.1107/s0021889869006558.

[173] R.E. Dinnebier, A. Leineweber, J.S.O. Evans, Rietveld Refinement: Practical Powder Diffraction Pattern Analysis using TOPAS, Walter de Gruyter GmbH & Co KG, Berlin/Boston, 2018.

[174] D. Baizar, H. Ledbetter, Accurate Modeling of Size and Strain Broadening in the Rietveld Refinement: The "Double-Voigt" Approach, Adv. X-Ray Anal. 38 (1994) 397–404. https://doi.org/10.1154/s0376030800018048.

[175] I. Krajinović, W. Daves, M. Tkadletz, T. Teppernegg, T. Klünsner, N. Schalk, C. Mitterer, C. Tritremmel, W. Ecker, C. Czettl, Finite element study of the influence

of hard coatings on hard metal tool loading during milling, Surf. Coatings Technol. 304 (2016) 134–141. https://doi.org/10.1016/j.surfcoat.2016.06.041.

[176] C. Saringer, M. Tkadletz, A. Stark, N. Schell, C. Czettl, N. Schalk, In-situ investigation of the oxidation behavior of metastable CVD $Ti_{1-x}Al_xN$ using a novel combination of synchrotron radiation XRD and DSC, Surf. Coatings Technol. 374 (2019) 617–624. https://doi.org/10.1016/j.surfcoat.2019.05.072.

[177] C. Saringer, C. Kickinger, F. Munnik, C. Mitterer, N. Schalk, M. Tkadletz, Thermal expansion of magnetron sputtered TiC_xN_{1-x} coatings studied by high-temperature X-ray diffraction, Thin Solid Films. (2019) 1–8. https://doi.org/10.1016/j.tsf.2019.05.026.

[178] C. Kainz, N. Schalk, C. Saringer, C. Czettl, In-situ investigation of the oxidation behavior of powdered TiN, Ti(C,N) and TiC coatings grown by chemical vapor deposition, Surf. Coatings Technol. 406 (2021) 126633. https://doi.org/10.1016/j.surfcoat.2020.126633.

[179] C. Kainz, C. Saringer, M. Burtscher, M. Tkadletz, A. Stark, N. Schell, M. Pohler, C. Czettl, D. Kiener, N. Schalk, Oxidation resistance of cathodic arc evaporated $Cr_{0.74}Ta_{0.26}N$ coatings, Scr. Mater. 211 (2022) 114492. https://doi.org/10.1016/j.scriptamat.2021.114492.

[180] Y. Moritz, C. Saringer, M. Tkadletz, A. Stark, N. Schell, I. Letofsky-papst, C. Czettl, M. Pohler, N. Schalk, Oxidation behavior of arc evaporated TiSiN coatings investigated by in-situ synchrotron X-ray diffraction and HR-STEM, Surf. Coat. Technol. 404 (2020) 126632. https://doi.org/10.1016/j.surfcoat.2020.126632.

[181] M. Tkadletz, C. Hofer, C. Wüstefeld, N. Schalk, M. Motylenko, D. Rafaja, H. Holzschuh, W. Bürgin, B. Sartory, C. Mitterer, C. Czettl, Thermal stability of nanolamellar fcc-$Ti_{1-x}Al_xN$ grown by chemical vapor deposition, Acta Mater. 174 (2019) 195–205. https://doi.org/10.1016/j.actamat.2019.05.044.

[182] F. Frank, M. Tkadletz, C. Czettl, N. Schalk, Microstructure and mechanical

properties of ZrN, ZrCN and ZrC coatings grown by chemical vapor deposition, Coatings. 11 (2021) 1–13. https://doi.org/10.3390/coatings11050491.

[183] G.W. Stinton, J.S.O. Evans, Parametric Rietveld refinement, J. Appl. Crystallogr. 40 (2007) 87–95. https://doi.org/10.1107/S0021889806043275.

[184] C. Xu, C. Huang, X. Ai, Cutting behavior and related cracks in wear and fracture of ceramic tool materials, Int. J. Adv. Manuf. Technol. 32 (2007) 1083–1089. https://doi.org/10.1007/s00170-006-0431-8.

[185] P.F. Becher, Crack Bridging Processes in Toughened Ceramics, Toughening Mech. Quasi-Brittle Mater. (1991) 19–33. https://doi.org/10.1007/978-94-011-3388-3_2.

[186] J. Zalesak, M. Bartosik, R. Daniel, C. Mitterer, C. Krywka, D. Kiener, P.H. Mayrhofer, J. Keckes, Cross-sectional structure-property relationship in a graded nanocrystalline $Ti_{1-x}Al_xN$ thin film, Acta Mater. 102 (2016) 212–219. https://doi.org/10.1016/j.actamat.2015.09.007.

[187] M. Tkadletz, N. Schalk, A. Lechner, L. Hatzenbichler, D. Holec, C. Hofer, M. Deluca, B. Sartory, A. Lyapin, J. Julin, C. Czettl, Influence of B content on microstructure, phase composition and mechanical properties of CVD Ti(B,N) coatings, Materialia. 21 (2022) 101323. https://doi.org/10.1016/j.mtla.2022.101323.

[188] H. Waldl, M. Tkadletz, C. Czettl, M. Pohler, N. Schalk, Influence of multilayer architecture on microstructure and fracture properties of arc evaporated TiAlTaN coatings, Surf. Coatings Technol. 433 (2022) 128098. https://doi.org/10.1016/j.surfcoat.2022.128098.

[189] C. Kainz, N. Schalk, M. Tkadletz, C. Mitterer, C. Czettl, The effect of B and C addition on microstructure and mechanical properties of TiN hard coatings grown by chemical vapor deposition, Thin Solid Films. (2019) 1–8. https://doi.org/10.1016/j.tsf.2019.05.002.

[190] F. Konstantiniuk, M. Tkadletz, C. Czettl, N. Schalk, Fracture Properties of α– and k–Al2O3 Hard Coatings Deposited by Chemical Vapor Deposition, Coatings. 11

(2021) 1359. https://doi.org/10.3390/coatings11111359.

[191] K. Matoy, H. Schönherr, T. Detzel, T. Schöberl, R. Pippan, C. Motz, G. Dehm, A comparative micro-cantilever study of the mechanical behavior of silicon based passivation films, Thin Solid Films. 518 (2009) 247–256. https://doi.org/10.1016/j.tsf.2009.07.143.

[192] A. Riedl, R. Daniel, M. Stefenelli, T. Schöberl, O. Kolednik, C. Mitterer, J. Keckes, A novel approach for determining fracture toughness of hard coatings on the micrometer scale, Scr. Mater. 67 (2012) 708–711. https://doi.org/10.1016/j.scriptamat.2012.06.034.

[193] D. Di Maio, S.G. Roberts, Measuring fracture toughness of coatings using focused-ion-beam-machined microbeams, J. Mater. Res. 20 (2005) 299–302. https://doi.org/10.1557/JMR.2005.0048.

[194] D. Gross, T. Seelig, Fracture Mechanics: With an Introduction to Micromechanics, 3rd ed., Springer, 2018.

7 Publications

7.1 List of included publications

I. **Microstructure and mechanical properties of ZrN, ZrCN and ZrC coatings grown by chemical vapor deposition**

Florian Frank, Michael Tkadletz, Christoph Czettl, Nina Schalk

Coatings 11 (2021) 491.

II. **In-situ investigation of the oxidation behaviour of chemical vapour deposited Zr(C,N) hard coatings using synchrotron X-ray diffraction**

Florian Frank, Michael Tkadletz, Christian Saringer, Andreas Stark, Norbert Schell, Marco Deluca, Christoph Czettl, Nina Schalk

Coatings 11 (2021) 264.

III. **Microstructural and micro-mechanical investigation of cathodic arc evaporated ZrN/TiN multilayer coatings with varying bilayer thickness**

Florian Frank, Christina Kainz, Michael Tkadletz, Christoph Czettl, Markus Pohler, Nina Schalk

Surface and Coatings Technology 432 (2022) 128070.

IV. **Investigation of the microstructure of a graded ZrN/Ti$_{0.33}$Al$_{0.67}$N multilayer coating using cross-sectional characterization methods**

Florian Frank, Michael Tkadletz, Christian Saringer, Christoph Czettl, Markus Pohler, Manfred Burghammer, Juraj Todt, Jakub Zalesak, Jozef Keckes, Nina Schalk

Under review in Surface and Coatings Technology (2022)

Publication I

Microstructure and mechanical properties of ZrN, ZrCN and ZrC coatings grown by chemical vapour deposition

Florian Frank, Michael Tkadletz, Christoph Czettl, Nina Schalk

In-situ investigation of the oxidation behaviour of chemical vapour deposited Zr(C,N) hard coatings using synchrotron X-ray diffraction

Florian Frank[1], Michael Tkadletz[2], Christoph Czettl[3], Nina Schalk[1]

[1] Christian Doppler Laboratory for Advanced Coated Cutting Tools at the Department of Materials Science, Montanuniversität Leoben, Franz–Josef–Strasse 18, 8700 Leoben, Austria

[2] Department of Materials Science, Montanuniversität Leoben, Franz–Josef–Strasse 18, 8700 Leoben, Austria

[3] Ceratizit Austria GmbH, Metallwerk–Plansee–Strasse 71, 6600 Reutte, Austria

Abstract

As the demands for wear resistant coatings in the cutting industry are constantly rising, new materials that have the potential to exhibit enhanced coating properties are continuously explored. Chemical vapour deposited (CVD) Zr(N,C) is a promising alternative to the well-established and thoroughly investigated Ti(C,N) coating system, owing to its advantageous mechanical and thermal properties. Thus within this work, CVD ZrN, ZrCN and ZrC coatings were deposited at 1000 °C and subsequently their microstructure and mechanical properties were investigated in detail. Scanning electron microscopy, electron backscatter diffraction and X-ray diffraction experiments revealed that all coatings exhibit a columnar structure and a fibre texture, where ZrN and ZrCN displayed a <100> preferred orientation in growth direction and ZrC showed a <110> texture. Tensile residual stresses that arise due to a mismatch in the coefficient of thermal expansion between the cemented carbide substrate and the coating material decrease with the addition of C to the coatings. No stress relaxation through thermal crack formation was observed in the coatings. The highest hardness was determined for ZrC with

28.1 ± 1.0 GPa and the lowest for ZrN with 22.1 ± 0.9 GPa. Addition of C to ZrN increased the hardness to 26.1 ± 1.6 GPa, which can be explained by a more covalent bonding character, as well as by solid solution strengthening. ZrCN exhibits the highest Young's modulus followed by ZrC and ZrN, which can be attributed to differences in their electronic band structure.

Keywords: CVD; Zr(C,N); hard coatings; texture; hardness

1. Introduction

Protective hard coatings for cemented carbide cutting tools are frequently used to improve the cutting performance [1]. While chemically vapour deposited (CVD) TiN, TiCN and TiC coatings have been intensively investigated and widely used for several decades [2–8], literature on alternative CVD transition metal nitride, carbonitride and carbide coatings is limited. However, some reports suggest advantageous mechanical and thermal properties of Zr(C,N) over Ti(C,N) coatings [9–11]. A study of Garcia et al. revealed a significantly improved cutting performance of CVD ZrCN compared to TiCN coated inserts in wet milling of cast iron [10]. Based on these findings, detailed micromechanical, as well as contact damage investigations were conducted by El Azhari et al. on both, CVD ZrCN and TiCN coatings, yielding a better cohesive strength and higher intrinsic plasticity of ZrCN [12,13]. Literature discussing the mechanical properties of CVD ZrN and ZrC is quite scarce. Russel observed a significantly lower coefficient of friction for CVD ZrN compared to TiN, which indicates an enhanced performance in machining applications [14]. Long et al. compared non-stoichiometric ZrC$_{0.85}$ coatings to stoichiometric ZrC coatings and found higher hardness and Young's modulus values for the latter [15]. Analogously to TiN and TiC, a higher hardness can be expected for ZrC due to its increased covalent contribution to the bond strength compared to ZrN [16].

Besides the few available studies on the mechanical properties of the Zr(C,N) system, several authors have investigated the influence of varying deposition parameters in the CVD process on the microstructure of the coatings [14,17–22]. The coatings were synthesised within a temperature range between 800 and 1550 °C and, depending on the deposition temperature, variations in the surface morphology, as well as the preferred orientation of the coatings were found. These microstructural differences occur due to a change in the deposition process from gas nucleation at lower temperatures to surface kinetic processes at temperatures above 1250 °C. Smooth and dense coatings were only observed in the surface kinetic regime, suggesting that high deposition temperatures (>1250 °C) are beneficial, although the exact temperature range might vary for different deposition facilities [19–21].

However, it needs to be kept in mind that deposition processes carried out at high temperatures consume great quantities of energy. Consequently, from an economic point of view, the deposition of coatings on the industrial scale with comparable mechanical properties at lower temperatures is desirable, although limitations for the lowest possible deposition temperature have to be considered. Investigations of ZrN deposited at 800 to 1000 °C from a $ZrCl_4$-NH_3-N_2-H_2 precursor system in a laboratory CVD chamber by Rauchenwald et al. have shown that a deposition temperature below 900 °C leads to the formation of ZrClN structures in the coatings [22]. This Cl contamination can deteriorate the mechanical properties of the coatings [7,17,23–26]. Nevertheless, a lower deposition temperature could have beneficial effects on stress formation and therefore on the crack network within the coatings. In CVD coatings, typically tensile residual stresses are observed, which result from a mismatch in the coefficient of thermal expansion (CTE) between coating and substrate material and the high deposition temperatures. One intrinsic advantage of Zr(C,N) over Ti(C,N) is its lower CTE, which is thus closer to the CTE of the cemented carbide substrates, resulting in lower tensile stresses in the coatings deposited at the same deposition temperature [13,27]. Since tensile stresses can lead to the

formation of cracks in the coatings, it would be beneficial to decrease the deposition temperature during synthesis of Zr(C,N) coatings as much as possible to further reduce the tensile stresses, while still depositing smooth and dense coatings without Cl contamination [13,28].

Thus, within this study CVD ZrN, ZrCN and ZrC coatings were deposited from three different precursor systems $ZrCl_4$-N_2-H_2, $ZrCl_4$-CH_3CN-H_2 and $ZrCl_4$-CH_4-H_2, respectively, using an industrial scale deposition plant. The deposition temperature was kept constant at 1000 °C and the microstructure and mechanical properties of the coatings were investigated in detail. The elemental composition was studied by energy dispersive X-ray spectroscopy (EDX). X-ray diffraction (XRD) analysis and scanning electron microscopy (SEM) gave insight into the microstructure, as well as the phase composition of the Zr(C,N) coatings. Cross-sectional analysis with electron backscatter diffraction (EBSD), as well as XRD pole figure (PF) measurements allowed to study the grain size and the crystallographic texture of the coatings. Special emphasis was laid on the investigation of the residual stresses of the coatings, which were evaluated applying the $\sin^2\psi$ method. The mechanical properties were determined by nanoindentation.

2. Materials and Methods

ZrN, ZrCN and ZrC coatings were deposited in a Sucotec SCT600TH (Sucotec, Langenthal, Switzerland) industrial scale hot-wall CVD plant. In addition to the solid Zr precursor chlorinated beforehand, a mixture of N_2, CH_3CN, and CH_4 with H_2 as carrier gas was used to synthesize the Zr(C,N) samples. The deposition parameters are summarized in Table 1. The deposition temperature was 1000 °C for all three systems, while the total pressure varied between 10 kPa (ZrCN) and 16 kPa (ZrN and ZrC), depending on the individual gas flow rates of all precursors. A TiN baselayer was deposited prior to the Zr(C,N) layer to hinder diffusion processes and enhance the coatings adherence to the substrate. The baselayer was synthesised using the precursors $TiCl_4$, N_2 and H_2 at 1000 °C and a deposition time of 60 min. Cemented carbide in SNUN

geometry according to ISO 1832 and mild steel foils were used as substrate material. The composition of the cemented carbide was 92 wt.% WC, 6 wt.% Co and 2 wt.% mixed carbides. To determine the stress free lattice parameter of the coatings, the mild steel foils were dissolved after deposition using nitric acid and a powder of the coating was produced.

Table 1. *Deposition parameters (time, temperature, total pressure and gas flow rates) for ZrN, ZrCN and ZrC.*

Sample	Time [min]	Temperature [°C]	Pressure [kPa]	H_2 (balance) [vol.%]	N_2 [vol.%]	CH_3CN [vol.%]	CH_4 [vol.%]
ZrN	260	1000	16	76	24	-	-
ZrCN	260	1000	10	99.9	-	2.2×10^{-5}	-
ZrC	260	1000	16	94	-	-	6

The quantitative elemental composition of the coatings was determined by EDX using an Oxford Ultim Extreme spectrometer (Oxford Instruments, Abingdon, Oxfordshire, England) mounted on a Zeiss GeminiSEM 450 (Carl Zeiss AG, Oberkochen, Germany). Microstructural analysis of the solid and powdered coatings was conducted applying a Bruker D8 Advance X-ray diffractometer (Bruker AXS, Karlsruhe, Germany) in locked coupled mode ($\theta = \theta$) in parallel beam configuration using Cu Kα ($\lambda = 1.5418$ Å) radiation. The diffractograms were recorded with a step size of 0.02° and a measuring time of 1.2 s per step, utilizing an energy dispersive Sol-X detector. To determine the stress free lattice parameter, XRD patterns of the coating powders were recorded and evaluated by Rietveld refinement using the software TOPAS 6 supplied by Bruker AXS. The coating surfaces as well as cross sections were investigated using the above mentioned SEM. The cross sections were prepared with a Hitachi IM4000+ ion milling system (Hitachi, Chiyoda City, Tokyo, Japan) utilizing Ar+ ions. EBSD investigations to determine the grain size and orientation were conducted on the mentioned SEM employing an Oxford Symmetry EBSD camera. The scanning step size was 20 nm and the accelerating voltage was set to 10 kV. Complementary, XRD PF measurements were performed on a Bruker D8 Advance DaVinci diffractometer using Cu Kα radiation and a position sensitive LynxEye XE-T

detector. A half-circle Eulerian cradle was used to tilt and rotate the sample. The PFs of all three samples were recorded for the 111, 200 and 220 peaks at tilt angles from 0° up to 84°. The data processing, as well as the visualisation of the recalculated PFs and the inverse pole figures (IPF) was conducted utilizing the MTEX toolbox [29].

The residual stresses were determined using the $\sin^2\psi$ method in side-inclination [30]. The measurements were carried out on the Bruker D8 Advance DaVinci diffractometer described above, employing the same experimental parameters as for the PF measurement. Nine equally spaced inclinations from 0–0.8 $\sin^2\psi$ were considered in the residual stress evaluation, using the 220 reflection for all coatings. The respective X-ray elastic constants were calculated employing the Hill grain interaction model [31], where elastic constants from literature were used as input [32]. Hardness as well as Young's modulus were determined by nanoindentation using an Ultra Micro Indentation System (UMIS) system from Fischer–Cripps Laboratories equipped with a diamond Berkovich indenter tip. Prior to the measurements, the surfaces of the samples were mirror polished. In order to reduce the influence of the TiN baselayer and the substrate on the hardness and the elastic modulus, a plateau test with penetration depths <10% of the respective Zr(C,N) film thickness was conducted. The data was evaluated according to the Oliver and Pharr method [33].

3. Results and Discussion

3.1. Chemical composition and microstructure

The elemental analysis obtained from EDX showed a mean Zr content of ~50 at.% for the ZrN and slightly lower values of ~45 at.% for the ZrCN and ZrC coating. Small amounts of C (~7 at.%) were detected in the ZrN sample, which can be related to residual CH_3 precursor in the feed gas line. However, due to the limitations of EDX to detect light elements like C and N, these values have to be treated carefully. A Cl contamination could not be observed in the Zr(C,N) coatings, which can be related to the deposition temperature >900 °C and high H_2 carrier gas flow rate [22]. H_2 acts as reductant agent for

the dissociation of $ZrCl_4$ into $ZrCl_3$, $ZrCl_2$ and $ZrCl$ subchlorides and its presence is necessary to reduce Cl contamination. The ZrCN sample contained ~21 at.% N and ~34 at.% C, which leads to a normalised composition of $ZrC_{0.62}N_{0.38}$ regarding the C/(C+N) ratio. This C/(C+N) ratio is in good agreement with ratios obtained for CVD TiCN coatings deposited from the $TiCl_4$-CH_3CN-H_2 system at temperatures >850 °C [34–36]. In addition to the mean coating composition, also cross-sectional EDX spectra were determined at different depths for ZrCN. The results are shown in Figure 1a. The analysis reveals an increase in C content of ~7 at.% towards the TiN baselayer. The origin of this C increase is not completely clear. Even though the TiN baselayer acts as diffusion barrier, the diffusion of small amounts of C from the cemented carbide substrate through this layer cannot be excluded [37]. The C increase may also arise from the precursor gas due to not optimized process parameters.

X-ray diffractograms of all three coating systems are displayed in Figure 1b. The standard peak positions of face-centred cubic (fcc)–ZrN (PDF 00-035-0753 [38]), fcc–ZrC (PDF 00-035-0784 [38]), fcc–TiN (PDF 00-038-1420 [38]) and WC (PDF 00-051-0939 [38]) arising from the cemented carbide substrate, are plotted as dashed lines. All Zr(C,N) layers, as well as the TiN baselayer, exhibit a fcc structure. The peaks of the ZrN and ZrC coatings are in good agreement with the standard peak positions, while the ZrCN peak lies between the ZrN and ZrC peaks, due to the formation of a solid solution. A detailed Rietveld refinement of the XRD patterns of the powdered coatings revealed a lattice parameter of 4.58 ± 0.01 Å and 4.70 ± 0.01 Å for ZrN and ZrC, respectively, which is in excellent agreement with the lattice parameters given in the respective ICDD cards (4.58 Å for ZrN and 4.69 Å for ZrC). Considering the formation of a solid solution and a Vegard's like behaviour, the determined lattice parameter for ZrCN of 4.63 ± 0.01 Å leads to a normalised composition of $ZrC_{0.39}N_{0.61}$, which is in contrast to the EDX measurement yielding $ZrC_{0.62}N_{0.38}$. This deviation can most probably be attributed to excess C in the

coating, which is not incorporated in the ZrCN lattice and consequently does not affect the lattice parameter.
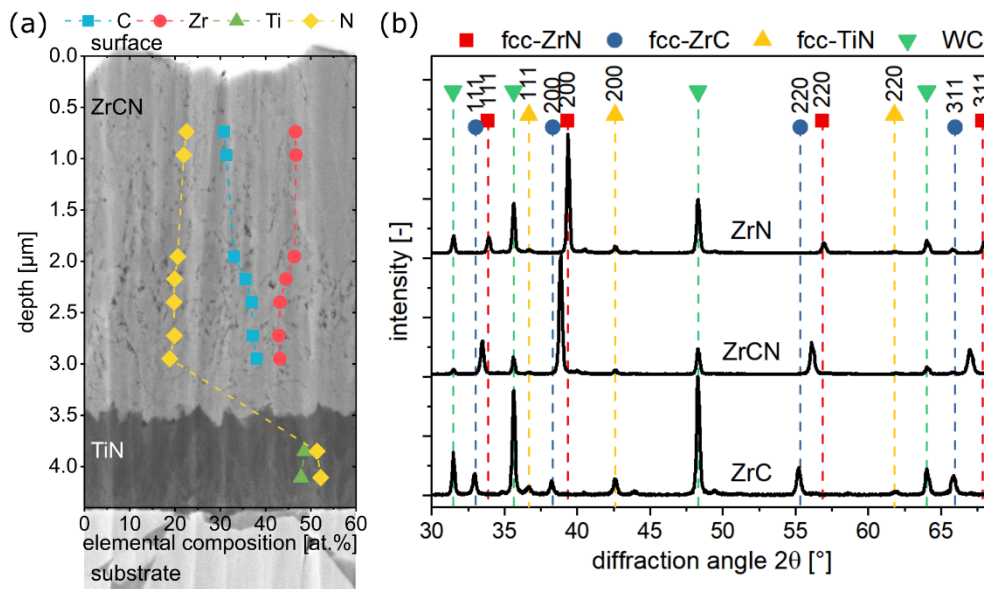
Figure 1. *(a) Cross-sectional SEM image, superimposed by the elemental composition of the ZrCN coating determined by EDX at different depths in the ZrCN coating and (b) X-ray diffractograms of ZrN, ZrCN and ZrC coatings on cemented carbide substrates with TiN baselayer.*

In Figure 2a, SEM micrographs of the surfaces of ZrN, ZrCN and ZrC are shown. ZrN exhibits a needle-like (lenticular) surface morphology, which was also reported by Russel et al. for CVD ZrN coatings, deposited at temperatures below 1050 °C [14]. The surface of ZrCN shows a rugged and apparently porous structure. Kudapa et al. observed a needle-like surface morphology for CVD ZrCN coatings, deposited at moderate temperatures [18]. Similar to ZrN, the surface morphology of ZrC is also needle-like. However, while the length of the needles is comparable (~1 µm), the aspect ratio is smaller for ZrC compared to ZrN. Focused ion beam (FIB) prepared cross sections of all three coatings are depicted in Figure 2b. The TiN baselayer and the respective ZrN, ZrCN and ZrC layer can be clearly distinguished. A difference in coating thickness between the three samples is clearly visible. While the ZrN and ZrC layers show a comparable thickness of 0.99 ± 0.09 µm and 0.87 ± 0.06 µm, respectively, the ZrCN layer exhibits a thickness of

3.53 ± 0.13 µm. Since the deposition time and the temperature were constant for all three coatings, the different feed gas composition is assumed to be mainly responsible for the variations in the coating thickness and consequently the deposition rate. In addition to the different reactivity of the three precursors CH_3CN, CH_4 and N_2, also the H_2 carrier gas flow rate can influence the coating thickness [22]. The deposition rate was the highest for ZrCN with 0.81 ± 0.01 µm/h, while the rates for ZrN and ZrC were 0.23 ± 0.01 µm/h and 0.20 ± 0.01 µm/h respectively. These results indicate a high yield from the CH_3CN precursor, used for the deposition of ZrCN and significantly lower yields for the deposition with N_2 and CH_4 for ZrN and ZrC, respectively, at identical deposition temperatures of 1000 °C. This can be attributed to the lower energy needed for the dissociation of the organic CH_3CH precursor than for N_2 and CH_4 [35,36,39]. Competitive growth can be observed for the TiN baselayer of all coatings. The smaller grains at the interface are followed by columnar grains, which extend through the baselayer. Within the ZrN and ZrC layers columnar grains, extending through the whole layer, can be observed. In the ZrCN cross section, columnar grains are visible as well, but they do not extend through the whole layer. The grain growth is repeatedly interrupted, especially at the beginning of the layer. Furthermore, the mean grain length in growth direction increases in size with increasing coating thickness, which is typical for the competitive growth mechanism [40,41]. The porous structure of the ZrCN coating, supposed from the surface micrograph, is also evident in the cross section. The pores might be related to the excess C which is not incorporated in the ZrCN lattice, as shown by EDX and XRD analysis (Figure 1). It appears that the number of pores increases towards the TiN interface, which is in good agreement with the accompanied increase in C content (Figure 1a). Both the surfaces and the cross sections of all coatings were inspected by SEM on a bigger scale (115 × 115 µm² surface and 11 × 11 µm² cross section, images not shown) and no cracks were found.
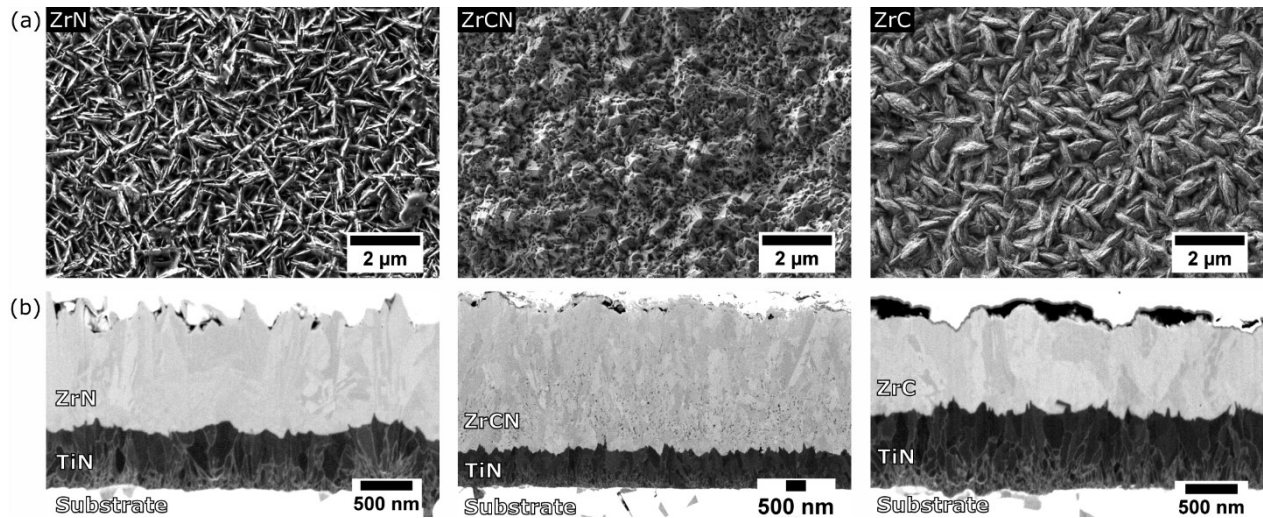
Figure 2. (a) SEM surface images and (b) FIB prepared cross sections of ZrN, ZrCN and ZrC. Note the different scale bar in the cross section micrograph of the ZrCN coating.

To gain further insight into the microstructure of the coatings, detailed EBSD investigations, shown in Figure 3, were conducted. On the far left side, the respective band contrast images, corresponding to the inverse pole maps in growth direction (IPF– Y maps) on the right side, are shown. The orientation of the grains is colour coded. The colour code valid for the coating is given at the bottom right of Figure 3. Please note that this colour code is not valid for the substrate, which is not in the focus of this work. The competitive growth in the TiN layer already seen in the FIB cross section micrographs in Figure 2b is also visible in the EBSD images for all coatings. In the ZrN layer (Figure 3a) mainly columnar grains are present that extend through the whole layer. The ZrCN layer (Figure 3b) exhibits a heterogeneous distribution of columnar grains and small globular grains at the TiN/ZrCN interface. As already mentioned above, the columnar grains, as well as the globular grains, increase in size with the layer thickness. Similar to ZrN, ZrC (Figure 3c) exhibits columnar grains which extend over the whole thickness of the layer, however, compared to ZrN also some rounder grains with lower aspect ratio are observed. The broader appearance of the grains is in good agreement with the surface micrograph (Figure 2a), where also broader needles were observed for ZrC compared to ZrN. The grain orientation in growth direction seems random for all three coatings and

considering only the EBSD images, no clear statement can be made regarding a preferred orientation of the coatings. Due to the small cross sections in relation to the grain sizes, a statistical evaluation of the grain orientation distribution was not considered.
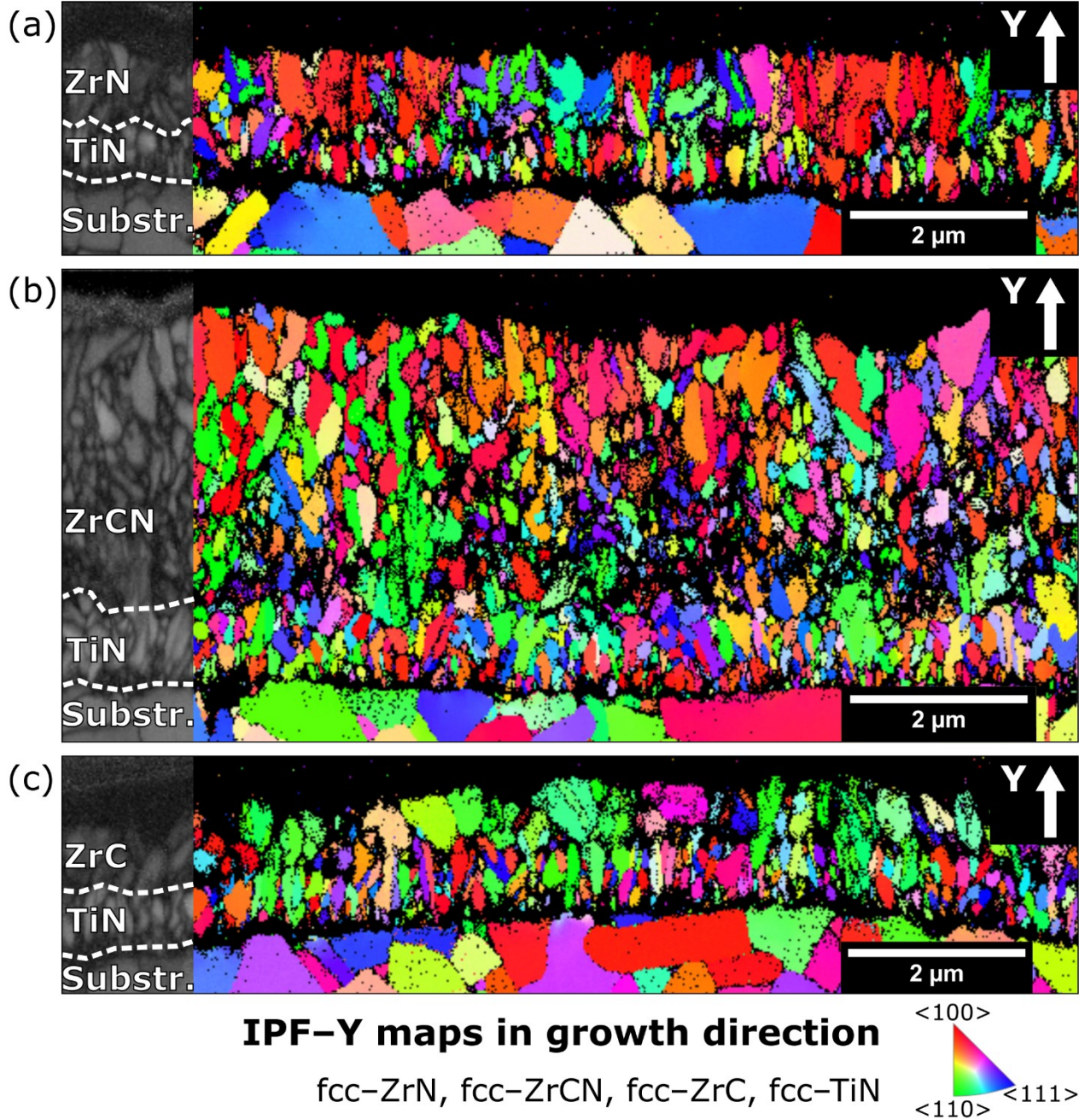

Figure 3. *EBSD inverse pole figure (IPF) maps of the ion sliced cross section in growth direction ("IPF–Y maps") for (a) ZrN, (b) ZrCN and (c) ZrC. The respective Zr(C,N) and TiN layers are indicated in the EBSD band contrast sections on the left. The IPF–Y colour code is given at the bottom right for face-centred cubic (fcc) phases.*

Therefore, to gain further insight into the texture of the coatings, XRD PFs were recorded. The recalculated PFs of the 111, 200 and 220 reflexes, as well as the calculated IPFs in growth direction are shown in Figure 4a–c for ZrN, ZrCN and ZrC, respectively. The intensities of the PFs are normalised within each coating system. All PFs exhibit rotational symmetric intensity distributions, indicating a fibre texture for all coating systems. The IPFs for ZrN (Figure 4a) and ZrCN (Figure 4b) reveal a distinct <100> preferred orientation. These results are in good agreement with the XRD patterns (Figure 1b), where 200 was identified as the strongest peak for ZrN and ZrCN. Russel found a <100> preferred orientation for ZrN coatings deposited at 1050 °C and a <111> or <110> preferred orientation for coatings deposited at lower temperatures of ~900 to 975 °C, indicating a pronounced texture dependency on the deposition temperature [14]. As opposed to ZrN and ZrCN, the IPF of ZrC (Figure 4c) exposes a <110> preferred orientation in growth direction. However, the texture is not that pronounced and some grains are oriented in <111>, <210> and <211> direction. Although the layer thickness might influence the texture of the coatings [35], a change in texture could also be related to the different precursor compositions, as ZrN and ZrC exhibited a similar thickness but different texture. Park et al. investigated the influence of the H_2 concentration on the microstructure of ZrC coatings, using a $ZrCl_4$-CH_4-H_2-Ar precursor system at temperatures of 1350 °C. They varied the H_2 to Ar gas ratio and found that a high H_2 concentration is accompanied by a 220 preferred orientation, in contrast to low H_2 concentrations that lead to 111 and 200 orientations [42]. The same effect of the H_2 concentration on the texture in CVD ZrC coatings, deposited from different precursor systems with temperatures >1000 °C, was observed by several researchers [19,43,44]. One possible explanation for this change in texture was given by Imai et al. and can be related to a varying critical size for nucleus growth in different crystallographic orientations with changing supersaturation of the precursor gases. Hereby, the preferred orientation changes from 111 to 001 and 110 with increasing H_2 partial pressure [45]. Since the H_2

concentration was high for the deposition of ZrC, the results of the texture analysis are in accordance with these reports.
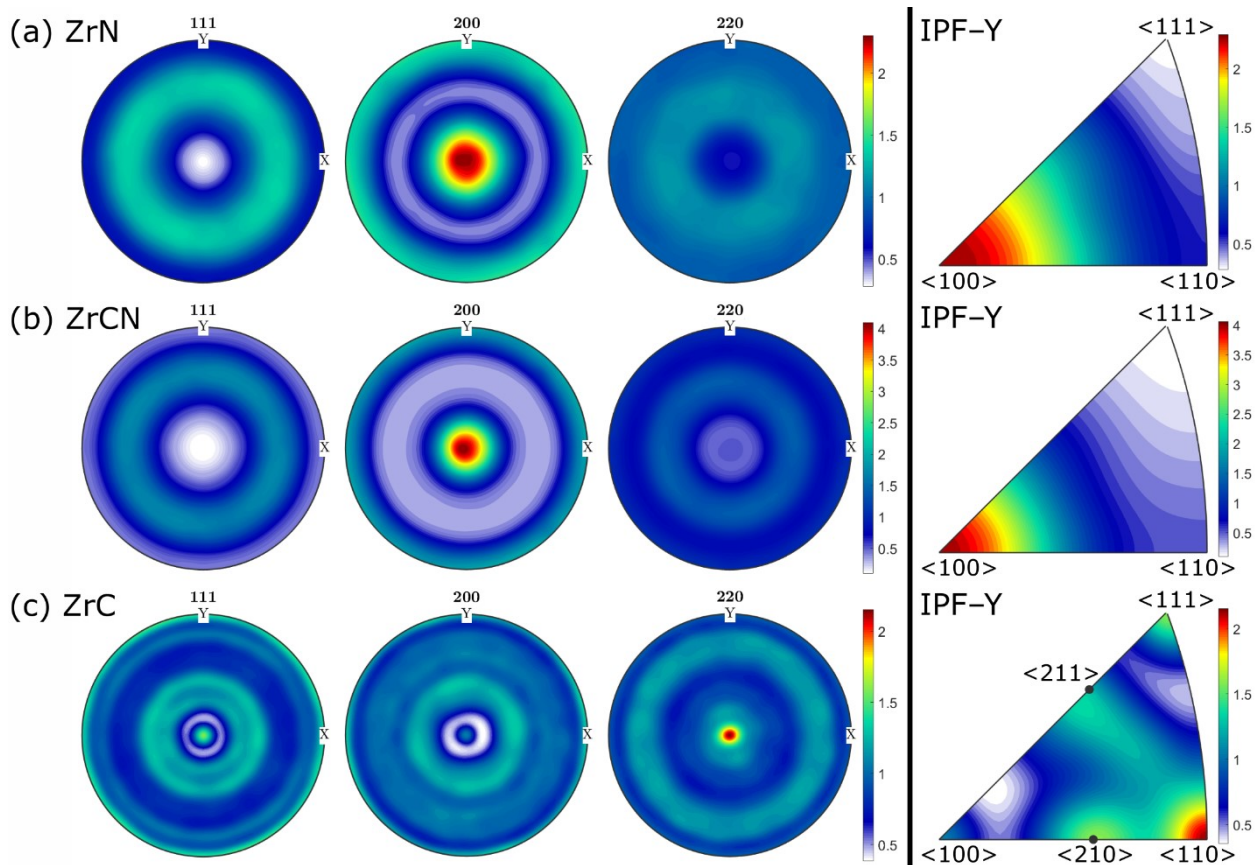
Figure 4. *Recalculated X-ray diffraction pole figures for the (a) ZrN, (b) ZrCN and (c) ZrC coatings with their corresponding IPFs in growth direction ("IPF–Y") on the right side.*

3.2. Residual stress and mechanical properties

The determined residual stresses are displayed in Figure 5a. All coatings show tensile stresses that arise due to the mismatch in the CTE between the substrate and the coating material (ΔCTE) [19]. According to literature, the CTEs for ZrN and ZrC are 7.2×10^{-6} K^{-1} and 6.7×10^{-6} K^{-1}, respectively [47]. Considering the determined composition for ZrCN, a linear interpolation of these two values yields a CTE of 6.95×10^{-6} K^{-1}. Consequently, the CTE of all coatings is higher compared to the one of the cemented carbide substrate (5.7×10^{-6} K^{-1} [46]), resulting in a more pronounced contraction of the coating than the substrate material during the cooling process after deposition [13]. The

observed decrease of the tensile stresses from ZrN over ZrCN to ZrC is in agreement with the CTEs of the individual coating systems. Since the main contribution to the stress state in CVD coatings is thermal stress ($\sigma_{thermal}$), the calculated values for these stresses are shown as a comparison to the measured residual stresses. $\sigma_{thermal}$ was calculated according to Gao et al. [48] using

$$\sigma_{thermal} = \frac{E_c}{1-\nu_c} \, (\alpha_c - \alpha_s)\Delta T, \tag{1}$$

where E is the Young's modulus, ν the Poisson's ratio, $\alpha_{c,s}$ the CTE, ΔT is the difference between the deposition and the room temperatures and the subscripts c and s denote the coating or the substrate, respectively. The corresponding values for E and ν were obtained from literature [32]. Although the theoretical thermal stresses follow the trend of the measured residual stresses, deviations of ~260 GPa and ~230 GPa can be observed for ZrCN and ZrC, respectively. The source of these deviations is not clear, however, it can be speculated that some form of stress relaxation mechanism either during coating growth or the cooling process might take place. Since no stress relaxation through crack formation was observed, either plastic deformation of the cemented carbide substrate upon cooling might take place [27], or, as El Azhari et al. suggested, compressive intrinsic stresses, like defect incorporation, formation of non-equilibrium structures or grain boundary relaxation, develop during the deposition process [13]. Due to the mainly thermal dominated stresses in CVD coatings, the differences in the coating thickness are expected to play a minor role for the residual stresses. By employing the classical laminate theory, residual stresses of the substrate-coating system can be calculated and the influence of the layer thickness on the stress state in the individual layers can be estimated [49–51]. Since the thickness of the substrate is ~4.5 mm, variations in the comparably thin Zr(C,N) layer thickness from 1 µm to 5 µm lead to no significant influence on the residual stress state in the Zr(C,N) layer. Thus it is assumed that the residual stress measurements are comparable between the three coatings, although the layer thickness varies between ~1 µm (ZrN, ZrC) and ~3.5 µm (ZrCN).

Hardness and Young's modulus of the Zr(C,N) coatings are shown in Figure 5b. With the addition of C to ZrN a hardness increase from 22.1 ± 0.9 GPa for ZrN to 26.1 ± 1.6 GPa for ZrCN is observed. This enhancement can be attributed to solid solution strengthening, as well as an increase of the covalent contribution to the bond strength between the p–states originating from C and the d–states from Zr [16]. ZrC exhibits an even higher hardness of 28.1 ± 1.0 GPa, which complies with the stronger covalent bonding characteristics. This trend of increasing hardness with increasing C/(C+N) ratio was also observed by Yang et al. in Zr(C,N) bulk materials [52]. Furthermore, the Young's modulus is as well affected by the C and N content and shows a maximum for ZrCN (514 ± 19 GPa), followed by a slightly lower value for the ZrC coating (472 ± 22 GPa), while ZrN exhibits the lowest value of 428 ± 10 GPa. This trend is expected and confirmed by first-principles density functional theory calculations by Ivashchenko et al., as well as by experimental findings for Zr(C,N) and Ti(C,N), and can be related to the electronic band structure of the coatings [32,52–54]. The influence of the observed pores in the ZrCN coating on the Young's modulus is expected to be minor, since the porosity is low and the pores are mainly located close to the interface to the TiN baselayer [55]. Hardness and Young's modulus are not only determined by the electronic band structure, but also by the microstructure and the coating thickness. As the grain size tends to increase with increasing coating thickness as a result of competitive growth, a dependency of the hardness and the Young's modulus on the coating thickness cannot be excluded [40,41,56].
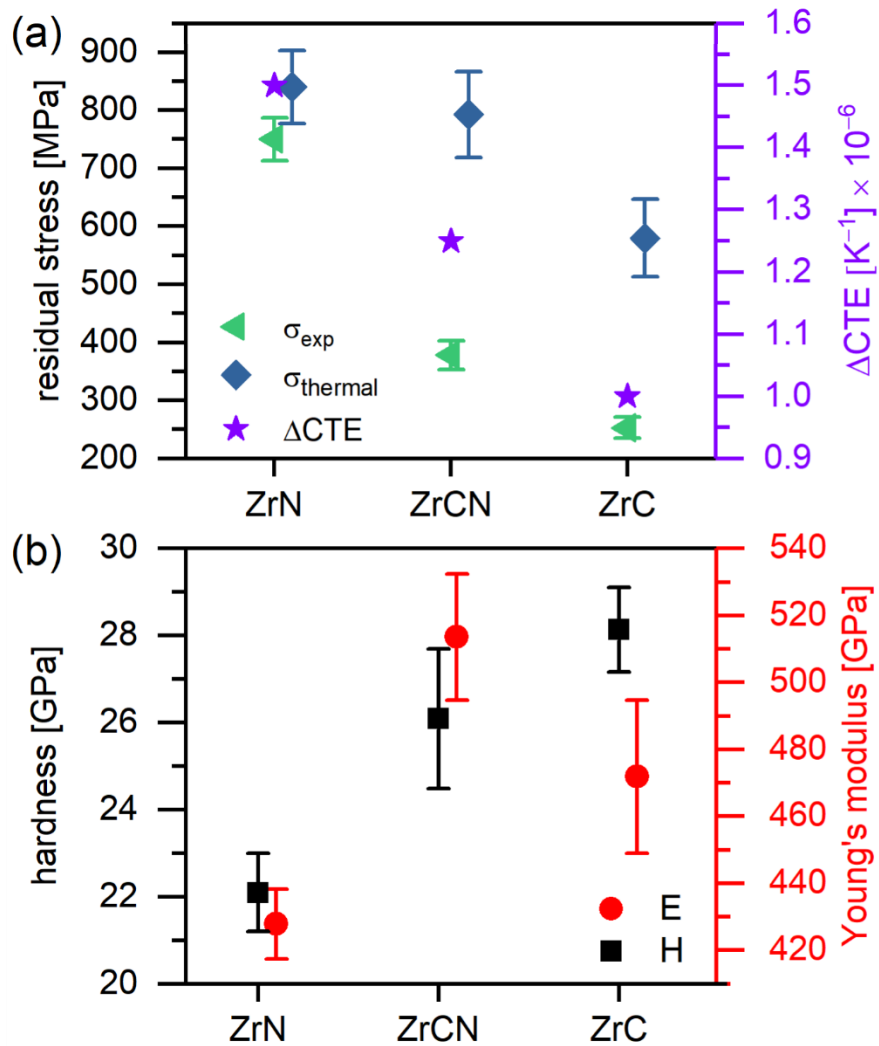
Figure 5. *(a) Experimentally determined (σ_{exp}) and calculated thermal stresses ($\sigma_{thermal}$) as well as CTE mismatch (ΔCTE) between the substrate and the investigated Zr(C,N) coatings. (b) Hardness (H) and Young's modulus (E) of the Zr(C,N) coatings.*

4. Conclusions

Within this study, ZrN, ZrCN and ZrC coatings were successfully deposited by chemical vapour deposition on industrial scale at 1000 °C, using the precursors $ZrCl_4$-N_2-H_2, $ZrCl_4$-CH_3CN-H_2 and $ZrCl_4$-CH_4-H_2, respectively. The microstructure and mechanical properties of the coatings were investigated. The considerably higher deposition rate for the ZrCN coating with 0.81 ± 0.01 μm/h compared to 0.23 ± 0.01 μm/h and 0.20 ± 0.01 μm/h for ZrN and ZrC, respectively, can be related to the higher reactivity of

the organic CH_3CN precursor compared to the less reactive N_2 and CH_4. ZrN and ZrC showed a needle-like surface morphology for ZrN and ZrC, whereas the ZrCN coating exhibited a rugged and porous structure. Columnar grain growth and fibre texture was observed in all three coatings. While the ZrN and ZrCN coatings exhibit a preferred <100> orientation in growth direction, the ZrC showed a <110> texture with few grains oriented in <111>, <210> and <211> direction. These differences in texture are associated with the high H_2 precursor concentration in the ZrC coating. The tensile residual stresses decrease from ZrN over ZrCN to ZrC, which can be attributed to the decreasing mismatch in the coefficient of thermal expansion between the cemented carbide substrate and coating material. Upon C addition, the hardness of the coatings increased as a result of solid solution strengthening, as well as the more pronounced covalent bonding character, leading to the lowest values of 22.1 ± 0.9 GPa for ZrN, followed by 26.1 ± 1.6 GPa for ZrCN and 28.1 ± 1.0 GPa for ZrC, respectively. The Young's modulus shows a maximum for the ZrCN coating of 514 ± 19 GPa, followed by ZrC with 472 ± 22 GPa and ZrN with 428 ± 10 GPa. In conclusion, the present work provides a fundamental understanding of the microstructure and mechanical properties of CVD Zr(C,N) coatings and is a first step towards the future optimisation of this coating system on an industrial scale.

5. Acknowledgments

(BMDW), represented by the Austrian research funding association (FFG), and the federal states of Styria, Upper Austria and Tyrol.

6.   References

[1]   Mitterer, C. PVD and CVD Hard Coatings. In *Comprehensive Hard Materials*; Sarin, V.K.., Ed.; Elsevier Ltd: Amsterdam, 2014; Vol. 2, pp. 449–467 ISBN 9780080965284.

[2]   Kainz, C.; Schalk, N.; Tkadletz, M.; Mitterer, C.; Czettl, C. Microstructure and mechanical properties of CVD TiN/TiBN multilayer coatings. *Surf. Coatings Technol.* **2019**, *370*, 311–319, doi:10.1016/j.surfcoat.2019.04.086.

[3]   Schintlmeister, W.; Wallgram, W.; Kranz, J.; Gigl, K. Cutting tool materials coated by chemical vapour deposition. *Wear* **1984**, *100*, 153–169.

[4]   Kainz, C.; Schalk, N.; Tkadletz, M.; Mitterer, C.; Czettl, C. The effect of B and C addition on microstructure and mechanical properties of TiN hard coatings grown by chemical vapor deposition. *Thin Solid Films* **2019**, 1–8, doi:10.1016/j.tsf.2019.05.002.

[5]   Wagner, J.; Mitterer, C.; Penoy, M.; Michotte, C.; Wallgram, W.; Kathrein, M. The effect of deposition temperature on microstructure and properties of thermal CVD TiN coatings. *Int. J. Refract. Met. Hard Mater.* **2008**, *26*, 120–126, doi:10.1016/j.ijrmhm.2007.01.010.

[6]   Rie, K.-T.; Wöhle, J. Plasma-CVD of TiCN and ZrCN films on light metals. *Surf. Coatings Technol.* **1999**, *112*, 226–229, doi:10.1016/S0257-8972(98)00803-2.

[7]   Rie, K.T.; Gebauer, A.; Wöhle, J. Plasma assisted CVD for low temperature coatings to improve the wear and corrosion resistance. *Surf. Coatings Technol.* **1996**, *86–87*, 498–506, doi:10.1016/S0257-8972(96)03177-5.

[8]   Haubner, R.; Rauchenwald, E.; Lessiak, M.; Pitonak, R.; Weissenbacher, R. Novel high-performance CVD coatings for machining applications. *Powder Metall. Prog.* **2018**, *18*, 128–138, doi:10.1515/pmp-2018-0015.

[9]   Huang, J.H.; Kuo, K.L.; Yu, G.P. Oxidation behavior and corrosion resistance of vacuum annealed ZrN-coated stainless steel. *Surf. Coatings Technol.* **2019**, *358*, 308–319, doi:10.1016/j.surfcoat.2018.11.054.

[10]   Garcia, J.; Moreno, M.F.; Östby, J.; Persson, J.; Pinto, H.C. Design of coated cemented carbides with improved comb crack resistance. *19th Plansee Semin. 2017* **2017**, 1–8.

[11]   Ul-Hamid, A. Microstructure, Properties and Applications of Zr-Carbide, Zr-Nitride and Zr-Carbonitride Coatings - A Review. *Mater. Adv.* **2020**, doi:10.1039/d0ma00233j.

[12]   El Azhari, I.; Garcia, J.; Zamanzade, M.; Soldera, F.; Pauly, C.; Llanes, L.; Mücklich, F. Investigations on micro-mechanical properties of polycrystalline Ti(C,N) and Zr(C,N) coatings. *Acta Mater.* **2018**, *149*, 364–376, doi:10.1016/j.actamat.2018.02.053.

[13]   El Azhari, I.; García, J.; Soldera, F.; Suarez, S.; Jiménez-Piqué, E.; Mücklich, F.; Llanes, L. Contact damage investigation of CVD carbonitride hard coatings deposited on cemented carbides. *Int. J. Refract. Met. Hard Mater.* **2020**, *86*, 105050, doi:10.1016/j.ijrmhm.2019.105050.

[14]   Russell, W.C. Experimental Design Approach to Development of a CVD ZrN Coating. *Le J. Phys. IV* **1995**, *5*, C5-127–134, doi:10.1051/jphyscol:1995513.

[15]   Long, Y.; Javed, A.; Chen, J.; Chen, Z.; Xiong, X. Phase composition, microstructure and mechanical properties of ZrC coatings produced by chemical vapor deposition. *Ceram. Int.* **2014**, *40*, 707–713, doi:10.1016/J.CERAMINT.2013.06.059.

[16]   Sundgren, J. -E.; Hentzell, H.T.G. A review of the present state of art in hard coatings grown from the vapor phase. *J. Vac. Sci. Technol. A Vacuum, Surfaces, Film.* **1986**, *4*, 2259–2279, doi:10.1116/1.574062.

[17]   El Azhari, I.; Barrirero, J.; García, J.; Soldera, F.; Llanes, L.; Mücklich, F. Atom Probe Tomography investigations on grain boundary segregation in polycrystalline Ti(C,N) and Zr(C,N) CVD coatings. *Scr. Mater.* **2019**, *162*, 335–340, doi:10.1016/j.scriptamat.2018.11.041.

[18] Kudapa, S.; Narasimhan, K.; Boppana, P.; Russell, W.C. Characterization and properties of MTCVD TiCN and MTCVD ZrCN coatings. *Surf. Coatings Technol.* **1999**, *120–121*, 259–264, doi:10.1016/S0257-8972(99)00484-3.

[19] Liu, Q.; Zhang, L.; Cheng, L.; Wang, Y. Morphologies and growth mechanisms of zirconium carbide films by chemical vapor deposition. *J. Coatings Technol. Res.* **2009**, *6*, 269–273, doi:10.1007/s11998-008-9117-5.

[20] Wang, Y.; Liu, Q.; Liu, J.; Zhang, L.; Cheng, L. Deposition mechanism for chemical vapor deposition of zirconium carbide coatings. *J. Am. Ceram. Soc.* **2008**, *91*, 1249–1252, doi:10.1111/j.1551-2916.2007.02253.x.

[21] Zhu, Y.; Cheng, L.; Ma, B.; Gao, S.; Feng, W.; Liu, Y.; Zhang, L. Calculation and synthesis of ZrC by CVD from $ZrCl_4$–C_3H_6–H_2–Ar system with high H_2 percentage. *Appl. Surf. Sci.* **2015**, *332*, 591–598, doi:10.1016/J.APSUSC.2015.01.175.

[22] Rauchenwald, E.; Lessiak, M.; Weissenbacher, R.; Haubner, R. Chemical vapor deposition of ZrN using in situ produced $ZrCl_4$ as a precursor. *Ceram. Int.* **2019**, *45*, 9410–9414, doi:10.1016/J.CERAMINT.2018.08.191.

[23] Kim, K.H.; Lee, S.H. Comparative studies of TiN and $Ti_{1-x}Al_xN$ by plasma-assisted chemical vapor deposition using a $TiCl_4$/$AlCl_3$/N_2/H_2/Ar gas mixture. *Thin Solid Films* **1996**, *283*, 165–170, doi:10.1016/0040-6090(96)08766-4.

[24] Kawata, K.; Sugimura, H.; Takai, O. Effects of chlorine on tribological properties of TiN films prepared by pulsed d.c. plasma-enhanced chemical vapor deposition. *Thin Solid Films* **2002**, *407*, 38–44, doi:10.1016/S0040-6090(02)00009-3.

[25] Rie, K.T.; Gebauer, A.; Woehle, J. Investigation of PA-CVD of TiN: Relations between process parameters, spectroscopic measurements and layer properties. *Surf. Coatings Technol.* **1993**, *60*, 385–388, doi:10.1016/0257-8972(93)90118-8.

[26] Anderbouhr, S.; Ghetta, V.; Blanquet, E.; Chabrol, C.; Schuster, F.; Bernard, C.; Madar, R. LPCVD and PACVD (Ti,Al)N films: Morphology and mechanical

properties. *Surf. Coatings Technol.* **1999**, *115*, 103–110, doi:10.1016/S0257-8972(99)00062-6.

[27] Stylianou, R.; Velic, D.; Daves, W.; Ecker, W.; Stark, A.; Schell, N.; Tkadletz, M.; Schalk, N.; Czettl, C.; Mitterer, C. Stress relaxation through thermal crack formation in CVD TiCN coatings grown on WC-Co with different Co contents. *Int. J. Refract. Met. Hard Mater.* **2020**, *86*, 105102, doi:10.1016/j.ijrmhm.2019.105102.

[28] Gassner, M.; Schalk, N.; Tkadletz, M.; Czettl, C.; Mitterer, C. Thermal crack network on CVD TiCN/α-Al$_2$O$_3$ coated cemented carbide cutting tools. *Int. J. Refract. Met. Hard Mater.* **2019**, *81*, 1–6, doi:10.1016/j.ijrmhm.2019.02.006.

[29] Bachmann, F.; Hielscher, R.; Schaeben, H. Texture analysis with MTEX - free and open source software toolbox. *Solid State Phenom.* **2010**, *160*, 63–68, doi:10.4028/www.scientific.net/SSP.160.63.

[30] Abadias, G.; Chason, E.; Keckes, J.; Sebastiani, M.; Thompson, G.B.; Barthel, E.; Doll, G.L.; Murray, C.E.; Stoessel, C.H.; Martinu, L. Review Article: Stress in thin films and coatings: Current status, challenges, and prospects. *J. Vac. Sci. Technol. A Vacuum, Surfaces, Film.* **2018**, *36*, 020801, doi:10.1116/1.5011790.

[31] Hill, R. The elastic behaviour of a crystalline aggregate. *Proc. Phys. Soc. Sect. A* **1952**, *65*, 349–354, doi:10.1088/0370-1298/65/5/307.

[32] Ivashchenko, V.I.; Turchi, P.E.A.; Shevchenko, V.I. First-principles study of elastic and stability properties of ZrC-ZrN and ZrC-TiC alloys. *J. Phys. Condens. Matter* **2009**, *21*, 395503, doi:10.1088/0953-8984/21/39/395503.

[33] Oliver, W.C.; Pharr, G.M. An improved technique for determining hardness and elastic modulus using load and displacement sensing indentation experiments. *J. Mater. Res.* **1992**, *7*, 1564–1583, doi:10.1557/JMR.1992.1564.

[34] Czettl, C.; Mitterer, C.; Mühle, U.; Rafaja, D.; Puchner, S.; Hutter, H.; Penoy, M.; Michotte, C.; Kathrein, M. CO addition in low-pressure chemical vapour deposition

of medium-temperature TiC_xN_{1-x} based hard coatings. *Surf. Coatings Technol.* **2011**, *206*, 1691–1697, doi:10.1016/j.surfcoat.2011.07.086.

[35]   Larsson, A.; Ruppi, S. Microstructure and properties of Ti(C,N) coatings produced by moderate temperature chemical vapour deposition. *Thin Solid Films* **2002**, *402*, 203–210, doi:10.1016/S0040-6090(01)01712-6.

[36]   Bonetti, R.S.; Wiprächtiger, H.; Mohn, E. CVD of titanium carbonitride at moderate temperature: Properties and applications. *Met. Powder Rep.* **1990**, *45*, 837–840, doi:10.1016/0026-0657(90)90575-2.

[37]   Sabitzer, C.; Steinkellner, C.; Koller, C.M.; Polcik, P.; Rachbauer, R.; Mayrhofer, P.H. Diffusion behavior of C, Cr, and Fe in arc evaporated TiN- and CrN-based coatings and their influence on thermal stability and hardness. *Surf. Coatings Technol.* **2015**, *275*, 185–192, doi:10.1016/j.surfcoat.2015.05.020.

[38]   Gates-Rector, S.; Blanton, T. The Powder Diffraction File: A quality materials characterization database. *Powder Diffr.* **2019**, *34*, 352–360, doi:10.1017/S0885715619000812.

[39]   Dreiling, I.; Haug, A.; Holzschuh, H.; Chassé, T. Raman spectroscopy as a tool to study cubic Ti-C-N CVD coatings. *Surf. Coatings Technol.* **2009**, *204*, 1008–1012, doi:10.1016/j.surfcoat.2009.05.029.

[40]   Pierson, H.O. *Handbook of chemical vapor deposition (CVD)*; 2nd ed.; Noyes Publications: Park Ridge, 1999; ISBN 0815514328.

[41]   Thompson, C. V Structure Evolution During Processing of Polycrystalline Films. *Annu. Rev. Mater. Sci.* **2000**, *30*, 159–190.

[42]   Park, J.H.; Jung, C.H.; Kim, D.J.; Park, J.Y. Effect of H_2 dilution gas on the growth of ZrC during low pressure chemical vapor deposition in the $ZrCl_4$-CH_4-Ar system. *Surf. Coatings Technol.* **2008**, *203*, 87–90, doi:10.1016/j.surfcoat.2008.08.004.

[43] Sun, W.; Xiong, X.; Huang, B.Y.; Li, G.D.; Zhang, H.B.; Xiao, P.; Chen, Z.K.; Zheng, X.L. Microstructural Control of Zirconium Carbide Coating Prepared by Chemical Vapor Deposition. *ECS Trans.* **2009**, *25*, 291–299.

[44] Wang, S.-L.; Li, K.-Z.; Li, H.-J.; Zhang, Y.-L.; Wang, Y.-J. Effects of microstructures on the ablation behaviors of ZrC deposited by CVD. *Surf. Coatings Technol.* **2014**, *240*, 450–455, doi:10.1016/J.SURFCOAT.2013.12.074.

[45] Imai, Y.; Mukaida, M.; Watanabe, A.; Tsunoda, T. Formation energies of two-dimensional nuclei randomly-generated on (001), (110), and (111) planes of a face-centered-cubic crystal. *Thin Solid Films* **1997**, *300*, 305–313, doi:10.1016/S0040-6090(96)09507-7.

[46] Stylianou, R.; Velic, D.; Daves, W.; Ecker, W.; Tkadletz, M.; Schalk, N.; Czettl, C.; Mitterer, C. Thermal crack formation in TiCN/α-Al$_2$O$_3$ bilayer coatings grown by thermal CVD on WC-Co substrates with varied Co content. *Surf. Coatings Technol.* **2020**, *392*, 125687, doi:10.1016/j.surfcoat.2020.125687.

[47] Pierson, H.O. *Handbook of Refractory Carbides and Nitrides: Properties, Characteristics, Processing and Applications*; 1st ed.; Noyes Publications: New York, 1996; ISBN 9780815513926.

[48] Gao, C.; Zhao, Z.; Li, X. Modeling of thermal stresses in elastic multilayer coating systems. *J. Appl. Phys.* **2015**, *117*, doi:10.1063/1.4907572.

[49] Pister, K.S. Flexural Vibration of Thin Laminated Plates. *J. Acoust. Soc. Am.* **1958**, *31*, 233–234.

[50] Reissner, E.; Stavsky, Y. Bending and Stretching of Certain Types of Heterogeneous Aeolotropic Elastic Plates. *J. Appl. Mech.* **1961**, *28*, 402–408.

[51] Chair of strucural and functional ceramics, Classical Laminate Theory (CLT) Available online: https://www.isfk.at/de/1428/ (accessed on Nov 2, 2020).

[52] Yang, Q.; Lengauer, W.; Koch, T.; Scheerer, M.; Smid, I. Hardness and elastic properties of Ti(C_xN_{1-x}), Zr(C_xN_{1-x}) and Hf(C_xN_{1-x}). *J. Alloys Compd.* **2000**, *309*, L5–L9, doi:10.1016/S0925-8388(00)01057-4.

[53] Jhi, S.H.; Ihm, J.; Loule, S.G.; Cohen, M.L. Electronic mechanism of hardness enhancement in transition-metal carbonitrides. *Nature* **1999**, *399*, 132–134, doi:10.1038/20148.

[54] Ivashchenko, V.I.; Turchi, P.E.A.; Gonis, A.; Ivashchenko, L.A.; Skrynskii, P.L. Electronic origin of elastic properties of titanium carbonitride alloys. *Metall. Mater. Trans. A Phys. Metall. Mater. Sci.* **2006**, *37*, 3391–3396, doi:10.1007/s11661-006-1031-9.

[55] Ková čik, J. Correlation between Young's modulus and porosity in porous materials. *J. Mater. Sci. Lett.* **1999**, *18*, 1007–1010, doi:10.1023/A:1006669914946.

[56]   Bouzakis, K.D.; Hadjiyiannis, S.; Skordaris, G.; Mirisidis, I.; Michailidis, N.; Efstathiou, K.; Pavlidou, E.; Erkens, G.; Cremer, R.; Rambadt, S.; et al. The effect of coating thickness, mechanical strength and hardness properties on the milling performance of PVD coated cemented carbides inserts. *Surf. Coatings Technol.* **2004**, *177–178*, 657–664, doi:10.1016/j.surfcoat.2003.08.003.

Publication II

In-situ investigation of the oxidation behaviour of chemical vapour deposited Zr(C,N) hard coatings using synchrotron X-ray diffraction

Florian Frank, Michael Tkadletz, Christian Saringer, Andreas Stark, Norbert Schell, Marco Deluca, Christoph Czettl, Nina Schalk

In-situ investigation of the oxidation behaviour of chemical vapour deposited Zr(C,N) hard coatings using synchrotron X-ray diffraction

Florian Frank[1], Michael Tkadletz[2], Christian Saringer[1], Andreas Stark[3], Norbert Schell[3], Marco Deluca[4], Christoph Czettl[5], Nina Schalk[1]

[1] Christian Doppler Laboratory for Advanced Coated Cutting Tools at the Department of Materials Science, Montanuniversität Leoben, Franz–Josef–Strasse 18, 8700 Leoben, Austria

[2] Department of Materials Science, Montanuniversität Leoben, Franz–Josef–Strasse 18, 8700 Leoben, Austria

[3] Institute of Materials Research, Helmholtz–Zentrum Geesthacht, Max–Planck–Strasse 1, 21502 Geesthacht, Germany

[4] Materials Center Leoben Forschung GmbH, Roseggerstrasse 12, 8700 Leoben, Austria

[5] Ceratizit Austria GmbH, Metallwerk–Plansee–Strasse 71, 6600 Reutte, Austria

Abstract

The oxidation behaviour of chemical vapour deposited ZrN, ZrC and ZrCN coatings was investigated using *in–situ* synchrotron X–ray diffraction (XRD). To obtain a precise analysis of the temperature–dependent phase evolution during oxidation, coating powders were annealed in air between 100 °C and 1000 °C. Simultaneously, 2D XRD patterns were recorded in ~2 °C increments, which were subsequently evaluated using parametric Rietveld refinement. The results were correlated with differential scanning calorimetry and thermogravimetric analysis measurements, to further illuminate the oxidation mechanism of each coating system. ZrCN exhibited the highest oxidation onset temperature, followed by ZrC and ZrN. Furthermore, ZrCN was completely oxidised at a temperature of ~720 °C, which was ~50–70 °C higher than for ZrN and ZrC. The *in–situ*

experiments revealed a similar oxidation sequence for all three samples: first, tetragonal and/or cubic (c/t)–ZrO_2 is formed, which subsequently transforms into the more stable monoclinic (m)–ZrO_2 phase. ZrCN and ZrC showed a higher c/t–ZrO_2 fraction than the ZrN sample at 1000 °C. Furthermore, *ex–situ* Raman and XRD investigations of the oxidised samples revealed the ongoing c/t–$ZrO_2 \rightarrow$ m–ZrO_2 phase transformation during cooling.

Keywords: CVD; Zr(C,N); in–situ synchrotron XRD; parametric Rietveld refinement; hard coatings

1. Introduction

Chemical vapour deposited (CVD) protective hard coatings are used in industrial turning and milling applications to improve the performance of cemented carbide cutting tools under extreme conditions. While CVD Ti(C,N) coatings have been intensively investigated and are widely applied [1–5], recent findings indicate advantageous mechanical properties of the CVD Zr(C,N) coating system [6–8]. Garcia et al. [6] and El Azhari et al. [7] reported an improved performance of Zr(C,N) under cyclic thermo–mechanical loads due to the better cohesive strength and intrinsic plasticity compared to Ti(C,N).

In addition to good mechanical properties, the oxidation resistance of hard coatings is crucial during machining applications. The oxidation stability of the Zr(C,N) system has been investigated by several authors [9–17]. Harrison and Lee [9] reported on the oxidation behaviour of commercially available ZrN powder (Sigma Aldrich), investigated in–situ between room temperature and 750 °C using a laboratory X–ray diffractometer (XRD). They observed the initial formation of substoichiometric ZrN_{1-x} and ZrO_xN_{1-x} at 400 °C, as well as the monoclinic ZrO_2 (m–ZrO_2) phase at 500 °C. Furthermore, sintered bulk ZrN was investigated ex–situ and a decreasing oxidation rate due to the

formation of a dense cubic ZrO_2 (c–ZrO_2) layer above 900 °C was observed. Small amounts of c–ZrO_2 and mainly m–ZrO_2 were also detected by Krusin–Elbaum and Wittmer in oxidised ZrN thin films, although already at lower temperatures of 475–650 °C compared to 900 °C for bulk materials [12]. Qi et al. [10] investigated the time dependent phase evolution of sputtered ZrN coatings at 650 °C with in–situ XRD and ex–situ TEM. After the initial formation of a tetragonal ZrO_2 (t–ZrO_2) layer on the coatings surface which proceeded to grow inwards, a martensitic phase transformation from t–ZrO_2 to m–ZrO_2 in the near surface region was observed. The occurrence of t–ZrO_2 was not expected at a temperature of 650 °C, as it is known to be less stable than m–ZrO_2 at temperatures below 1170 °C [18]. However, the authors attributed the formation of the t–ZrO_2 phase to the smaller activation energy needed for the phase transformation face centered cubic (fcc)–ZrN → t–ZrO_2 compared to ZrN → m–ZrO_2. The martensitic transformation from t–ZrO_2 to m–ZrO_2 is accompanied by a volume expansion of ~5 vol.-%, which leads to the formation of cracks and pores in the m–ZrO_2 layer of the oxide scale, which provide oxygen diffusion paths, further decreasing the oxidation resistance of the ZrN coating.

The oxidation behaviour of ZrC has been investigated in several studies on powder samples [13–15,19,20], as well as bulk materials [16,17,21–26] and CVD coatings [15]. The oxidation mechanism of this system is generally described by the initial formation of a ZrC_xO_y phase, followed by the occurrence of amorphous or nanocrystalline ZrO_2 [13–16,25–27]. This ZrO_2 phase acts as an oxygen diffusion barrier and retards the oxidation process, leading to the precipitation of free carbon. With increasing temperature, ZrO_2 crystallises to c–ZrO_2 or t–ZrO_2; it should be noted that the differentiation between t–ZrO_2 and c–ZrO_2 is not possible using XRD, as the reflections appear at very similar diffraction angles [26,28]. Analogously to t–ZrO_2, c–ZrO_2 is unstable at lower temperatures (<1170 °C), however, both phases can be stabilised by the substitution of O^{2-} with C^{3-} ions, creating oxygen ion vacancies [17,29]. As the temperature increases, CO_2 starts to form

and consequently the C content decreases, leading to the c/t–ZrO_2 → m–ZrO_2 phase transformation [14,17].

In comparison to ZrN and ZrC, where several studies on the oxidation resistance are available, literature on the oxidation behaviour of ZrCN as well as on the detailed oxidation mechanism of all three coating systems, deposited by CVD, is limited. Since the oxidation kinetics depend on the experimental conditions (e.g. oxygen partial pressure during oxidation), a comparison between these three systems based on previous reports is difficult. Thus, the goals of this study were on the one hand to provide a detailed investigation of the oxidation behaviour and phase evolution of CVD ZrCN and, on the other hand, to compare ZrCN to the more thoroughly investigated ZrN and ZrC by maintaining identical experimental conditions for the oxidation experiments. In order to establish a comprehensive understanding of the oxidation mechanism of CVD Zr(C,N) coatings, in–situ synchrotron X–ray powder diffraction experiments were conducted in ambient air. Subsequent parametric Rietveld refinement of the synchrotron data gave detailed insight into the temperature–dependent phase evolution. Complementary differential scanning calorimetry (DSC) and thermogravimetric analysis (TGA) were correlated with the results of the synchrotron experiments and provided additional insight in the oxidation behaviour. In order to investigate the phase change after the oxidation at 1000 °C, ex–situ Raman and XRD measurements were conducted.

2. Materials and Methods

2.1. Coating Deposition

The ZrN, ZrCN and ZrC coatings investigated in this work were deposited in an industrial scale hot–wall CVD reactor of the type Sucotec SCT600T. A solid Zr precursor was chlorinated beforehand, using a mixture of HCl and H_2. Subsequently, the resulting $ZrCl_4$ precursor was brought to reaction with H_2 and N_2 in the deposition chamber to synthesise ZrN. In order to deposit ZrCN or ZrC, the N_2 precursor was replaced by CH_3CN or CH_4, respectively. All coatings were deposited at a temperature of 1000 °C, a

base pressure of 10 kPa (ZrCN) and 16 kPa (ZrN and ZrC), and a constant deposition time of 260 min. To hinder interdiffusion between substrate and coating, a TiN base layer was grown on the substrate prior to the respective Zr(C,N) layers. The precursors used for the base layer were $TiCl_4$, N_2 and H_2 and the deposition temperature 1000 °C with a base pressure of 16 kPa. Cemented carbide with a composition of 92 wt.% WC, 6 wt.% Co and 2 wt.% mixed carbides, as well as mild steel foils were used as substrate materials. The mild steel foils were subsequently dissolved in diluted nitric acid and a powder of the coatings was produced.

2.2. *Coating Characterisation*

The microstructure of the solid coatings on cemented carbide was analysed at room temperature utilizing a Bruker D8 Advance X–ray diffractometer in grazing incidence geometry. A Göbel mirror was used to collimate the Cu Kα ($\lambda = 1.5418$ Å) radiation, which was directed at a 2° incidence angle at the sample. A secondary equatorial Soller collimator with a 0.12° acceptance angle was mounted in front of an energy dispersive Sol–X detector. Diffractograms were recorded with a step size of 0.02° and a counting time of 1.2 s per step. The in–situ synchrotron powder XRD investigations were carried out at the high energy materials science beamline P07 at PETRA III in Hamburg, Germany [30]. A schematic of the experimental setup is shown in Figure 1. The powdered Zr(C,N) coatings were placed in a heatable Pt crucible and heated in air with a heating rate of 10 K/min starting from 100 °C up to 1000 °C, utilizing inductive heating coils. Further details on the experiment can be found in ref. [31]. 2D X–ray diffractograms were recorded every ~2 °C at an exposure time of ~5 s in Debye–Scherrer geometry with a Perkin Elmer XRD 1621 flat–panel detector, resulting in ~600 frames per sample. The energy of the X–ray beam was 103.6 keV, which corresponds to a wavelength of 0.11965 Å.
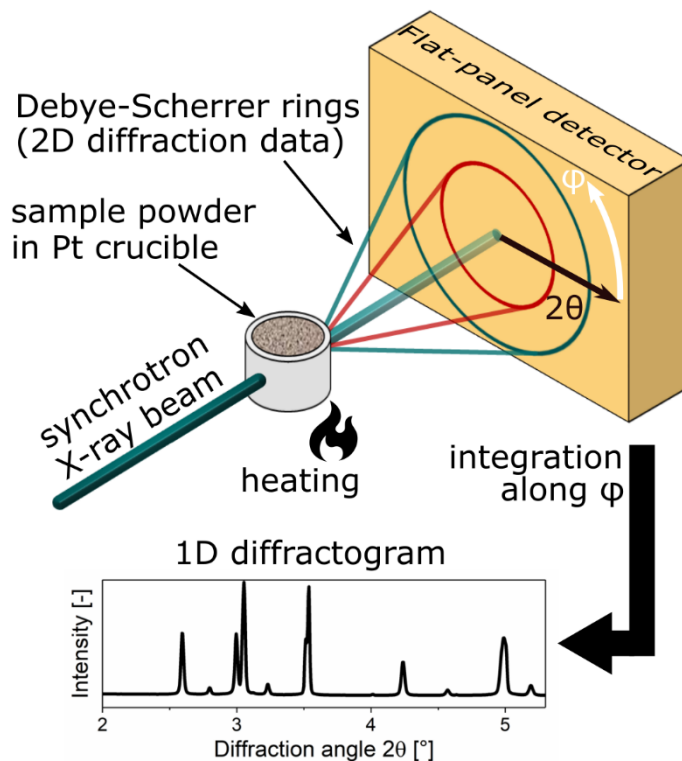
Figure 1. *Schematic view of the in-situ powder X-ray diffraction (XRD) experimental setup in Debye-Scherrer geometry at the synchrotron beam line. External heating was applied via inductive heating coils. By azimuthal integration (along φ) of the Debye-Scherrer rings (2D diffraction data), 1D diffractograms were obtained.*

DSC measurements were conducted in synthetic air using a Setaram Setsys Evo 2400 DSC. For the measurements ~20 mg of the powdered samples were filled into Al_2O_3 crucibles and heated with a heating rate of 10 K/min to 1000 °C. Raman spectroscopy measurements were performed in a LabRAM 300 spectrometer (Horiba Jobin Yvon, France) using 532 nm laser excitation. The powder samples were placed on a glass slide and analysed with a 100x long working distance objective with numerical aperture (NA) = 0.8 (Olympus, Japan). Raman spectra were collected in backscattering geometry using a through–focus configuration and dispersed by a 1800 gr/mm grating.

2.3. Synchrotron Data Evaluation — Parametric Rietveld Refinement

Further processing of the 2D diffraction data was conducted with a custom–made Python script, whereby the Debye–Scherrer rings of each individual frame were azimuthally integrated to obtain a respective 1D diffractogram, resulting in a temperature dependent set of diffraction data for each sample. The subsequent quantitative Rietveld refinement [32] was carried out using the software TOPAS 6, supplied by Bruker. In order to determine the instrumental contributions in the diffractograms, the diffraction pattern of a standard LaB_6 powder sample (NIST 660c [33]) was recorded and fitted using the Rietveld method. The so determined instrument function was used for the refinement of the diffraction data sets. A parametric Rietveld refinement approach (as described in ref. [34]) was applied to determine the quantitative phase evolution during oxidation of the Zr(C,N) samples. This approach was chosen since it can reduce the uncertainties of the output quantities (e.g. phase fractions) and helps to avoid false minima during the refinement of large sets of data including sporadic measurement artefacts. Furthermore, this method allows to provide a physical meaningful model to describe the evolution of cell–parameters with temperature, reducing the number of possible solutions, which can also decrease the uncertainty of the results [35]. Hereby, the model is applied to quantities of minor interest in order to gain more precise information about other quantities of interest. Within this oxidation study, a second–order polynomial function of the form

$$a(T) = a_0(1 + \lambda_1 T + \lambda_2 T^2) \tag{1}$$

where a_0 is the lattice parameter at room temperature and $\lambda_{1,2}$ are fit parameters, was used to describe the evolution of the lattice parameters a (quantities of minor interest) of each individual phase at the temperature T. This polynomial model guarantees smooth variations of the cell volume and the phase fractions (quantities of interest). Within this parametric refinement routine, all patterns are fitted simultaneously. A change of χ^2 of less than 0.001 between successive iteration steps was chosen as criterion of convergence and the quality of the refinement was assessed with the difference curve between the experimental and fitted pattern. The emerging phases were modelled using

crystallographic information files (cif), which were obtained from the Crystallography Open Database (COD) [36]. The applied non–oxide phases were ZrN [37], ZrCN [38], ZrC [39] and TiN [40]; the oxide phases were c–ZrO_2 [41], t–ZrO_2 [42], m–ZrO_2 [43] and rutile TiO_2 (r–TiO_2) [44].

3.   Results and discussion

3.1. As-deposited Microstructure

To validate that no significant changes in the phase composition occur during the powder preparation process, X–ray diffractograms of the as–deposited coatings on cemented carbide substrate were recorded on a laboratory XRD and compared to diffractograms of the powdered coatings, measured at the synchrotron radiation facility (see Figure 2). Both patterns were acquired at room temperature. Since the energies of the used X–ray sources were different, the diffractograms are plotted as a function of the d–spacing, enabling a straight forward comparison of the data. The standard peak positions of fcc–ZrN [45], fcc–ZrC [46] and fcc–TiN [47] are indicated as dashed lines and their individual hkl–indices are labelled. Peaks arising from the cemented carbide substrate (WC, solid coatings) and the Pt crucible (Pt, powdered coatings) are also marked. It can be seen that the positions of the diffraction peaks, arising from the face centered cubic (fcc) phases for the ZrN (Figure 2a), ZrCN (Figure 2b) and ZrC (Figure 2c) layer, as well as the TiN base layers, are comparable for the solid coating and the powder, indicating that no significant changes in chemistry occur during the powdering process. Rietveld refinement of the powdered samples revealed stress free lattice parameters of 4.58 ± 0.01 Å and 4.71 ± 0.01 Å for ZrN and ZrC, respectively. These results agree well with the lattice parameters of 4.58 Å and 4.69 Å given by the ICDD cards for stoichiometric ZrN and ZrC, respectively [45,46]. ZrCN forms a solid solution and the lattice parameter was determined to be 4.63 ± 0.01 Å, which results in a composition of $ZrC_{0.4}N_{0.6}$, assuming a Vegard's like behaviour. A change in the relative peak intensities, arising from different hkl–planes, between solid and powdered coatings is related to a

loss of preferred orientation during powdering. This is best observed for the ZrCN solid coating (Figure 2b). The 200 peak shows the highest intensity, whereas in the powdered sample the 111 peak is higher than the 200, as would be expected for an untextured sample.
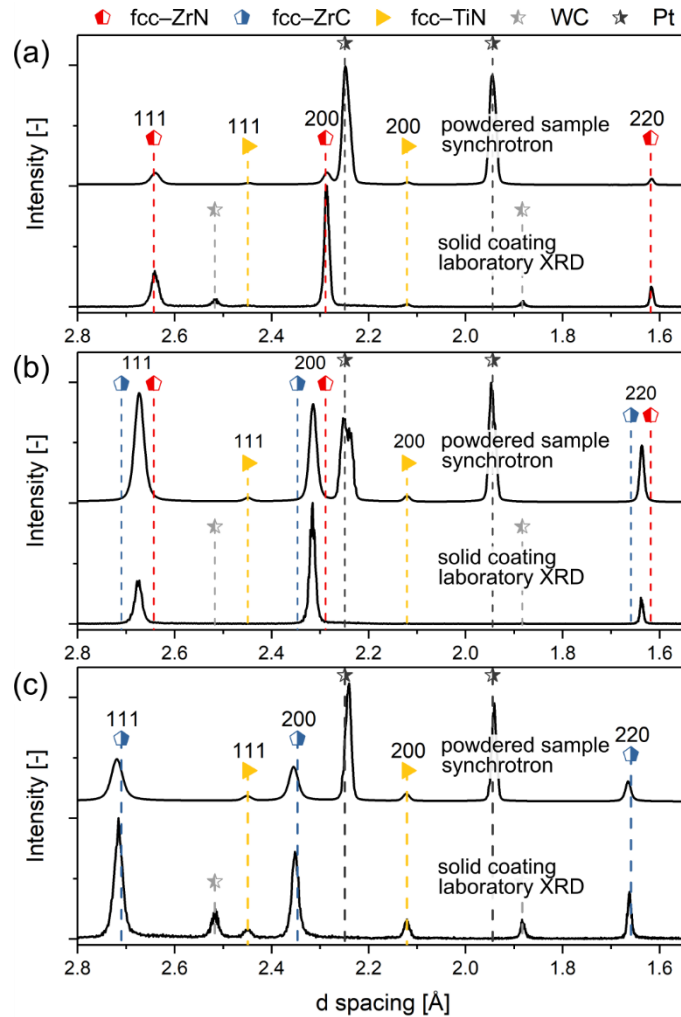
Figure 2. *Comparison of the X-ray diffractograms of the solid coatings (laboratory XRD in grazing incidence geometry with 2° incidence angle) and the powdered coatings (synchrotron radiation facility, Debye-Scherrer geometry) for the (a) ZrN, (b) ZrCN, (c) ZrC samples. The patterns were recorded at room temperature.*

3.2. Oxidation Behaviour

The temperature dependent phase evolution during oxidation is displayed in Figure 3 in 2D contour plots, commonly referred to as phase plots, from 100 °C to 1000 °C

for ZrN (Figure 3a), ZrCN (Figure 3b) and ZrC (Figure 3c). Especially for the diffractograms of the powdered ZrN sample at room temperature, it becomes apparent that the peak contributions from the Pt crucible are high compared to the ZrN peaks (see Figure 2a). Thus, the contributions of the Pt crucible were fitted using the Pawley method [48] and subsequently subtracted from the fitted patterns to enhance the visibility of the phase evolution. These modelled fits without the signal from the Pt crucible are displayed in Figure 3. Diffraction peaks arising from the non–oxidised phases (ZrN, ZrCN, ZrC, TiN) are indicated by symbols and dashed lines at the bottom of each phase plot, respectively. Since a clear differentiation between the c–ZrO_2 and t–ZrO_2 phase is not possible for XRD experiments, the peaks are indicated with one symbol and dashed line at the top of each phase plot, alongside the m–ZrO_2 and r–TiO_2 phases. In the following, if no separation between the c–ZrO_2 and t–ZrO_2 can be made, the phase will be referred to as c/t–ZrO_2. In all three phase plots a slight shift towards lower diffraction angles can be observed for the ZrN, ZrCN and ZrC phases with increasing temperature, which is related to an increase of the lattice parameter due to thermal expansion. In addition, all three phase plots can be divided into three temperature zones, which are separated by white dashed lines. In Zone 1 of the phase plots, only the fcc–Zr(C,N) phases and the fcc–TiN peaks from the substrate are visible. The oxidation onset marks the beginning of Zone 2, which occurs at ~400 °C for ZrN, followed by ZrC at ~530 °C and ZrCN, which exhibits the highest onset temperature of ~570 °C. For all three samples, the oxidation starts with the emergence of a c/t–ZrO_2 phase, followed by the formation of m–ZrO_2. Although m–ZrO_2 is the stable phase at temperatures below 1170 °C, this phase evolution can be explained by a lower activation energy of Zr(C,N) $\rightarrow$ c/t–ZrO_2 compared to Zr(C,N) $\rightarrow$ m–ZrO_2 [10,18]. The c/t–ZrO_2 phase then undergoes a martensitic phase transformation to m–ZrO_2, which is accompanied by a volume expansion of ~5% [18,29]. This phase evolution was reported by several authors for the ZrN [10,11,28], as well as for the ZrC system [14,15,21]. However, as it can be seen for all three samples in Figure 3, the c/t–ZrO_2

phase prevails in Zone 2 and Zone 3 up to 1000 °C and is not completely transformed to m–ZrO_2. This characteristic is attributed to the fact that the c/t–ZrO_2 can be stabilised at lower temperatures by a number of different mechanisms, which were discussed in detail by Shukla and Seal [29]. Generally, a decrease of the particle size to the nm range enables the stabilisation of the c/t–ZrO_2 phase. For a free–standing single–crystalline particle, the critical size at room temperature above which only m–ZrO_2 is formed is in the range of ~10 nm, due to the stabilisation of the c/t–ZrO_2 phase by the increased specific surface area at lower particle sizes. However, powdered coatings are more properly represented as an agglomeration of crystallites for which a larger critical grain size of ~33 nm at room temperature is observed [29,49]. This can be explained by two factors. First, in an agglomeration the surface is replaced by an interface with other crystallites which changes the energy state. This energy state is related to the interface free energy and the volume free energy of the crystallite. The contribution of the interfacial free energy increases with decreasing grain size. Due to the fact that the interfacial free energy is lower for the c/t–ZrO_2 than the m–ZrO_2 phase, the c/t–ZrO_2 phase is stabilised below a critical grain size of 33 nm at room temperature [29,49]. Second, hydrostatic stress which can build up in an agglomeration may lead to an increase in the critical grain size. The formation of m–ZrO_2 is associated with a volume expansion of ~5%. Thus, already transformed crystallites induce compressive stress in the untransformed c/t–ZrO_2 crystallites, consequently stabilizing their crystal structure at larger grain size [29,50]. Additionally, the critical grain size for the c/t–ZrO_2 phase stabilisation depends on the temperature. Using eq. 17 from ref. [29], a critical grain size of ~230 nm at 1000 °C can be calculated. A "double–Voigt" approach was applied to estimate the size of coherently diffracting domains, which is assumed to be in the range of the average grain size, of the present c/t–ZrO_2 phases for selected patterns in Zone 2 and in Zone 3 (>950 °C). The results were similar for the ZrN, ZrCN and ZrC samples and displayed an average domain size for their corresponding c/t–ZrO_2 phases of 8–11 nm in Zone 2 and 16–20 nm in Zone 3.

Although these values for the domain size are only rough estimations and should be treated carefully, it can be assumed that the average grain size is sufficiently small (<33 nm) to allow for a c/t–ZrO$_2$ phase stabilisation.
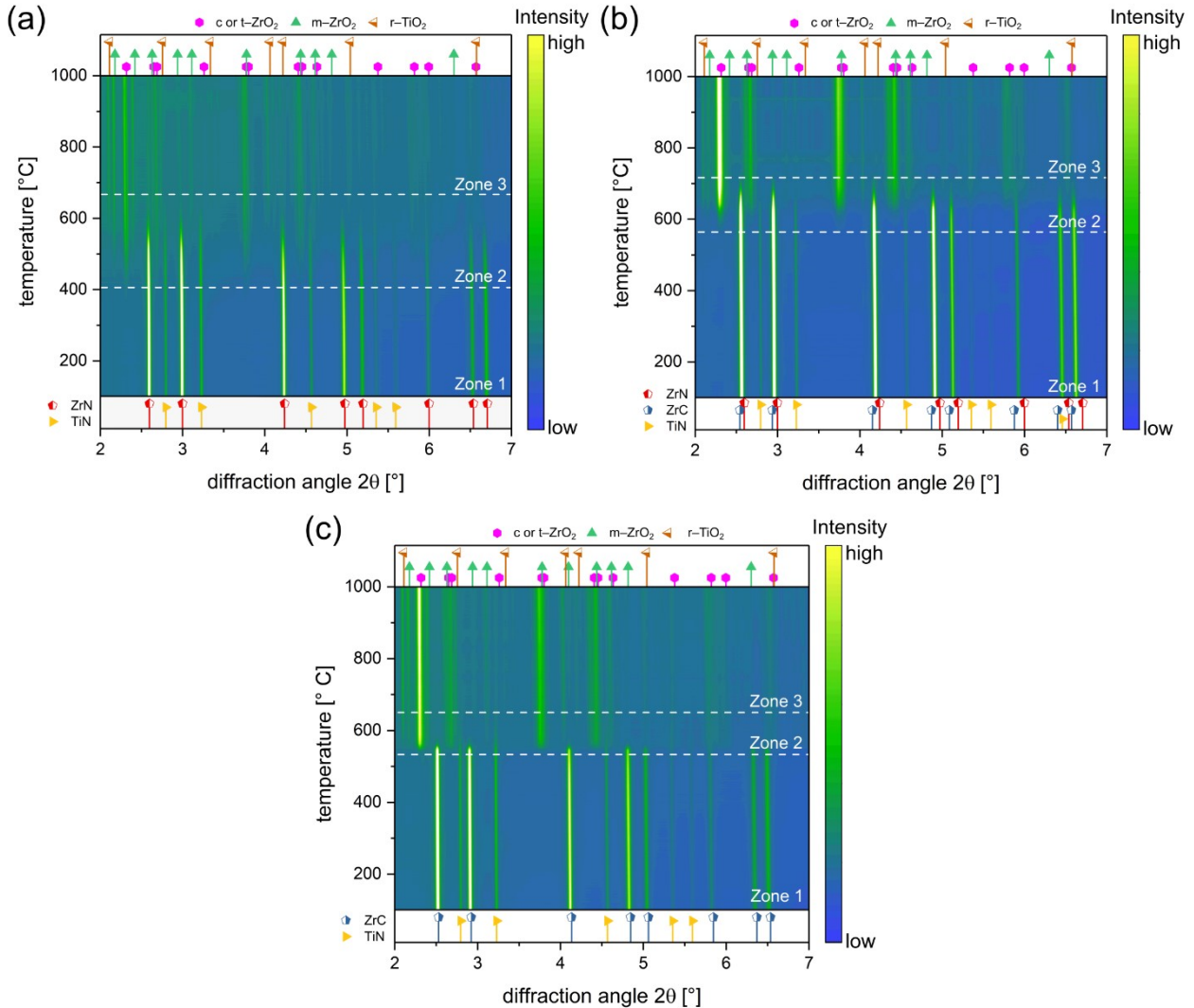

Figure 3. Phase plots of the modelled in-situ powder XRD data as a function of the oxidation temperature for the (a) ZrN, (b) ZrCN and (c) ZrC sample. The intensity of the diffraction data is colour coded.

In addition to the ZrO$_2$ phases, also the initial formation of r–TiO$_2$ from the TiN base layer is visible at ~655 °C in the phase plots in Zone 2. This r–TiO$_2$ phase is stable up to 1000 °C. Full oxidation for all samples is obtained at ~650 °C for ZrC, followed by ZrN at ~670 °C and ZrCN at ~720 °C, which is indicated by the dashed line at the beginning of

Zone 3. In Figure 3a,b it can be seen that the corresponding TiN phases are not as stable as the ZrN and ZrCN phases, as they vanish at ~650 °C. The TiN phase in Figure 3c also vanishes at ~650 °C, however, the ZrC phase is even less stable and disappears already at ~580 °C. This small temperature range for the oxidation of the ZrC phase of only 50 °C after the initial c/t–ZrO_2 formation demonstrates the high rate at which the oxidation of ZrC takes place, in contrast to ZrN, where the oxidation proceeds over a temperature range of ~270 °C. No sudden peak shift of the ZrN, ZrCN and ZrC phases towards higher 2θ angles could be observed with increasing temperature, which would indicate the presence of a substoichiometric ZrN_x, ZrC_xN_y or ZrC_x phase due to a possible loss of N or C. The formation of ZrN_x, was observed by Harrison and Lee above 400 °C for the oxidation of ZrN powder using *in–situ* laboratory XRD in static air [9]. Besides the formation of substoichiometric phases, the occurrence of oxynitride ($ZrO_{1-x}N_x$) or oxycarbide ($ZrO_{1-x}C_x$) phases seems plausible and is suggested by some authors, yet, they are rarely experimentally confirmed [9,23]. This circumstance can be explained by their ambiguity with other phases (ZrN, ZrC) or their low present fraction. The occurrence of these phases might be related to a low supply of oxygen, given by the experimental conditions [9,13,14,16,17,25,26,51,52]. For the synchrotron measurements in this work a sufficiently high supply of oxygen to form ZrO_2 rather than substoichiometric compounds was guaranteed, as the crucible was completely exposed to ambient air.

By fitting the *in-situ* synchrotron data using a parametric Rietveld refinement routine, the phase evolution during the oxidation process can be quantitatively evaluated, which is shown in the following section. A representative example of a refined pattern along with the individual phase contributions is presented in Figure 4. The ZrN sample at a temperature of 577 °C (Zone 2) was chosen as it displays both, nitride and oxide phases in one pattern, since the oxidation is not yet finished at this temperature. The difference curve (grey line) between the measured and fitted pattern is displayed at the bottom and its appearance was used as an indication of a reasonable fit. While the ZrN,

TiN, m–ZrO_2 and r–TiO_2 phases can be clearly distinguished, an overlap of the t–ZrO_2 and c–ZrO_2 phase is visible. Even though both phases were fitted individually, their resulting weight percentage is presented as sum of both phases in the following section, because of the ambiguity in the differentiation of both phases.
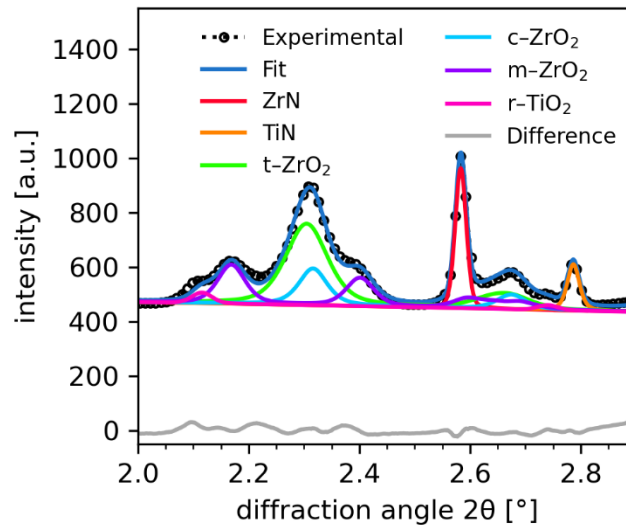

Figure 4. Rietveld refinement of the ZrN sample at 577 °C. The fits of the nitride and oxide phases, as well as the measured pattern, the fit and the difference curve between the measured pattern and the fit are displayed in different colours.

The temperature dependent quantitative phase evolution of the three samples is displayed in Figure 5a (ZrN), Figure 5b (ZrCN) and Figure 5c (ZrC). The error for the phase fractions was <1 wt.% for all phases and temperatures. To facilitate the comparison of the phase evolution of the three samples, the onset and end temperatures of the oxidation are highlighted in Figure 5d. The individual zones are also indicated by dashed lines within Figure 5a–c, corresponding to the zones discussed in Figure 3. In Zone 1, the phase content of the TiN from the base layer is similar for the ZrN (~25 wt.%) and ZrC (~26 wt.%) sample, but lower for the ZrCN (~11 wt.%) sample. This content variation can be related to a difference in the thickness ratio of the Zr(C,N) layers to the TiN, which was evaluated from SEM cross section images (not shown). The ZrCN layer was thicker (~3.5 µm) compared to ZrN (~0.9 µm) and ZrC (~0.9 µm), while the TiN base layer

thickness was comparable for all three coatings (~0.5 μm for ZrN, ~0.8 μm for ZrCN and ~0.7 μm for ZrC). The difference in coating thickness is related to the higher reactivity of ZrCN during the deposition process compared to the pure ZrN and ZrC which leads to an overall higher Zr(C,N) phase fraction in the ZrCN sample. For the initial formation of oxide phases, marked with the border to Zone 2, a threshold of >1 wt.% was chosen as the criterion for the onset temperatures. The ZrN sample (Figure 5a) shows a continuous decline of the ZrN phase in Zone 2, with the initial formation of the c/t–ZrO_2 phase at ~400 °C. With a slight delay, the m–ZrO_2 phase starts to form at ~460 °C and up to ~600 °C the slopes of c/t–ZrO_2 and m–ZrO_2 are almost equal, indicating that the simultaneous formation of c/t–ZrO_2 and successive martensitic phase transformation to the more stable m–ZrO_2 phase occur at approximately equal rates. The oxidation of the ZrCN sample (Figure 5b) begins similarly to the ZrN sample with the formation of c/t–ZrO_2, but at a different temperature of ~560 °C. However, here the oxidation occurs with a higher rate compared to ZrN. Furthermore, the martensitic phase transformation to m–ZrO_2 occurs at a slower rate compared to ZrN, resulting in a maximum phase fraction of only <6 wt.% m–ZrO_2 at the end of Zone 2 for ZrCN compared to ~28 wt.% m–ZrO_2 for ZrN. An even higher formation rate is observed for the ZrC → c/t–ZrO_2 phase transition in Zone 2 of Figure 5c. Within 50 °C, starting with the formation of c/t–ZrO_2 at ~530 °C and ending with the disappearance of ZrC at ~580 °C, the ZrC phase is completely oxidised and mainly c/t–ZrO_2 is formed (72 wt.% at 580 °C) with minor contributions of 6 wt.% m–ZrO_2. At the end of Zone 3 of the ZrN sample, the content of m–ZrO_2 is higher (36 wt.%) than the c/t–ZrO_2 content (29 wt.%). In contrast to the ZrN sample, the major oxide modification of the oxidised ZrCN and ZrC samples is c/t–ZrO_2. ZrCN exhibited 80 wt.% c/t–ZrO_2 and 8 wt.% m–ZrO_2 at 1000 °C and ZrC contained 60 wt.% c/t–ZrO_2 and 16 wt.% m–ZrO_2 at the same temperature. The higher c/t–ZrO_2 phase fraction in the C containing samples might be related to small amounts of residual amorphous C, stabilising the c/t–ZrO_2 phase and thus inhibiting the formation of m–ZrO_2 [13,14,17,26]. This c/t–ZrO_2 phase

stabilisation is expected to be beneficial in solid coatings, as the c/t–ZrO_2 → m–ZrO_2 martensitic phase transformation is accompanied by a ~5% volume increase in the oxide scale resulting in the formation of microcracks. These cracks provide oxygen diffusion paths through the oxide scale towards the still intact Zr(C,N) regions, thus reducing the coatings oxidation resistance [10,53].

TiN starts to oxidise at ~540–550 °C in the ZrN and ZrC sample and at ~595 °C in the ZrCN sample, as highlighted by the onset of r–TiO_2 formation in Figure 5d. This is in good agreement with literature, where the oxidation onset temperature for TiN is reported to lie between 550 °C and 600 °C [54-56]. Since the TiN base layers were synthesised under the same deposition conditions, it is expected that the onset temperature is equal for all three sample. The observed deviation of the TiN oxidation onset in the ZrCN sample compared to the ZrN and ZrC sample is related to the lower relative phase fraction of TiN powder in the ZrCN sample, as the intensity of the diffraction peaks and thus the evaluated wt.% is influenced by the amount of TiN powder present in the sample. A sensible Rietveld refinement relies on the intensity of the diffraction peak and thus the low amounts of r–TiO_2 might not be fitted reasonably, shifting the onset of oxidation to higher temperatures. If the onset of oxidation for TiN is considered to lie between 540–550 °C for all samples, ZrCN shows a slightly higher oxidation onset temperature with ~570 °C compared to TiN, while ZrN and ZrC have a lower onset temperature of ~400 °C and ~530 °C, respectively.
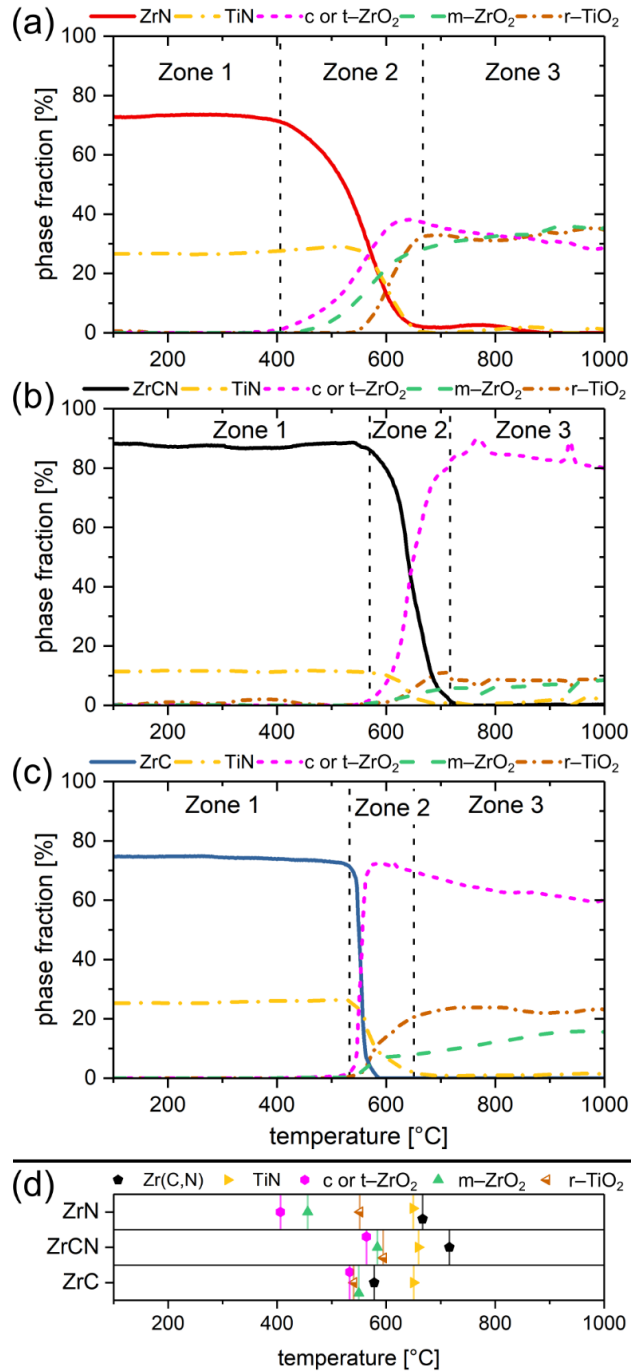
Figure 5. *Quantitative phase evolution as a function of the oxidation temperature for (**a**) ZrN, (**b**) ZrCN and (**c**) ZrC, obtained by parametric Rietveld refinement. (**d**) The oxidation onset temperatures of the oxide phases (c or t-ZrO$_2$, m-ZrO$_2$ and r-TiO$_2$), as well as the temperature of full oxidation of the Zr(C,N) and TiN phases for the ZrN, ZrCN and ZrC sample, respectively.*

3.4. Influence of Carbon on the Oxidation Onset Temperature

DSC and TGA investigations are shown in Figure 6a,b, respectively. The oxidation onset temperatures, determined by the synchrotron measurements and parametric Rietveld refinement, are indicated by the arrows in colours corresponding to the respective Zr(C,N) samples. As an exothermic change in the heat flow and a mass gain indicate the beginning of the oxidation process, the ZrN, ZrCN and ZrC oxidation onset temperature matches quite well with the onset determined by the *in-situ* synchrotron experiments. The minor changes in the heat flow of the ZrCN and ZrC sample at temperatures below the oxidation onset observed in the synchrotron measurements might be due to the formation of amorphous phases. One has to keep in mind that the results of the synchrotron measurements are based on the evolution of crystalline phases and that amorphous ZrO_2 and free C might be formed at lower temperatures, as observed by several authors [13–16,25–27]. At these lower temperatures, the provided oxygen is mainly used for the formation of amorphous ZrO_2 rather than CO_2, since the combustion of C is expected to take place at temperatures >600 °C [13,14,19,25]. As the temperature increases, the amorphous ZrO_2 forms c/t–ZrO_2 which was detected in the *in-situ* synchrotron experiments (see Figure 4b,c). The DSC signal of the ZrC sample shows a broad peak at ~600 °C to 630 °C. This broad peak can be attributed to two consecutive reactions that take place during the ZrC oxidation at slightly different temperatures. The first reaction at ~600 °C can be related to the oxidation of ZrC and the reaction at ~620 °C arises due to the combustion of the retained C, which was also observed in ref. [19]. Compared to ZrC, no distinct DSC peak related to the formation of CO_2 is observable in the ZrCN sample. This can be explained by the higher oxidation temperature (>600 °C) for the ZrCN sample, allowing for the subsequent formation of CO_2 from the newly formed C. Additionally, less C will be formed at temperatures <600 °C due to the higher oxidation onset and the lower C content of ZrCN compared to ZrC. The maximum of the exothermic peaks in the heat flow signal are observed at ~650 °C, ~710 °C and ~600 °C for

ZrN, ZrCN and ZrC, respectively. This is in excellent agreement with the maximum content of the c/t–ZrO$_2$ phase observed in the phase evolution and the end of the oxidation process (Figure 5), where the transformation rate is the highest. In the heat flow signal of the ZrN sample, a shoulder at ~700 °C superimposes the oxidation peak. This shoulder might be related to r–TiO$_2$ formation from the TiN base layer, as the r–TiO$_2$ content also shows a maximum in the phase evolution at ~700 °C. The heat flow signal of the ZrC sample also exhibits a minor peak at ~700 °C. As the ZrC oxidation process is already finished at this temperature, this observation further corroborates the assumption that this peak is indeed related to the base layer oxidation. In the ZrCN the contributions of the TiN base layer to the DSC and TGA signal seem to be superimposed by the ZrCN oxidation possibly explaining the asymmetric ZrCN peak.
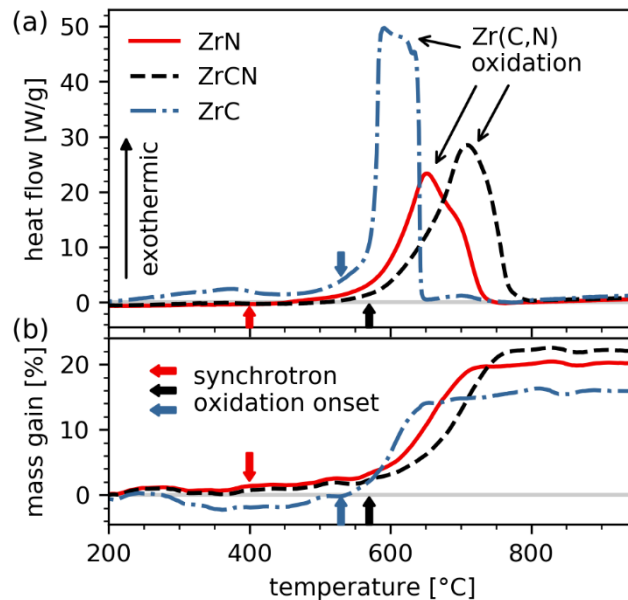

Figure 6. *(**a**) Heat flow of the Zr(C,N) samples and (**b**) mass gain from the thermogravimetric analysis as a function of the oxidation temperature. The arrows indicate the oxidation onset temperatures as determined by the in-situ synchrotron powder diffraction experiments.*

The final phase composition after cooling down from the oxidation process was investigated *ex–situ* with Raman spectroscopy and XRD. The characteristic Raman bands of m–ZrO$_2$ and t–ZrO$_2$ [57–59], as well as r–TiO$_2$ [60] are indicated as dashed lines in

Figure 7a and the diffraction peaks of m–ZrO_2 [61], c/t–ZrO_2 [62,63] and r–TiO_2 [64] are highlighted in Figure 7b. The Raman spectra and XRD patterns are in good agreement. Both, the oxidised ZrN and ZrCN samples exhibit mainly the m–ZrO_2 phase with minor traces of t–ZrO_2, whereas the ZrC sample shows a higher t–ZrO_2 contribution in the Raman spectrum and higher c/t–ZrO_2 in the XRD. While the r–TiO_2 peaks, arising from the oxidation of the TiN base layer, exhibit a low intensity and can be clearly distinguished from the ZrO_2 peaks in the XRD, the r–TiO_2 bands in the Raman spectra show a high intensity, partially superimposing the ZrO_2 bands. Especially the F_{2g}–mode at ~600 cm^{-1} of c–ZrO_2 is superimposed by the A_{1g} contribution of r–TiO_2 at ~610 cm^{-1} [58,65]. Due to this overlap and the high intensity of r–TiO_2, an unambiguous identification of the c–ZrO_2 phase in the Raman spectra is not possible. Thus, a clear distinction between the c–ZrO_2 and t–ZrO_2 phase was also not possible with Raman spectroscopy. In order to investigate the effect of cooling the samples from the final oxidation temperature of 1000 °C to room temperature on the phase composition, a quantitative Rietveld refinement of the *ex–situ* XRD data was performed. The results are compared to those of the Rietveld refinement of the *in–situ* measurement at 1000 °C in Figure 7c. All three samples show an increase of the m–ZrO_2 phase and a decrease of t–ZrO_2 after cooling, as would be expected from the ongoing martensitic phase transformation during the cooling process. While ZrCN shows the largest increase of m–ZrO_2 during cooling, the smallest increase is observed for ZrN, which is related to the already high m–ZrO_2 fraction in ZrN at 1000 °C compared to ZrCN. ZrC exhibits a moderate m–ZrO_2 increase, with a slightly lower m–ZrO_2 phase fraction at room temperature compared to the ZrCN sample. This might indicate a higher c/t–ZrO_2 phase stabilisation in ZrC compared to ZrCN and ZrN. One possible explanation could be that the c/t–ZrO_2 grain size might be smaller in the ZrC sample compared to ZrCN and ZrN, which would lead to a c/t–ZrO_2 phase stabilisation [29,49]. Another reason for the stabilisation might be related to a higher amount of residual C in the ZrC sample compared to ZrCN and ZrN, which would also result in a c/t–ZrO_2 phase stabilisation.

The Raman measurements suggest a higher contribution of the G–band, which is related to the sp^2 (graphitelike) bonds of C [66], in the ZrC sample compared to ZrN and ZrCN. However, these C contributions in the Raman spectrum are small and superimposed by a fluorescent background and are therefore not shown in Figure 7a. Most probably a combination of these stabilisation effects occurs in the ZrC sample, which cannot be clearly differentiated.
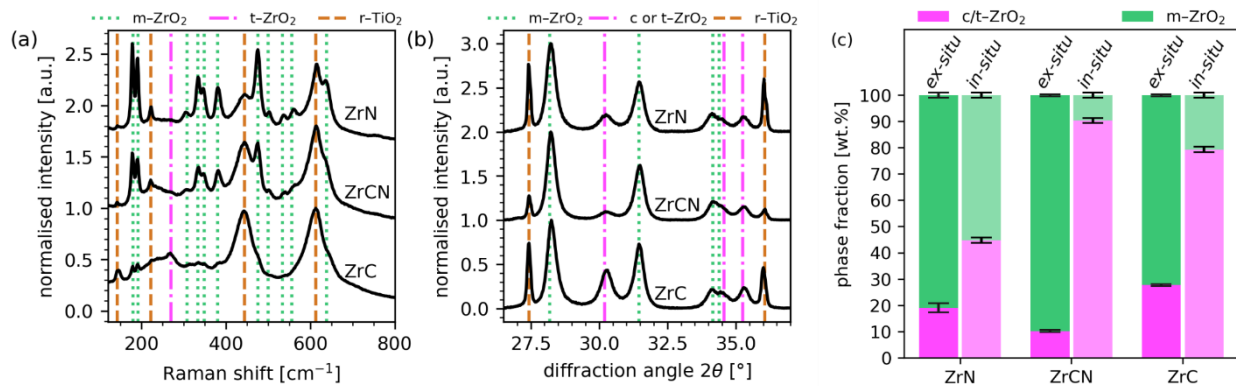
Figure 7. (**a**) *Ex-situ Raman spectra and* (**b**) *ex-situ X-ray diffractograms of the ZrN, ZrCN and ZrC powdered samples oxidised at 1000 °C.* (**c**) *Phase fraction of the ZrN, ZrCN and ZrC samples oxidised at 1000 °C, measured ex-situ using a laboratory XRD at room temperature and in-situ at the synchrotron facility at 1000 °C.*

3. Conclusions

Within this work, the oxidation behaviour of powdered ZrN, ZrCN and ZrC coatings, grown by chemical vapour deposition, was investigated. *In–situ* synchrotron X–ray diffraction (XRD) and successive evaluation of the obtained diffraction data by parametric Rietveld refinement gave insight into the phase evolution during oxidation between 100 °C and 1000 °C. For the parametric refinement, a polynomial model was used to describe the thermal expansion of the unit cells of the individual phases with increasing temperature. Differential scanning calorimetry (DSC) and thermogravimetric analysis (TGA) were correlated with the results of the synchrotron experiments. *Ex–situ* Raman spectroscopy and laboratory X–ray diffraction complemented the *in–situ* investigations

and displayed a change in the phase composition after the cooling process. ZrCN exhibited the highest oxidation onset temperature at ~570 °C, followed by ZrC with ~530 °C and ZrN, which showed the lowest oxidation onset at ~400 °C. Furthermore, the ZrCN coating was only completely oxidised at a temperature of ~720 °C, resulting in a better oxidation resistance compared to the ZrN and ZrC coating, which were already entirely oxidised at ~670 °C and ~650 °C, respectively. Parametric Rietveld refinement revealed a similar oxidation mechanism for all three coating systems: after the loss of N or C from the Zr(C,N) lattice and the uptake of O, cubic and/or tetragonal c/t–ZrO_2 phases are formed initially. c/t–ZrO_2 then transformed to the monoclinic m–ZrO_2 phase, which is usually more stable at the investigated temperatures. ZrCN and ZrC showed the highest c/t–ZrO_2 phase fractions, indicating that these phases were stabilised in these samples. This stabilisation effect might be related to residual C and/or a smaller grain size in the ZrCN and ZrC samples. In order to assess phase changes during cooling from 1000 °C to room temperature, previously oxidised samples were studied *ex–situ* by Raman spectroscopy and XRD, which revealed a major increase of the m–ZrO_2 phase compared to the *in–situ* synchrotron measurement at 1000 °C for all three samples, indicating an ongoing martensitic phase transformation during cooling. Summarizing, the present work gives insight into the phase evolution during oxidation of ZrN, ZrCN and ZrC coatings, highlighting the higher oxidation resistance of the lesser investigated ZrCN compared to ZrN and ZrC.

4.   Acknowledgments

5.   References

[1]   Sundgren, J.E. Structure and properties of TiN coatings. *Thin Solid Films* **1985**, *128*, 21–44, doi:10.1016/0040-6090(85)90333-5.

[2]   Rebenne, H.E.; Bhat, D.G. Review of CVD TiN coatings for wear-resistant applications: deposition processes, properties and performance. *Surf. Coatings Technol.* **1994**, *63*, 1–13, doi:10.1016/S0257-8972(05)80002-7.

[3]   Holzschuh, H. Deposition of Ti–B–N (single and multilayer) and Zr–B–N coatings by chemical vapor deposition techniques on cutting tools. *Thin Solid Films* **2004**, *469–470*, 92–98, doi:10.1016/J.TSF.2004.08.077.

[4]   Wagner, J.; Mitterer, C.; Penoy, M.; Michotte, C.; Wallgram, W.; Kathrein, M. The effect of deposition temperature on microstructure and properties of thermal CVD TiN coatings. *Int. J. Refract. Met. Hard Mater.* **2008**, *26*, 120–126, doi:10.1016/j.ijrmhm.2007.01.010.

[5]   Kainz, C.; Schalk, N.; Tkadletz, M.; Winkler, M.; Czettl, C. Microstructure, mechanical and thermo-physical properties of CVD TiC_xN_{1-x} coatings on cemented carbide substrates grown with C_2H_6 as C feeding precursor. *Surf. Coat. Technol.* **2020**, doi:10.1016/j.metabol.2020.154244.

[6]   Garcia, J.; Moreno, M.F.; Östby, J.; Persson, J.; Pinto, H.C. Design of coated
        cemented carbides with improved comb crack resistance. *19th Plansee Semin. 2017*
        2017, 1–8.

[7]   El Azhari, I.; Garcia, J.; Zamanzade, M.; Soldera, F.; Pauly, C.; Llanes, L.; Mücklich,
        F. Investigations on micro-mechanical properties of polycrystalline Ti(C,N) and
        Zr(C,N) coatings. *Acta Mater.* **2018**, *149*, 364–376, doi:10.1016/j.actamat.2018.02.053.

[8]   El Azhari, I.; Barrirero, J.; García, J.; Soldera, F.; Llanes, L.; Mücklich, F. Atom Probe
        Tomography investigations on grain boundary segregation in polycrystalline
        Ti(C,N) and Zr(C,N) CVD coatings. *Scr. Mater.* **2019**, *162*, 335–340,
        doi:10.1016/j.scriptamat.2018.11.041.

[9]   Harrison, R.W.; Lee, W.E. Mechanism and Kinetics of Oxidation of ZrN Ceramics.
        J. Am. Ceram. Soc. **2015**, *98*, 2205–2213, doi:10.1111/jace.13575.

[10]   Qi, Z.B.; Wu, Z.T.; Liang, H.F.; Zhang, D.F.; Wang, J.H.; Wang, Z.C. In situ and ex
        situ studies of microstructure evolution during high-temperature oxidation of ZrN
        hard coating. *Scr. Mater.* **2015**, *97*, 9–12, doi:10.1016/J.SCRIPTAMAT.2014.10.024.

[11]   Gao, Z.; Chen, Y.; Kulczyk-Malecka, J.; Kelly, P.; Zeng, Y.; Zhang, X.; Li, C.; Liu, H.;
        Rohbeck, N.; Xiao, P. Comparison of the oxidation behavior of a zirconium nitride
        coating in water vapor and air at high temperature. *Corros. Sci.* **2018**, *138*, 242–251,
        doi:10.1016/j.corsci.2018.04.015.

[12]   Krusin-Elbaum, L.; Wittmer, M. Oxidation kinetics of ZrN thin films. *Thin Solid
        Films* **1983**, *107*, 111–116, doi:10.1016/0040-6090(83)90013-5.

[13]   Shimada, S.; Ishil, T. Oxidation kinetics of Zirconium Carbide at relatively low
        temperatures. *J. Am. Ceram. Soc.* **1990**, *73*, 2804–2808, doi:10.1111/j.1151-
        2916.1990.tb06678.x.

[14]   Rao, G.A.R.; Venugopal, V. Kinetics and mechanism of the oxidation of ZrC. *J.
        Alloys Compd.* **1994**, *206*, 237–242, doi:10.1002/(SICI)1521-
        4176(199912)50:12<686::AID-MACO686>3.0.CO;2-M.

[15] Tamura, K.; Ogawa, T.; Fukuda, K. The oxidation behavior of ZrC coating and powder studied by laser Raman spectroscopy and X-ray diffraction. *J. Nucl. Mater.* **1990**, *175*, 266–269, doi:10.1016/0022-3115(90)90218-C.

[16] Shimada, S.; Inagaki, M.; Suzuki, M. Microstructural observation of the ZrC/ZrO$_2$ interface formed by oxidation of ZrC. *J. Mater. Res.* **1996**, *11*, 2594–2597, doi:10.1557/JMR.1996.0326.

[17] Harrison, R.W.; Lee, W.E. Processing and properties of ZrC, ZrN and ZrCN ceramics: a review. *Adv. Appl. Ceram.* **2015**, *115*, 294–307, doi:10.1179/1743676115y.0000000061.

[18] Kingery, W.D.; Bowen, H.K.; Uhlmann, D.R. *Introduction to Ceramics*; 2nd ed.; New York, 1976; ISBN 0471478601.

[19] Shimada, S. A thermoanalytical study on the oxidation of ZrC and HfC powders with formation of carbon. *Solid State Ionics* **2002**, *149*, 319–326, doi:10.1016/S0167-2738(02)00180-7.

[20] Shevchenko, A.S.; Lyutikov, R.A.; Andrievskii, R.A.; Terekhova, V.A. Oxidation of Zirconium and Niobium Carbides. *Powder Met. Met Ceram* **1980**, *19*, 48–52, doi:https://doi.org/10.1007/BF00798164.

[21] Shimada, S.; Nishisako, M.; Inagaki, M.; Yamamoto, K. Formation and microstructure of Carbon-containing oxide scales by oxidation of single crystals of Zirconium Carbide. *J. Am. Ceram. Soc.* 1995, *78*, 41–48.

[22] Shimada, S. Interfacial reaction on oxidation of carbides with formation of carbon. *Solid State Ionics* **2001**, *141–142*, 99–104, doi:10.1016/S0167-2738(01)00727-5.

[23] Voitovich, R.F.; Pugach, E.A. High-temperature oxidation of ZrC and HfC. *Sov. Powder Metall. Met. Ceram.* **1973**, *12*, 916–921, doi:10.1007/BF00794631.

[24] Jackson, H.F.; Lee, W.E. *Properties and Characteristics of ZrC*; Konings, R.J.M., Ed.; Elsevier Inc.: Oxford, 2012; ISBN 9780080560335.

[25] Katoh, Y.; Vasudevamurthy, G.; Nozawa, T.; Snead, L.L. Properties of Zirconium Carbide for nuclear fuel applications. *J. Nucl. Mater.* **2013**, *441*, 718–742, doi:10.1016/j.jnucmat.2013.05.037.

[26] Gasparrini, C.; Chater, R.J.; Horlait, D.; Vandeperre, L.; Lee, W.E. Zirconium Carbide oxidation: Kinetics and oxygen diffusion through the intermediate layer. *J. Am. Ceram. Soc.* **2018**, *101*, 2638–2652, doi:10.1111/jace.15479.

[27] Gasparrini, C.; Podor, R.; Horlait, D.; Chater, R.; Lee, W.E. Zirconium Carbide oxidation: Maltese cross formation and interface characterization. *Oxid. Met.* **2017**, *88*, 509–519, doi:10.1007/s11085-016-9672-6.

[28] Huang, J.H.; Kuo, K.L.; Yu, G.P. Oxidation behavior and corrosion resistance of vacuum annealed ZrN-coated stainless steel. *Surf. Coatings Technol.* **2019**, *358*, 308–319, doi:10.1016/j.surfcoat.2018.11.054.

[29] Shukla, S.; Seal, S. Mechanisms of room temperature metastable tetragonal phase stabilisation in Zirconia. *Int. Mater. Rev.* **2005**, *50*, 45–64, doi:10.1179/174328005X14267.

[30] Schell, N.; King, A.; Beckmann, F.; Ruhnau, H.U.; Kirchhof, R.; Kiehn, R.; Müller, M.; Schreyer, A. The High Energy Materials Science Beamline (HEMS) at PETRA III. *AIP Conf. Proc.* **2010**, *1234*, 391–394, doi:10.1063/1.3463221.

[31] Saringer, C.; Tkadletz, M.; Stark, A.; Schell, N.; Czettl, C.; Schalk, N. In-situ investigation of the oxidation behavior of metastable CVD $Ti_{1-x}Al_xN$ using a novel combination of synchrotron radiation XRD and DSC. *Surf. Coatings Technol.* **2019**, *374*, 617–624, doi:10.1016/j.surfcoat.2019.05.072.

[32] Baerlocher, C.; Cheetham, A.K.; David, W.I.F.; de Keijser, T.H.; Delhez, R.; Hill, R.J.; Izumi, F.; Jorgensen, J.D.; Langford, J.I.; Louër, D.; et al. *The Rietveld Method*; Young, R.A., Ed.; Oxford University Press: Oxford, 1993; Vol. 1; ISBN 9780198559122.

[33] NIST 660c certificate Available online: https://www-
      s.nist.gov/srmors/view_detail.cfm?srm=660c (accessed on Aug 25, 2020).

[34] Stinton, G.W.; Evans, J.S.O. Parametric Rietveld refinement. *J. Appl. Crystallogr.*
      2007, *40*, 87–95, doi:10.1107/S0021889806043275.

[35] Dinnebier, R.E.; Leineweber, A.; Evans, J.S.O. *Rietveld Refinement: Practical Powder*
      Diffraction Pattern Analysis using TOPAS; Walter de Gruyter GmbH & Co KG, 2018;
      ISBN 3110461382.

[36] Crystallography Open Database Available online:
      http://www.crystallography.net/cod/ (accessed on Aug 1, 2020).

[37] Crystallography Open Database, COD-ID 1538058. **2019**.

[38] Crystallography Open Database, COD-ID 1539496. **2019**.

[39] Crystallography Open Database, COD-ID 1011322. **2019**.

[40] Crystallography Open Database, COD-ID 1011099. **2019**.

[41] Crystallography Open Database, COD-ID 1521753. **2019**.

[42] Crystallography Open Database, COD-ID 1525705. **2019**.

[43] Crystallography Open Database, COD-ID 2108450. **2019**.

[44] Crystallography Open Database, COD-ID 9004141. **2019**.

[45] International Centre for Diffraction Data, PDF-2 Release, Card Number 00-035-
      0753. **2019**.

[46] International Centre for Diffraction Data, PDF-2 Release, Card Number 00-035-
      0784. **2019**.

[47] International Centre for Diffraction Data, PDF-2 Release, Card Number 00-038-
      1420. **2019**.

[48] Pawley, G.S. Unit-cell refinement from powder diffraction scans. *J. Appl.*
      Crystallogr. **1981**, *14*, 357–361, doi:10.1107/s0021889881009618.

[49] Garvie, R.C. The occurrence of metastable tetragonal zirconia as a crystallite size
      effect. *J. Phys. Chem.* **1965**, *69*, 1238–1243, doi:10.1021/j100888a024.

[50] Kanno, Y. Stability of metastable tetragonal ZrO_2 in compound powders and nucleation arguments. *J. Mater. Sci.* **1990**, *25*, 1987–1990, doi:10.1007/BF01045753.

[51] Reddy, G.L.N.; Ramana, J. V.; Kumar, S.; Kumar, S.V.; Raju, V.S. Investigations on the oxidation of zirconium nitride films in air by nuclear reaction analysis and backscattering spectrometry. *Appl. Surf. Sci.* **2007**, *253*, 7230–7237, doi:10.1016/j.apsusc.2007.03.004.

[52] Gendre, M.; Maître, A.; Trolliard, G. Synthesis of zirconium oxycarbide (ZrC_xO_y) powders: Influence of stoichiometry on densification kinetics during spark plasma sintering and on mechanical properties. *J. Eur. Ceram. Soc.* **2011**, *31*, 2377–2385, doi:10.1016/j.jeurceramsoc.2011.05.037.

[53] Garces, H.F.; Senturk, B.S.; Padture, N.P. In situ Raman spectroscopy studies of high-temperature degradation of thermal barrier coatings by molten silicate deposits. *Scr. Mater.* **2014**, *76*, 29–32, doi:10.1016/j.scriptamat.2013.12.008.

[54] Münz, W. Titanium aluminum nitride films: A new alternative to TiN coatings. *J. Vac. Sci. Technol. A Vacuum, Surfaces, Film.* **1986**, *4*, 2717–2725, doi:10.1116/1.573713.

[55] Fateh, N.; Fontalvo, G.A.; Gassner, G.; Mitterer, C. Influence of high-temperature oxide formation on the tribological behaviour of TiN and VN coatings. *Wear* **2007**, *262*, 1152–1158, doi:10.1016/j.wear.2006.11.006.

[56] Chen, L.; Paulitsch, J.; Du, Y.; Mayrhofer, P.H. Thermal stability and oxidation resistance of Ti-Al-N coatings. *Surf. Coatings Technol.* **2012**, *206*, 2954–2960, doi:10.1016/j.surfcoat.2011.12.028.

[57] Muñoz Tabares, J.A.; Anglada, M.J. Quantitative analysis of monoclinic phase in 3Y-TZP by Raman pectroscopy. *J. Am. Ceram. Soc.* **2010**, *93*, 1790–1795, doi:10.1111/j.1551-2916.2010.03635.x.

[58] Gilman, J.J.; Galvanov, B.A.; Kindrachuk, V.M.; Zhang, L.C.; Cheong, W.C.D.; Ackland, G.J.; Levitas, V.I.; Fischer-Cripps, A.C.; Bhushan, B.; Xiaodong, L.; et al.

High-Pressure Surface Science and Engineering; Gogotsi, Y., Domnich, V., Eds.; 1st ed.; Routledge: New York, 2004; ISBN 9780750308816.

[59]   Naumenko, A.P.; Berezovska, N.I.; Biliy, M.M.; Shevchenko, O. V. Vibrational analysis and Raman spectra of tetragonal Zirconia. *Phys. Chem. Solid State* **2008**, *9*, 121–125.

[60]   Rutile TiO_2 Raman peaks Available online: https://rruff.info/rutile/display=default/R110109 (accessed on Nov 2, 2020).

[61]   International Centre for Diffraction Data, PDF-2 Release, Card Number 00-065-0687. **2019**.

[62]   International Centre for Diffraction Data, PDF-2 Release, Card Number 00-049-1642. **2019**.

[63]   International Centre for Diffraction Data, PDF-2 Release, Card Number 01-072-7115. **2019**.

[64]   International Centre for Diffraction Data, PDF-2 Release, Card Number 01-070-7347. **2019**.

[65]   Krishnamurti, D. The Raman spectrum of rutile. *Proc. Indian Acad. Sci. - Sect. A* **1962**, *55*, 290–299.

[66]   Ferrari, A.C.; Robertson, J. Interpretation of Raman spectra of disordered and amorphous carbon. *Phys. Rev. B* **2000**, *61*, 14095, doi:10.1007/BF02543692.

Publication III

Microstructural and micro-mechanical investigation of cathodic arc evaporated ZrN/TiN multilayer coatings with varying bilayer thickness

Florian Frank, Christina Kainz, Michael Tkadletz, Christoph Czettl, Markus Pohler, Nina Schalk

Microstructural and micro-mechanical investigation of cathodic arc evaporated ZrN/TiN multilayer coatings with varying bilayer thickness

Florian Frank[1], Christina Kainz[1], Michael Tkadletz[2], Christoph Czettl[3], Markus Pohler[3], Nina Schalk[1]

[1] Christian Doppler Laboratory for Advanced Coated Cutting Tools at the Department of Materials Science, Montanuniversität Leoben, Franz–Josef–Strasse 18, 8700 Leoben, Austria

[2] Department of Materials Science, Montanuniversität Leoben, Franz–Josef–Strasse 18, 8700 Leoben, Austria

[3] Ceratizit Austria GmbH, Metallwerk–Plansee–Strasse 71, 6600 Reutte, Austria

Abstract

Modifying the architecture of multilayer hard coatings allows to adjust the mechanical properties of these materials for a given application. Within this work, the effect of the bilayer thickness (Λ) and the individual sublayer thickness ratio on the microstructure and mechanical properties of ZrN/TiN multilayer coatings was investigated. Multilayer coatings with Λ of 570, 320 and 35 nm were deposited by cathodic arc evaporation and compared to TiN and ZrN single-layer coatings. The microstructure was investigated by X-ray diffraction (XRD) and scanning electron microscopy. All coatings exhibit a single phase face-centred cubic structure and a predominant (111) texture. A columnar structure was observed for all coatings and grain growth extending beyond the ZrN/TiN interfaces was evident in all multilayers. For all coatings, compressive residual stresses were determined by XRD using the $\sin^2\psi$ method, where the multilayer sample with the largest Λ exhibited the highest compressive residual stress of -1.7 ± 0.2 GPa. Lower compressive residual stresses could be correlated

with decreasing Λ and decreasing ZrN:TiN thickness ratio. Nanoindentation experiments as well as micro-mechanical bending tests were conducted to assess the mechanical properties of the coatings. The ZrN/TiN multilayer sample with Λ of 35 nm showed the highest hardness of 28.0 ± 1.1 GPa. This value is similar to the TiN single-layer and higher compared to the ZrN single-layer, which exhibited a hardness of 27.9 ± 1.4 GPa and 25.8 ± 1.3 GPa, respectively. While the ZrN single-layer showed the highest fracture toughness, the ZrN/TiN multilayer samples were identified as the mechanically stiffest and strongest of the investigated coatings, since they exhibited a higher fracture stress compared to the single-layer coatings. The obtained results allow to optimise the architecture of ZrN/TiN multilayer coatings yielding the desired coating properties for application in the cutting industry.

Keywords: Fracture toughness, mechanical properties, multilayer, ZrN, TiN, arc evaporation

1. Introduction

Transition metal nitride hard coatings grown by cathodic arc evaporation (CAE) are widely used to enhance the performance of cutting tools in industrial machining applications. The required properties for such coatings include high hardness, good oxidation resistance as well as high thermal stability. Furthermore, the fracture stress and fracture toughness are crucial properties for machining applications, as they define the initiation and propagation of cracks in the coatings and may thus be correlated with the performance of the coatings during cutting tests [1–3]. Since a combination of high hardness and good fracture toughness is desirable, but inherent mutually exclusive for most transition metal nitride coatings [4], attempts are made to overcome this obstacle. One method to achieve this goal relies on the modification of the coating architecture by combining two materials in a multilayer approach. Ideally, the two counterparts should

exhibit different intrinsic properties in regard of e.g. microstructure, elastic properties and chemical composition [2,5,6]. In addition to the material choice within the respective layers, the layer thickness strongly influences the mechanical properties [6–8]. Thus, properties such as the fracture behaviour can be tailored and subsequently optimised by adapting the bilayer thickness (Λ) [6–10]. This enhancement can be achieved by alternating stress fields at the interfaces [6,11–15], which might lead to crack deflection and thus retard the crack propagation throughout the interfaces [16]. Alternating stress fields can be induced by coherency strains due to a mismatch in the lattice parameter and/or differences in the elastic properties of the individual sublayers [8,11,17]. Besides the fracture properties, also the hardness can be enhanced by a multilayered architecture compared to the respective single layers. Hereby, the induced stress fields might also hinder dislocation movement, thus increasing the hardness [8,11,18].

ZrN and TiN are both intrinsically hard materials with a good thermal and chemical stability, making them excellent candidates for the deposition of multilayer ZrN/TiN protective hard coatings [19–21]. Both materials crystallise in the face-centred cubic (fcc) structure with a lattice mismatch of about 7–8% [10,22]. This lattice mismatch can be overcome by misfit dislocations, however, it might also induce high coherency strains at the interface that can improve the mechanical properties of the ZrN/TiN multilayer coatings compared to single-layer coatings [8,11,17]. Various physical vapour deposition methods are used for the fabrication of ZrN/TiN multilayer coatings, such as magnetron sputtering [7,9,22,23], CAE [24,25] and pulsed laser deposition [26]. Most of these studies investigated the influence of the deposition conditions or the bilayer architecture on microstructural, mechanical and tribological properties of the coatings. However, the influence of Λ on the fracture behaviour of the ZrN/TiN coating system has not yet been studied.

Within this study, the microstructure and mechanical properties of CAE ZrN and TiN single and ZrN/TiN multilayer coatings with Λ of 570, 320 and 35 nm were

investigated, applying different characterization methods such as X-ray diffraction (XRD), scanning electron microscopy (SEM), energy-dispersive X-ray diffraction (EDX) and nanoindentation. The fracture behaviour was determined by micro-mechanical bending tests, which allowed to systematically assess the influence of the multilayer architecture on the fracture stress and fracture toughness of the ZrN/TiN coating system.

2.   Experimental details

The ZrN and TiN single-layer and the ZrN/TiN multilayer coatings with different Λ were deposited using CAE in an industrial scale Oerlikon Balzers Innova deposition plant. The single-layer and multilayer coatings were deposited with Zr and Ti cathodes, which were operated in DC mode. Cemented carbide cutting inserts in SNUN geometry (ISO 1832 [27]) with a composition of 92 wt% WC, 6 wt% Co and 2 wt% mixed carbides as well as mild steel foil were used as substrates and mounted on a rotational holder to undergo two-fold rotation. ZrN/TiN multilayer coatings exhibiting 10 and 21 bilayers with different Λ of 570 and 320 nm, respectively, were deposited by opposed cyclic activation and deactivation of the Zr and Ti cathodes. The multilayer coating with the bilayer thickness of 35 nm was realised through the rotation of the substrates. After this deposition step, a ZrN protection layer with a thickness of about 360 nm was deposited on this sample. All samples were synthesised in N_2 and Ar atmosphere at a total pressure of 3.0 Pa, using a bias voltage of −100 V. The deposition temperature was kept constant at 425 °C. After the deposition process, the coated mild-steel foil was dissolved in diluted nitric acid to obtain powders of the coatings.

A Zeiss GeminiSEM 450 was used to investigate the cross-sections of the coatings, which were prepared utilising a Hitachi IM4000+ ion milling system. The elemental composition of the single-layer coatings was quantified by EDX using an Oxford Ultim Extreme detector mounted on the above mentioned SEM. Additionally, EDX maps of the multilayer coatings with Λ of 570, 320 and 35 nm were recorded. The microstructure of the coatings was analysed applying a Bruker D8 Advance diffractometer, operated in

parallel beam configuration using Cu-Kα (λ = 1.54186 Å) radiation. The diffraction patterns were recorded in locked-coupled mode with a step size of 0.02° and a counting time of 1 s per step, using an energy dispersive Sol-X detector. Powder, pole figure and residual stress measurements were conducted on a Bruker D8 Advance DaVinci XRD using Cu-Kα radiation and a position sensitive LynxEye XE-T detector. The domain size of the powdered coatings was investigated via Bragg-Brentano scans and subsequent Rietveld refinement of the recorded diffractograms using the software TOPAS 6 (Bruker AXS). The patterns were recorded with a step size of 0.02° and a counting time of 1 s per step. The texture of the coatings on cemented carbide substrates was determined with pole figure measurements in parallel beam configuration of the 111, 200 and 220 peaks. Pole figures were recorded for tilt angles from 0 to 84° and rotation angles from 0 to 360°, with a step size of 3° for both cases. Data processing and visualization of the recalculated pole figures as well as of the inverse pole figures was carried out using the MTEX toolbox [28]. Residual stress analysis was conducted using the $\sin^2\psi$ technique in side-inclination on the 200 peak. Twelve equally spaced inclinations from 0 to 0.9 $\sin^2\psi$ were recorded and evaluated using the software Leptos (Bruker AXS). The Hill grain interaction model was applied to calculate the X-ray elastic constants [29] using elastic constants from literature as input [30,31].

Hardness and Young's modulus were measured by nanoindentation, using an Ultra Micro Indentation System (UMIS) from Fischer-Cripps Laboratories equipped with a diamond Berkovich indenter tip by Synton-MDP. In order to reduce the surface roughness, the coatings were mirror polished using a 3 µm and 1 µm diamond suspension prior to the hardness measurements. The ZrN top-layer of the sample with a Λ of 35 nm was carefully removed by mechanical grinding using SiC-paper with 1200 grade, followed by polishing using a 3 µm and 1 µm diamond suspension. The load range was between 30 mN and 12 mN, with a decrement of 0.75 mN and the data was analysed according to Oliver and Pharr [32]. To determine the fracture stress and fracture

toughness of the coatings, micro-mechanical bending tests were conducted on two sets of free-standing unnotched and notched cantilevers, respectively. At least three specimens were tested for each set of cantilevers per investigated coating. The cantilevers were prepared using focused ion beam (FIB) milling on a Versa 3D DualBeam system by FEI. The bending length of the cantilevers was ~9 μm and the cross-sectional area was ~3 × 3 μm2. Furthermore, half of the specimens were notched at about 1 μm from the cantilevers' support. The cantilevers were loaded until fracture using a cono-spherical diamond tip mounted on a Hysitron TriboIndenter TI950. The displacement-controlled loading was conducted at a rate of 5 nm/s and the fracture stress was estimated from the recorded load-displacement curves according to the linear-elastic bending theory. The fracture toughness was evaluated according to Matoy et al. and the notch depth was measured post mortem using the aforementioned DualBeam system by FEI [33].

3.   Results and discussion

To gain insight into the microstructure of the single and multilayer coatings, SEM images of cross-sections of all coatings are shown in Fig. 1. Although ZrN (Fig. 1a) and TiN (Fig. 1b) both exhibit grains that are elongated in growth direction, differences in the grain size are visible. The average grains of the ZrN coatings appear to be smaller compared to TiN. For all ZrN/TiN multilayer coatings (Fig. 1c–f) with varying Λ of 570, 320 and 35 nm, the alternating layer structure is clearly visible and a fine-grained microstructure can be observed. The thickness ratio of the individual ZrN and TiN sublayers ZrN:TiN was determined from the SEM images and is 6.1, 3.2 and 3.4 for the multilayer coatings with Λ of 570, 320 and 35 nm, respectively. The sublayer thickness of the TiN layer was kept constant at ~80 nm for the coatings with Λ of 570 and 320 nm and the 35 nm coating exhibited a TiN layer thickness of 8 nm. When taking a closer look at the cross-sections of the multilayer coatings it becomes further apparent that several grains extend through multiple layers, evidencing (semi-)coherent growth for all multilayers. While no macroparticles are visible in the cross-section images of the ZrN

and TiN single-layer coatings, a low number of macroparticles can be observed in the cross-sections of the multilayer coatings [34–36].
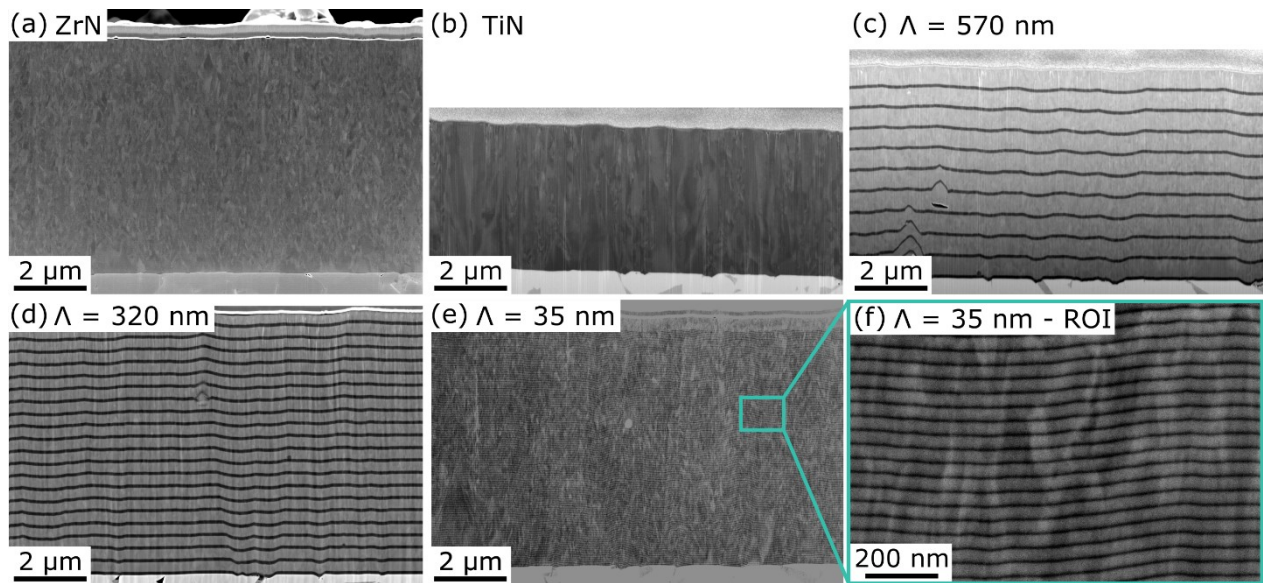
Fig. 1. *SEM images of FIB prepared cross-sections of (a) ZrN and (b) TiN single-layer coatings and (c–e) ZrN/TiN multilayer coatings with different bilayer periods (Λ). (f) A region of interest (ROI) with a higher magnification of the multilayer coating with Λ = 35 nm is shown. TiN layers appear dark, ZrN layers light.*

In Fig. 2 the elemental distribution of the multilayer coatings with a Λ of 570 and 320 nm is depicted; EDX maps for the smallest Λ of 35 nm are not shown, as the Λ is too small to resolve the chemical composition of the individual sublayers using SEM/EDX. No intermixing of the ZrN and TiN layers is observed, which is also supported by a positive enthalpy of formation over the whole compositional range [37]. Minor fluctuations can be observed for the N content, which were also present in the single-layer ZrN and TiN coatings, which exhibited a N content of 52 at.% and 54 at.%, respectively. This can be explained by the vicinity of the Ti-Lα (0.452 keV) and N-Kα (0.392 keV) lines in the EDX spectrum, leading to an overestimation of the N content in the Ti rich regions. Since the deposition conditions were equal for the single-layer and multilayer coatings, no significant compositional deviations are expected between single-layer coatings and the corresponding individual ZrN and TiN sublayers in the multilayer coatings.
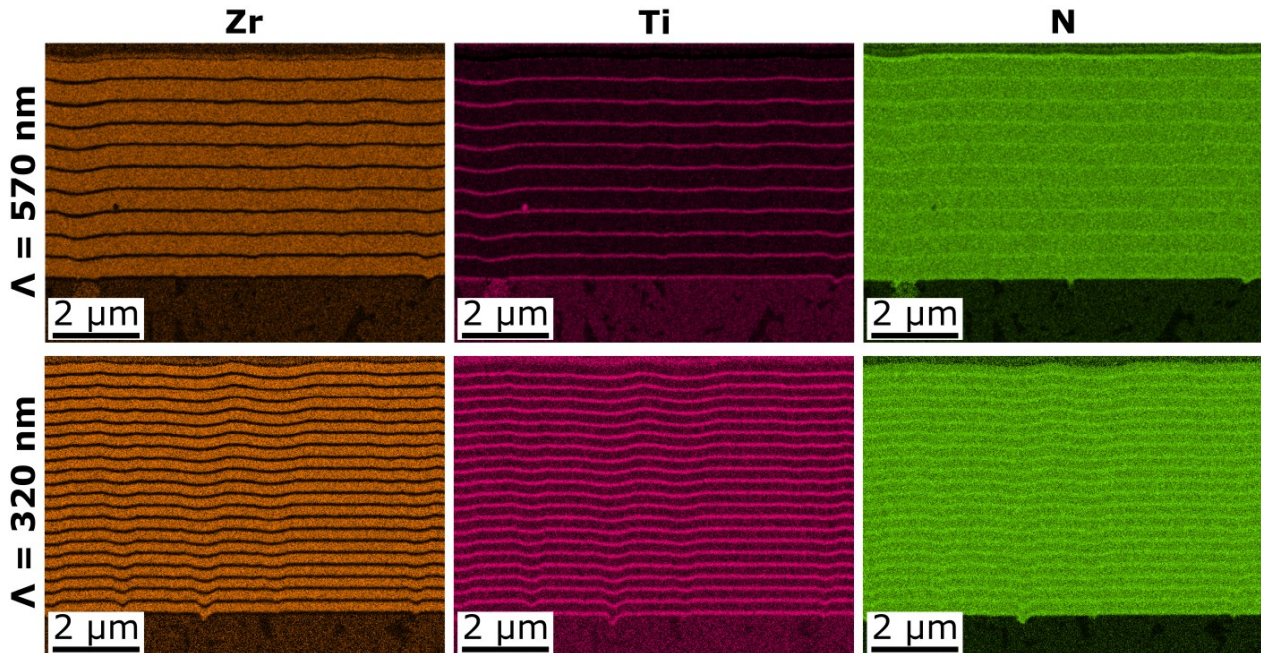
Fig. 2. *EDX maps of Zr (orange), Ti (pink) and N (green) of FIB prepared cross-sections of the two multilayer coatings with a Λ of 570 nm and 320 nm.*

X-ray diffractograms of all coatings are displayed in Fig. 3a. The reference positions for fcc-ZrN (PDF 00-035-0753 [38]) and fcc-TiN (PDF 00-038-1420 [38]), as well as for WC (PDF 00-003-1096 [38]) from the substrate are indicated with dashed lines. All coatings exhibit an fcc structure. While for all multilayer coatings distinct fcc-ZrN peaks are evident, the fcc-TiN 111 peak is only visible in the multilayer coatings with Λ of 570 and 320 nm. The peaks are shifted to lower diffraction angles compared to the reference position, indicating a compressive residual stress state for all samples. The considerably lower peak intensity arising from the TiN phase compared to the ZrN peaks can be attributed to two effects: first, the individual sublayer thickness of the TiN layers is smaller compared to the thicker ZrN layers, resulting in a smaller diffracting volume for TiN compared to ZrN. Second, the atomic form factor, which can be related to the structure factor and the intensity of the diffraction peaks, is about twice as high for Zr compared to Ti, resulting in a lower scattering intensity for the TiN layer compared to the ZrN layer [39]. When comparing the TiN 111 peak of the multilayer coatings with a Λ of 570 and 320 nm it becomes apparent that the intensity is higher for the 320 nm coating.

This can be related to the lower ZrN:TiN layer thickness ratio of this coating compared to the coating with Λ of 570 nm. No TiN related peaks are visible in the diffractogram of the coating with the Λ of 35 nm, although the ZrN:TiN thickness ratio is comparable to the coating with a Λ of 320 nm, which exhibits TiN peaks. Thus, another effect than the ZrN:TiN layer thickness ratio has to be considered that explains the absence of the TiN peaks. One explanation might be related to high coherency strains, originating from the lattice mismatch between the ZrN and TiN crystal lattice of about 7–8% [10,22]. The coherency strains might distort the crystal lattice in such a way that the TiN peaks are not detectable with conventional XRD methods. This effect is more pronounced in the 35 nm coating compared to the other multilayer coatings, since the TiN layer thickness is considerably smaller in the 35 nm multilayer coating. However, the experimental validation of this hypothesis is beyond the scope of this work. Both the ZrN and TiN single-layer coatings display strong 111 contributions. The TiN coating does not exhibit a 200 peak, whereas the ZrN shows a small 200 peak, indicating a more pronounced (111) texture of the TiN coating. Although the (200) orientation displays a lower surface free energy compared to the (111) orientation, a (111) preferred orientation is often reported for ZrN coatings deposited by CAE at high bias voltages [40–42]. According to Abadias et al., the occurrence of the (111) preferred orientation at high bias voltages can be explained by a re-nucleation mechanism of the growing grains [43]. The re-nucleation is induced by a high defect density due the ion bombardment with high energetic ions. The defects act as sites for secondary nucleation and grain boundary migration, which favours the formation of the plane with the fastest growth rate, being the (111) plane for fcc crystals [43,44]. Compared to the ZrN single-layer coating, the multilayer coatings show a similar texture with a stronger contribution of the 111 peak and a smaller 200 peak. Fig. 3b shows the size of the coherently diffracting domains, determined from powdered coatings by Rietveld refinement. It can be assumed that the size of the coherently diffracting domains correlates with the grain size, although the absolute values for the

size of the coherently diffracting domains are usually smaller than the actual grain size [45–48]. TiN exhibits the largest domain size, followed by ZrN, which is in accordance with the SEM images in Figs. 1a and b. Regarding the multilayer coatings, the domain size decreases with decreasing Λ. González-Carmona et al. observed a similar trend of a decreasing domain size in ZrN/TiN multilayer with decreasing Λ [7]. They attributed the decrease in domain size to the restricted grain growth at the ZrN-TiN interface. The grain growth further decreases with decreasing Λ, which can be explained by an in- crease in the interface-to-volume ratio with decreasing Λ. Regarding the present work, this explanation seems counter-intuitive, as the grain growth extends through multiple layers and new grains do not form exclusively at the ZrN-TiN interface. However, it can be assumed that few dislocations form at the ZrN-TiN interface, resulting in semi-coherent interfaces. Similar to the defects arising from the high bias voltage, these dislocations might contribute to re-nucleation of the grains [43]. While the dislocations might not stop the grain growth at the interface, they may at least hinder it.
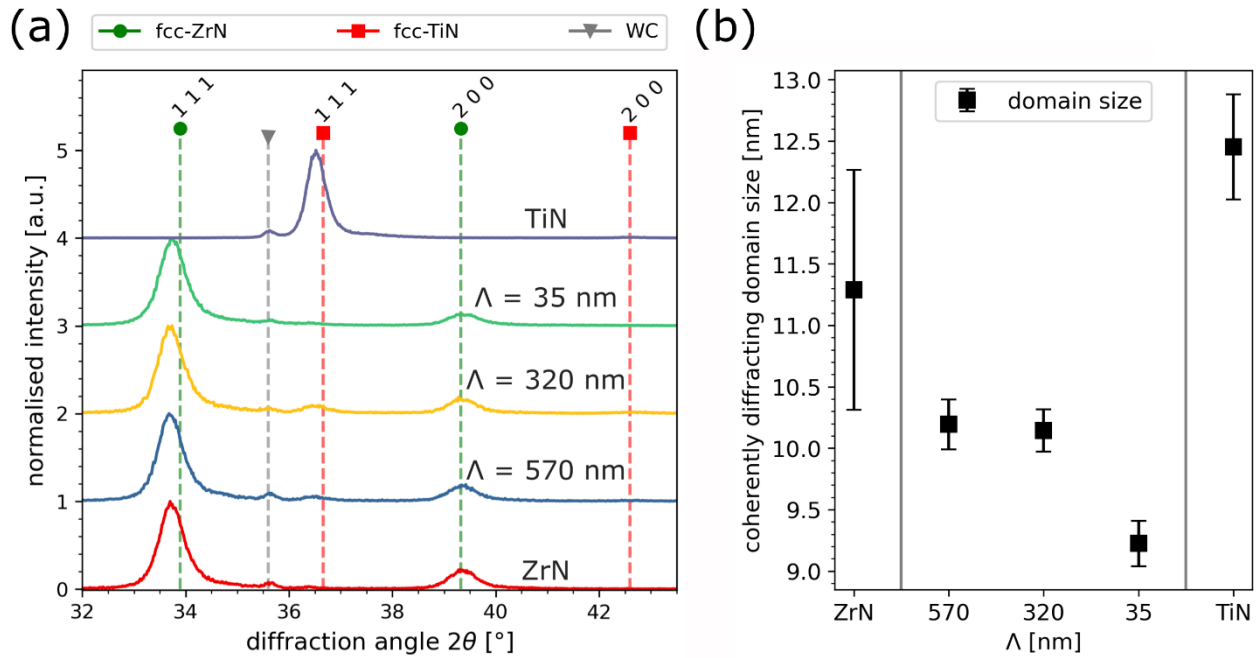
Fig. 3. *(a) X-ray diffractograms of ZrN and TiN single-layer, as well as ZrN/TiN multilayer coatings with Λ of 570, 320 and 35 nm and (b) size of coherently diffracting domains, determined using Rietveld refinement from powdered coatings.*

In order to investigate the influence of the multilayer architecture on the coating texture, XRD pole-figure (PF) measurements were conducted. The recorded PF of the 111, 200 and 220 peaks were recalculated using the MTEX toolbox [28] and subsequently, the inverse pole figures (IPFs) in growth direction were calculated. The PFs (not shown) revealed a fibre texture for all coatings. The inverse pole figures (IPF), which depict the texture of the coatings in growth direction, are displayed in Fig. 4. There, the IPFs for the fcc-ZrN phase are shown in the first row, the IPFs for the fcc-TiN phase are depicted in the second row. In the case of the coating with a Λ of 35 nm, only the IPF of the fcc-ZrN phase is given, since the fcc-TiN phase was not detectable for this coating. The ZrN coating shows a (111) texture with minor contributions from the (311), (211), and (100) planes. It is evident that the multilayer coatings display a similar texture compared to the single-layer ZrN sample. However, the (111) preferred orientation becomes more pronounced with decreasing Λ, as the intensity of the minor contributions from the (311),

(211) and (100) planes decrease. One explanation for the more pronounced (111) texture with decreasing Λ might be related to an increase in defect density due to the increased interface-to-volume ratio in coatings with lower Λ compared to coatings with larger Λ. As a result, more dislocations and imperfections are incorporated within the crystal [7]. A higher number of defects would result in more nucleation sites, which favours the crystal growth in [111] direction [43]. The TiN single-layer coating displays a very strong (111) texture with no contributions from other diffraction planes. The fcc-TiN phase of the multilayer coatings with Λ of 570 and 320 nm displays a different texture compared to the single-layer TiN coating; the texture correlates with the one of the ZrN single-layer coating. This preferred orientation alignment of the two phases in the multilayer coatings indicates (semi-)coherent growth of ZrN and TiN layers, whereby the thicker ZrN layers act as a template for the thinner TiN layers.
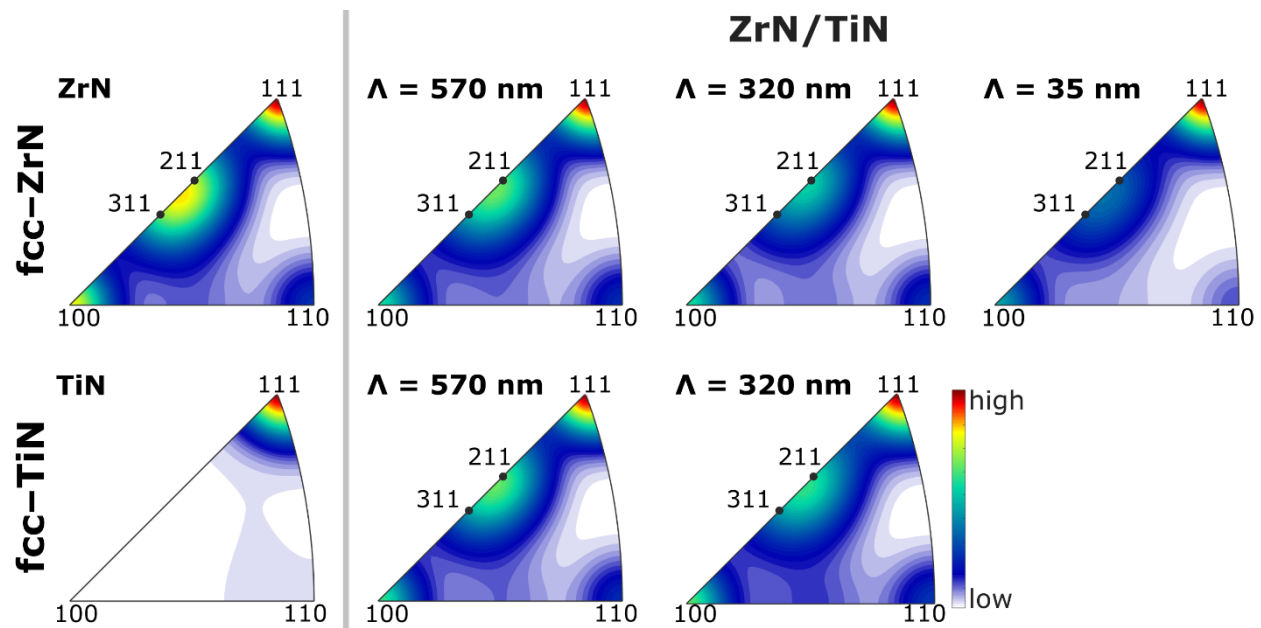
Fig. 4. *Inverse pole figures (IPFs) in growth direction, recorded for the face-centred cubic (fcc)-ZrN phase of ZrN single-layer, and ZrN/TiN multilayer coatings with Λ of 570 nm, 320 nm and 35 nm and the fcc-TiN phase of the TiN single-layer and the ZrN/TiN multilayer coatings with a Λ of 570 nm and 320 nm.*

XRD residual stress measurements were conducted to assess the macroscopic stress in the coatings. The results are shown in Fig. 5a. The 200 peak of the fcc-ZrN and fcc-TiN phase was evaluated for the ZrN and TiN single-layer coatings, respectively. An evaluation of the fcc-TiN 200 peak of the multilayer coatings was only possible for the coating with a Λ of 320 nm, as the peak-to-background ratio was too low in the coatings with a Λ of 570 and 35 nm. The ZrN and TiN single-layer coatings exhibit a compressive residual stress of -1.6 ± 0.2 and -1.1 ± 0.3 GPa, respectively. Within the error, the residual stress of the fcc-ZrN phase of the ZrN/TiN multilayer coatings is comparable to the residual stress of the ZrN single-layer coating. A slightly lower compressive residual stress is observed for the multilayer coating with a Λ of 320 nm compared to the multilayer coating with a Λ of 570 nm. The lower ZrN:TiN thickness ratio in the 320 nm compared to the 570 nm coating might contribute to the stress relief in the ZrN layer. In CAE coatings, the compressive residual stress emerges mainly due to the high energy ion bombardment during the deposition process. In multilayer coatings, additional stress contributions from the interface between the individual sublayers arise that influence the macroscopic stress state [49]. Several researchers investigated the dependence of the residual stress on the Λ in multilayer coatings [7,50,51]. They found that the stress usually decreases with decreasing Λ and reaches the level of the corresponding single-layer coatings at small Λ. This effect can be attributed to the increased interface-to-volume ratio with decreasing Λ, which generates a higher lattice distortion that leads to a dissipation of the system stress [7]. This dissipation of energy might also contribute to the lower residual stress in the 320 nm coating. The stress in the TiN layer of the 320 nm multilayer coating is comparable within the error to the stress of the single-layer TiN coating.

Hardness and Young's modulus of all investigated coatings are displayed in Fig. 5b. The TiN single-layer coating exhibits a higher hardness of 27.9 ± 1.4 GPa compared to the ZrN coating with 25.8 ± 1.3 GPa. This behaviour can be related to differences in the electronic structure of the two coating systems, which is also supported

by first-principles density functional theory calculations [52]. Furthermore, the more pronounced (111) texture in the TiN coating might contribute to the higher hardness compared to the less textured ZrN coating. In ZrN and TiN, the Schmid factor of the (111) plane is known to be the lowest, which results in the highest hardness of the material in [111] direction [53,54]. ZrN/TiN multilayer coatings show an increase in hardness compared to the single-layer ZrN coating of about 1 to 2 GPa, whereby the highest hardness of 28.0 ± 1.1 GPa can be found for the smallest Λ of 35 nm. The hardness increase for multilayer coatings, which is even more pronounced when decreasing the bilayer period, can be attributed to three effects. First, the smaller grain size of the multilayer coatings compared to the single-layer ZrN leads to higher hardness due to Hall-Petch strengthening. Second, as the preferred orientation changes to a more pronounced (111) orientation with decreasing Λ (see Fig. 4), a hardness increase may also be ascribed to this change in texture [53,54]. Third, coherency strains in the multilayer coating that arise due to the lattice mismatch between the individual sublayers act as obstacles for the dislocation motion [8,11,17]. The Young's modulus is lowest for the ZrN single-layer and highest for the TiN single-layer coating. Again, this behaviour can be related to the electronic structure of both materials, as computational results of several researchers have shown a similar trend for TiN and ZrN [55–59]. Hoerling et al. explained the differences in the Young's modulus with a larger atomic radius of Zr compared to the smaller Ti atom. Taking into account Coulomb's law, the ionic contribution to the cohesive strength decreases with increasing atomic radius, leading to a reduced Young's modulus for ZrN compared to TiN [58]. An increase in Young's modulus of about 20 GPa is observed for the multilayer coatings compared to single-layer ZrN. This behaviour can be attributed to the combination of the ZrN and TiN layers, which results in a Young's modulus that is between the values of the individual layer components. As the significantly thicker ZrN layers dominate within the multilayer structure, the values of the Young's modulus are closer to the ZrN single layer compared to TiN. The different bilayer thicknesses of the

multilayer samples seem to have a minor influence on the Young's modulus as the values only vary within the standard deviation.
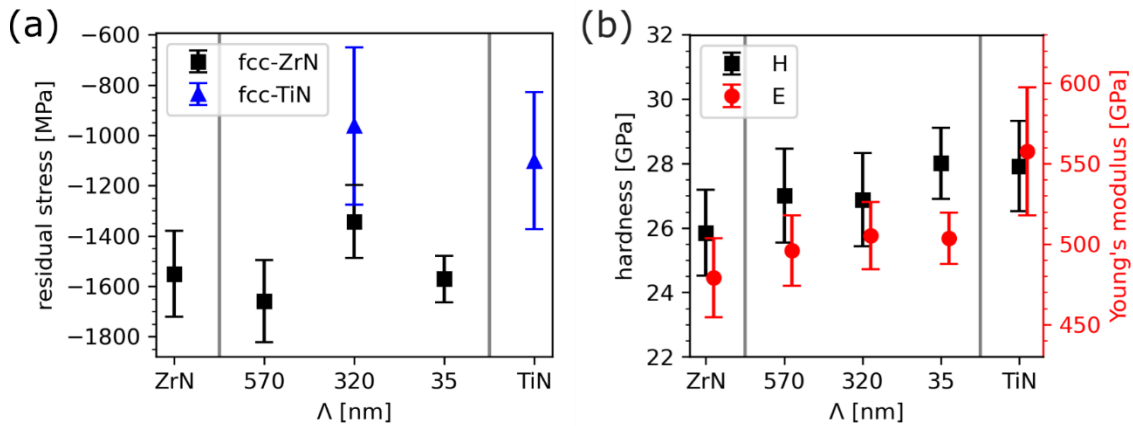

Fig. 5. *(a) Residual stress of the fcc-ZrN and fcc-TiN phases, as well as (b) hardness and Young's modulus of the investigated coatings.*

As hardness and Young's modulus are not the only properties influencing the performance of the coatings during machining applications, focus should also be placed on investigating the fracture behaviour of the coating materials. Therefore, micro-mechanical bending tests were conducted on free-standing cantilevers, which were prepared using FIB milling. Fracture stress and fracture toughness were quantitatively determined from the stress-deflection curves of notched and unnotched cantilevers, respectively. The recorded stress-deflection curves of the unnotched cantilevers are shown in Fig. 6a. All coatings display a linear-elastic bending behaviour until instantaneous fracture occurs, indicating that no plastic deformation takes place during the bending test. The calculated fracture stress and fracture toughness values are summarised in Fig. 6b. The ZrN and TiN single-layer coatings show the lowest fracture stress of 2.9 ± 0.6 GPa and 3.5 ± 0.4 GPa, respectively. For the ZrN/TiN multilayers, an increase in fracture stress compared to the single-layer coatings is observed, with values ranging from 4.2 to 4.5 GPa. This increase may be attributed to Hall-Petch strengthening as a result of the smaller grain size in the multilayer coatings. Regarding the fracture toughness of the coatings, a different trend is observed. The highest fracture toughness

was found for the single-layer ZrN coating with 4.0 ± 0.2 MPa·m$^{1/2}$, which is higher than the maximum values of magnetron sputtered ZrN coatings reported in literature ranging from 1.7 to 3.6 MPa·m$^{1/2}$ [60,61]. It has to be noted that the wide range of literature values for the fracture toughness results from different deposition conditions and the accompanied microstructural changes of the investigated coatings. Furthermore, to the best of our knowledge, quantitative fracture toughness values are only reported for sputtered ZrN; additionally, the fracture toughness of these coatings was determined using the internal energy induced cracking method [62]. The TiN single-layer coating showed the lowest fracture toughness of the investigated coatings with 2.6 ± 0.4 MPa·m$^{1/2}$, which is in good agreement with literature data for TiN coatings, ranging from 1.19 to 2.7 MPa·m$^{1/2}$ [45,56,62–66]. The fracture toughness of the ZrN/TiN multilayer coatings was found to lie between the values for the ZrN and TiN single-layer coatings. While the coatings with a Λ of 570 and 320 nm show almost identical values of 3.5 ± 0.3 MPa·m$^{1/2}$ and 3.5 ± 0.2 MPa·m$^{1/2}$, respectively, a slight decrease to 3.1 ± 0.4 MPa·m$^{1/2}$ can be observed for the multilayer coating with the smallest Λ of 35 nm. The grain size and preferred orientation seem to have the strongest influence on the fracture behaviour. First of all, the smaller grain size in the ZrN single-layer and the ZrN/TiN multilayer coatings seems to increase the fracture toughness compared to the larger grained single-layer TiN coating. This behaviour can be explained by crack propagation occurring predominantly at the grain boundaries. The grain boundaries represent paths of lower fracture energy and thus cracks propagate mainly along the grain boundaries until they are deflected at an adjacent grain boundary. With a decrease of the grain size, the rate of deflection events increases, which leads to an increase in fracture toughness [5,67,68]. However, the fracture toughness does not follow the trend observed in the grain size determined by Rietveld refinement, where the fracture toughness of the multilayer coatings would be higher compared to the ZrN single-layer coating and would also increase with decreasing Λ. This contradictory behaviour might be explained by the dependence of the fracture toughness

on texture. As the pronounced (111) texture decreases in the multilayer coatings compared to TiN and decreases even further in the ZrN coating, the fracture toughness can be related to texture differences between the investigated coatings. Huang et al. investigated the fracture toughness of sputter deposited ZrN coatings [60]. They observed a texture dependence of the fracture toughness and found a higher value for coatings with less pronounced (111) texture compared to coatings with a stronger (111) preferred orientation.
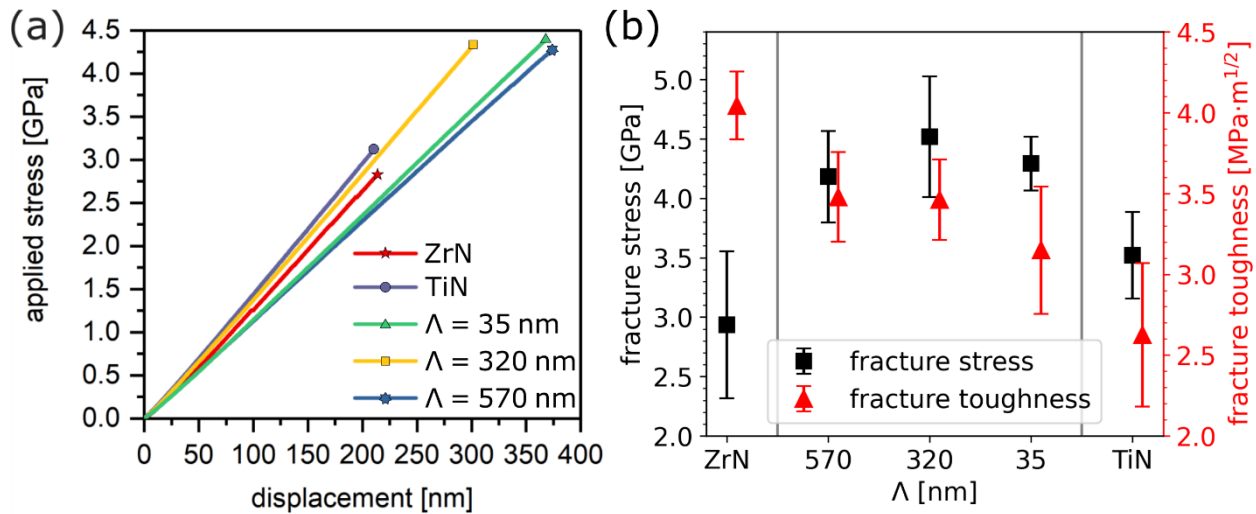
Fig. 6. *(a) Stress deflection curves, as well as (b) fracture stress and fracture toughness, determined from micro-cantilever bending tests of the ZrN and TiN single-layer, as well as the ZrN/TiN multilayer coatings.*

The post-mortem fracture cross-sections of the unnotched cantilevers correlate well with the SEM images of Fig. 1. They display finer grains for the ZrN single-layer coating (Fig. 7a) and the ZrN/TiN multilayer coatings with varying Λ (Fig. 7c–e) compared to the TiN coating single-layer (Fig. 7b). The multilayer coatings with Λ of 570 and 320 nm show grain growth through the clearly visible ZrN and TiN layers. No individual ZrN and TiN layers are visible in the multilayer coating with the smallest Λ of 35 nm. It can be seen that fracture occurs predominantly along the grain boundaries for all coatings, although transgranular fracture cannot be fully excluded. The darker section in the upper left part in the cross-sections of the ZrN and the darker section from the

middle to the bottom of the coating with Λ of 570 nm may be related to macroparticles in the coatings. To minimise the influence of macro-particles on the fracture behaviour, at least three different cantilevers where no macroparticles were visible in the post mortem cross-section images were chosen for the determination of the fracture properties. Considering the fact that only few macroparticles are visible in the SEM cross-section images (Fig. 1), it can be assumed that the influence of the macroparticles on the fracture properties is minor.

4. Conclusion

Within this study, the microstructure and mechanical properties of cathodic arc evaporated ZrN and TiN single-layer, as well as ZrN/TiN multilayer coatings with varying bilayer thickness (Λ) and different individual layer thickness were investigated. X-ray diffraction and scanning electron microscopy investigations showed (semi-)coherent grain growth for the multilayer coatings. With decreasing Λ, a smaller size of coherently diffracting domains, as well as a more pronounced preferred (111) orientation was observed. Both might be related to grain re-nucleation due to dislocations at the ZrN/TiN interface that arise from differences in the lattice parameter between ZrN and TiN. The combination of smaller grain size, a more pronounced (111) texture and coherency strains leads to the highest hardness values of about 28 GPa for the ZrN/TiN multilayer coating with the smallest Λ. Fracture stress and fracture toughness were evaluated with micro-mechanical bending tests of unnotched and notched cantilevers, respectively. The ZrN/TiN multilayer coatings exhibited a higher fracture stress compared to the single layers, which can be attributed to Hall-Petch strengthening in the multilayer coatings. The highest fracture toughness was observed for the ZrN single-layer, followed by the multilayer coatings and the TiN single-layer, which exhibited the lowest values. This trend of fracture properties can be related to differences in grain size and texture of the investigated coatings. The findings of the present work illuminate the influence of a multilayer architecture of ZrN/TiN coatings on the microstructure and

mechanical properties with a special emphasis on the fracture behaviour, which allows to adapt and optimise these coatings for various applications in the cutting industry.

5.   Acknowledgements

6.   References

[1]   P.F. Becher, Crack Bridging Processes in Toughened Ceramics, Toughening Mech. Quasi-Brittle Mater. (1991) 19–33. https://doi.org/10.1007/978-94-011-3388-3_2.

[2]   R. Daniel, M. Meindlhumer, J. Zalesak, B. Sartory, A. Zeilinger, C. Mitterer, J. Keckes, Fracture toughness enhancement of brittle nanostructured materials by spatial heterogeneity: A micromechanical proof for CrN/Cr and TiN/SiO$_x$ multilayers, Mater. Des. 104 (2016) 227–234. https://doi.org/10.1016/j.matdes.2016.05.029.

[3]   C. Xu, C. Huang, X. Ai, Cutting behavior and related cracks in wear and fracture of ceramic tool materials, Int. J. Adv. Manuf. Technol. 32 (2007) 1083–1089. https://doi.org/10.1007/s00170-006-0431-8.

[4]   R.O. Ritchie, The conflicts between strength and toughness, Nat. Mater. 10 (2011) 817–822. https://doi.org/10.1038/nmat3115.

[5]   R. Daniel, M. Meindlhumer, W. Baumegger, J. Zalesak, B. Sartory, M. Burghammer, C. Mitterer, J. Keckes, Grain boundary design of thin films: Using tilted brittle interfaces for multiple crack deflection toughening, Acta Mater. 122 (2017) 130–137. https://doi.org/10.1016/j.actamat.2016.09.027.

[6]   C. Kainz, N. Schalk, M. Tkadletz, C. Mitterer, C. Czettl, Microstructure and mechanical properties of CVD TiN/TiBN multilayer coatings, Surf. Coatings Technol. 370 (2019) 311–319. https://doi.org/10.1016/j.surfcoat.2019.04.086.

[7]   J.M. González-Carmona, J.D. Triviño, Gómez-Ovalle, C. Ortega, J.M. Alvarado-Orozco, H. Sánchez-Sthepa, A. Avila, Wear mechanisms identification using Kelvin probe force microscopy in TiN, ZrN and TiN/ZrN hard ceramic multilayers coatings, Ceram. Int. 46 (2020) 24592–24604. https://doi.org/10.1016/j.ceramint.2020.06.248.

[8]   Y.X. Xu, L. Chen, F. Pei, K.K. Chang, Y. Du, Effect of the modulation ratio on the interface structure of TiAlN/TiN and TiAlN/ZrN multilayers: First-principles and experimental investigations, Acta Mater. 130 (2017) 281–288. https://doi.org/10.1016/j.actamat.2017.03.053.

[9]   E.J. Herrera-Jimenez, A. Raveh, T. Schmitt, E. Bousser, J.E. Klemberg-Sapieha, L. Martinu, Solid solution hardening in nanolaminate ZrN-TiN coatings with enhanced wear resistance, Thin Solid Films. 688 (2019) 137431. https://doi.org/10.1016/J.TSF.2019.137431.

[10]   X.M. Xu, J. Wang, Q.Y. Zhang, J. An, Y. Zhao, Effect of modulation structure on the growth behavior and mechanical properties of TiN/ZrN multilayers, Surf. Coatings Technol. 201 (2007) 5582–5586. https://doi.org/10.1016/j.surfcoat.2006.07.132.

[11]   L. Geyang, H. Zenghu, T. Jiawan, X. Junhua, G. Mingyuan, Alternating stress field and superhardness effect in TiN/NbN superlattice films, J. Vac. Sci. Technol. A Vacuum, Surfaces, Film. 20 (2002) 674–677. https://doi.org/10.1116/1.1460887.

[12] A.J. Blattner, R. Lakshminarayanan, D.K. Shetty, Toughening of layered ceramic composites with residual surface compression: Effects of layer thickness, Eng. Fract. Mech. 68 (2001) 1–7. https://doi.org/10.1016/S0013-7944(00)00096-5.

[13] C.R. Chen, J. Pascual, F.D. Fischer, O. Kolednik, R. Danzer, Prediction of the fracture toughness of a ceramic multilayer composite - Modeling and experiments, Acta Mater. 55 (2007) 409–421. https://doi.org/10.1016/j.actamat.2006.07.046.

[14] L. Yang, Y. Chen, J. Chen, C. Wang, G. He, Anisotropic deformation and fracture mechanisms of physical vapor deposited TiN/ZrN multilayers, Ceram. Int. 46 (2020) 15502–15509. https://doi.org/10.1016/j.ceramint.2020.03.095.

[15] C. Ziebert, S. Ulrich, Hard multilayer coatings containing TiN and/or ZrN: A review and recent progress in their nanoscale characterization, J. Vac. Sci. Technol. A Vacuum, Surfaces, Film. 24 (2006) 554–583. https://doi.org/10.1116/1.2194031.

[16] S. Zhang, D. Sun, Y. Fu, H. Du, Toughening of hard nanostructural thin films: A critical review, Surf. Coatings Technol. 198 (2005) 2–8. https://doi.org/10.1016/j.surfcoat.2004.10.020.

[17] N. Jäger, S. Klima, H. Hruby, J. Julin, M. Burghammer, J.F. Keckes, C. Mitterer, R. Daniel, Evolution of structure and residual stress of a fcc/hex-AlCrN multi-layered system upon thermal loading revealed by cross-sectional X-ray nano-diffraction, Acta Mater. 162 (2019) 55–66. https://doi.org/10.1016/J.ACTAMAT.2018.09.031.

[18] Y.Y. Wang, M.S. Wong, W.J. Chia, J. Rechner, W.D. Sproul, Synthesis and characterization of highly textured polycrystalline AlN/TiN superlattice coatings, J. Vac. Sci. Technol. A Vacuum, Surfaces, Film. 16 (1998) 3341–3347. https://doi.org/10.1116/1.581542.

[19] Z. Gao, Y. Chen, J. Kulczyk-Malecka, P. Kelly, Y. Zeng, X. Zhang, C. Li, H. Liu, N. Rohbeck, P. Xiao, Comparison of the oxidation behavior of a zirconium nitride coating in water vapor and air at high temperature, Corros. Sci. 138 (2018) 242–251. https://doi.org/10.1016/j.corsci.2018.04.015.

[20] L. Krusin-Elbaum, M. Wittmer, Oxidation kinetics of ZrN thin films, Thin Solid Films. 107 (1983) 111–116. https://doi.org/10.1016/0040-6090(83)90013-5.

[21] I. Milosev, H.-H. Strehblow, B. Navinsek, Comparison of TiN, ZrN, and CrN coatings under oxidation, Thin Solid Films. (1997) 246–254.

[22] C.J. Tavares, L. Rebouta, B. Almeida, J. Bessa E Sousa, Structural characterization of multilayered sputtered TiN/ZrN coatings, Surf. Coatings Technol. 100–101 (1998) 65–71. https://doi.org/10.1016/S0257-8972(97)00589-6.

[23] C.J. Tavares, L. Rebouta, M. Andritschky, S. Ramos, Mechanical characterisation of TiN/ZrN multi-layered coatings, J. Mater. Process. Technol. 92–93 (1999) 177–183. https://doi.org/10.1016/S0924-0136(99)00126-0.

[24] D.F. Arias, Y.C. Arango, A. Devia, Study of TiN and ZrN thin films grown by cathodic arc technique, Appl. Surf. Sci. 253 (2006) 1683–1690. https://doi.org/10.1016/j.apsusc.2006.03.017.

[25] D.F. Arias, Y.C. Arango, A. Devia, Characterization of bilayer coatings of TiN/ZrN grown using pulsed arc PAPVD, Appl. Surf. Sci. 252 (2005) 1175–1181. https://doi.org/10.1016/j.apsusc.2005.02.047.

[26] G. Pradhaban, P. Kuppusami, D. Ramachandran, K. Viswanathan, R. Ramaseshan, Nanomechanical properties of TiN/ZrN multilayers prepared by pulsed laser deposition, Mater. Today Proc. 3 (2016) 1627–1632. https://doi.org/10.1016/j.matpr.2016.04.052.

[27] Indexable inserts for cutting tools - Designation, ISO 1832:2017, 2017. https://standards.iteh.ai/catalog/standards/iso/af10a357-79be-4c54-b963-59800aeb8545/iso-1832-2017.

[28] F. Bachmann, R. Hielscher, H. Schaeben, Texture analysis with MTEX - free and open source software toolbox, Solid State Phenom. 160 (2010) 63–68. https://doi.org/10.4028/www.scientific.net/SSP.160.63.

[29]   R. Hill, The elastic behaviour of a crystalline aggregate, Proc. Phys. Soc. Sect. A. 65 (1952) 349–354. https://doi.org/10.1088/0370-1298/65/5/307.

[30]   V.I. Ivashchenko, P.E.A. Turchi, A. Gonis, L.A. Ivashchenko, P.L. Skrynskii, Electronic origin of elastic properties of titanium carbonitride alloys, Metall. Mater. Trans.   A   Phys.   Metall.   Mater.   Sci.   37   (2006)   3391–3396. https://doi.org/10.1007/s11661-006-1031-9.

[31]   V.I. Ivashchenko, P.E.A. Turchi, V.I. Shevchenko, First-principles study of elastic and stability properties of ZrC-ZrN and ZrC-TiC alloys, J. Phys. Condens. Matter. 21 (2009) 395503. https://doi.org/10.1088/0953-8984/21/39/395503.

[32]   W.C. Oliver, G.M. Pharr, An improved technique for determining hardness and elastic modulus using load and displacement sensing indentation experiments, J. Mater. Res. 7 (1992) 1564–1583. https://doi.org/10.1557/JMR.1992.1564.

[33]   K. Matoy, H. Schönherr, T. Detzel, T. Schöberl, R. Pippan, C. Motz, G. Dehm, A comparative micro-cantilever study of the mechanical behavior of silicon based passivation   films,   Thin   Solid   Films.   518   (2009)   247–256. https://doi.org/10.1016/j.tsf.2009.07.143.

[34]   S. Anders, A. Anders, K.M. Yu, X.Y. Yao, I.G. Brown, On the Macroparticle Flux from Vacuum Arc Cathode Spots, IEEE Trans. Plasma Sci. 21 (1993) 440–446. https://doi.org/10.1109/27.249623.

[35]   A. Anders, Ion charge state distributions of vacuum arc plasmas: The origin of species, Phys. Rev. E. 55 (1997) 969–981. https://doi.org/10.1103/PhysRevE.55.969.

[36]   M. Pohler, R. Franz, J. Ramm, P. Polcik, C. Mitterer, Cathodic arc deposition of $(Al,Cr)_2O_3$: Macroparticles and cathode surface modifications, Surf. Coatings Technol. 206 (2011) 1454–1460. https://doi.org/10.1016/j.surfcoat.2011.09.028.

[37]   V. V. Uglov, V.M. Anishchik, S. V. Zlotski, G. Abadias, S.N. Dub, Structural and mechanical stability upon annealing of arc-deposited Ti-Zr-N coatings, Surf.

Coatings Technol. 202 (2008) 2394–2398. https://doi.org/10.1016/j.surfcoat.2007.09.035.

[38] S. Gates-Rector, T. Blanton, The Powder Diffraction File: A quality materials characterization database, Powder Diffr. 34 (2019) 352–360. https://doi.org/10.1017/S0885715619000812.

[39] P.J. Brown, A.G. Fox, E.N. Maslen, M.A. O'Keefe, B.T.M. Willis, Intensity of diffracted intensities, in: Int. Tables Crystallogr., Wiley, Chichester, 2006: pp. 554–595. https://doi.org/10.1107/97809553602060000600.

[40] E.W. Niu, G.H. Lv, W.R. Feng, S.H. Fan, X.Z. Yang, S.Z. Yang, L. Li, H. Chen, Influence of substrate bias on the structure and properties of ZrN films deposited by cathodic vacuum arc, Mater. Sci. Eng. A. 460–461 (2007) 135–139. https://doi.org/10.1016/j.msea.2007.02.085.

[41] H.M. Tung, J.H. Huang, D.G. Tsai, C.F. Ai, G.P. Yu, Hardness and residual stress in nanocrystalline ZrN films: Effect of bias voltage and heat treatment, Mater. Sci. Eng. A. 500 (2009) 104–108. https://doi.org/10.1016/j.msea.2008.09.006.

[42] Y.O. Kravchenko, E. Coy, B. Peplińska, I. Iatsunskyi, K. Załęski, M. Kempiǹski, V.M. Beresnev, A. V. Pshyk, A.D. Pogrebnjak, Micro-mechanical investigation of $(Al_{50}Ti_{50})N$ coatings enhanced by ZrN layers in the nanolaminate architecture, Appl. Surf. Sci. 534 (2020). https://doi.org/10.1016/j.apsusc.2020.147573.

[43] G. Abadias, Y.Y. Tse, P. Guérin, V. Pelosin, Interdependence between stress, preferred orientation, and surface morphology of nanocrystalline TiN thin films deposited by dual ion beam sputtering, J. Appl. Phys. 99 (2006) 113519. https://doi.org/10.1063/1.2197287.

[44] I. Petrov, P.B. Barna, L. Hultman, J.E. Greene, Microstructural evolution during film growth, J. Vac. Sci. Technol. A Vacuum, Surfaces, Film. 21 (2003) S117–S128. https://doi.org/10.1116/1.1601610.

[45] Y. Moritz, C. Kainz, M. Tkadletz, C. Czettl, M. Pohler, N. Schalk, Microstructure and mechanical properties of arc evaporated Ti(Al,Si)N coatings, Surf. Coatings Technol. 421 (2021) 127461. https://doi.org/10.1016/j.surfcoat.2021.127461.

[46] C. Kainz, M. Pohler, G.C. Gruber, M. Tkadletz, A. Sophie, C. Czettl, N. Schalk, Influence of bias voltage on microstructure, mechanical properties and thermal stability of arc evaporated $Cr_{0.74}Ta_{0.26}N$ coatings, Surf. Coatings Technol. 417 (2021) 127212. https://doi.org/10.1016/j.surfcoat.2021.127212.

[47] Y. Kim, Y. Cho, S. Hong, S. Bühlmann, H. Park, D.K. Min, S.H. Kim, K. No, Correlation between grain size and domain size distributions in ferroelectric media for probe storage applications, Appl. Phys. Lett. 89 (2006). https://doi.org/10.1063/1.2363942.

[48] W. Cao, C.A. Randall, Grain size and domain size relations in bulk ceramic ferroelectric materials, J. Phys. Chem. Solids. 57 (1996) 1499–1505. https://doi.org/10.1016/0022-3697(96)00019-4.

[49] R. Daniel, J. Keckes, I. Matko, M. Burghammer, C. Mitterer, Origins of microstructure and stress gradients in nanocrystalline thin films: The role of growth parameters and self-organization, Acta Mater. 61 (2013) 6255–6266. https://doi.org/10.1016/j.actamat.2013.07.009.

[50] S.J. Bull, A.M. Jones, Multilayer coatings for improved performance, Surf. Coatings Technol. 78 (1996) 173–184. https://doi.org/10.1016/0257-8972(94)02407-3.

[51] M. Stueber, H. Holleck, H. Leiste, K. Seemann, S. Ulrich, C. Ziebert, Concepts for the design of advanced nanoscale PVD multilayer protective thin films, J. Alloys Compd. 483 (2009) 321–333. https://doi.org/10.1016/j.jallcom.2008.08.133.

[52] Z.T.Y. Liu, B.P. Burton, S. V. Khare, D. Gall, First-principles phase diagram calculations for the rocksalt-structure quasibinary systems TiN-ZrN, TiN-HfN and ZrN-HfN, J. Phys. Condens. Matter. 29 (2017) 35401. https://doi.org/10.1088/0953-8984/29/3/035401.

[53] Z.B. Qi, P. Sun, F.P. Zhu, Z.C. Wang, D.L. Peng, C.H. Wu, The inverse Hall-Petch effect in nanocrystalline ZrN coatings, Surf. Coatings Technol. 205 (2011) 3692–3697. https://doi.org/10.1016/j.surfcoat.2011.01.021.

[54] H. Ljungcrantz, M. Odén, L. Hultman, J.E. Greene, J.E. Sundgren, Nanoindentation studies of single-crystal (001)-, (011)-, and (111)-oriented TiN layers on MgO, J. Appl. Phys. 80 (1996) 6725–6733. https://doi.org/10.1063/1.363799.

[55] Z.G. Mei, S. Bhattacharya, A.M. Yacout, First-principles study of fracture toughness enhancement in transition metal nitrides, Surf. Coatings Technol. 357 (2019) 903–909. https://doi.org/10.1016/j.surfcoat.2018.10.102.

[56] M. Bielawski, K. Chen, Computational evaluation of adhesion and mechanical properties of nanolayered erosion-resistant coatings for gas turbines, J. Eng. Gas Turbines Power. 133 (2011) 042102–1. https://doi.org/10.1115/1.4002158.

[57] G. Abadias, V.I. Ivashchenko, L. Belliard, P. Djemia, Structure, phase stability and elastic properties in the $Ti_{1-x}Zr_xN$ thin-film system: Experimental and computational studies, Acta Mater. 60 (2012) 5601–5614. https://doi.org/10.1016/j.actamat.2012.07.014.

[58] A. Hoerling, J. Sjölén, H. Willmann, T. Larsson, M. Odén, L. Hultman, Thermal stability, microstructure and mechanical properties of $Ti_{1-x}Zr_xN$ thin films, Thin Solid Films. 516 (2008) 6421–6431. https://doi.org/10.1016/j.tsf.2007.12.133.

[59] V. Krasnenko, M.G. Brik, First-principles calculations of the structural, elastic and electronic properties of MN_xC_{1-x} (M = Ti, Zr, Hf; $0 \leq x \leq 1$) carbonitrides at ambient and elevated hydrostatic pressure, Solid State Sci. 28 (2014) 1–8. https://doi.org/10.1016/j.solidstatesciences.2013.11.012.

[60] J.H. Huang, Y.H. Chen, A.N. Wang, G.P. Yu, H. Chen, Evaluation of fracture toughness of ZrN hard coatings by internal energy induced cracking method, Surf. Coatings Technol. 258 (2014) 211–218. https://doi.org/10.1016/j.surfcoat.2014.09.026.

[61] H.W. Hsiao, J.H. Huang, G.P. Yu, Effect of oxygen on fracture toughness of Zr(N,O) hard coatings, Surf. Coatings Technol. 304 (2016) 330–339. https://doi.org/10.1016/j.surfcoat.2016.07.026.

[62] A.N. Wang, G.P. Yu, J.H. Huang, Fracture toughness measurement on TiN hard coatings using internal energy induced cracking, Surf. Coatings Technol. 239 (2014) 20–27. https://doi.org/10.1016/j.surfcoat.2013.11.010.

[63] M. Bartosik, R. Hahn, Z.L. Zhang, I. Ivanov, M. Arndt, P. Polcik, P.H. Mayrhofer, Fracture toughness of Ti-Si-N thin films, Int. J. Refract. Met. Hard Mater. 72 (2018) 78–82. https://doi.org/10.1016/j.ijrmhm.2017.12.015.

[64] C. Kainz, N. Schalk, M. Tkadletz, C. Mitterer, C. Czettl, The effect of B and C addition on microstructure and mechanical properties of TiN hard coatings grown by chemical vapor deposition, Thin Solid Films. (2019) 1–8. https://doi.org/10.1016/j.tsf.2019.05.002.

[65] S. Kataria, S.K. Srivastava, P. Kumar, G. Srinivas, Siju, J. Khan, D.V.S. Rao, H.C. Barshilia, Nanocrystalline TiN coatings with improved toughness deposited by pulsing the nitrogen flow rate, Surf. Coatings Technol. 206 (2012) 4279–4286. https://doi.org/10.1016/j.surfcoat.2012.04.040.

[66] S. Massl, W. Thomma, J. Keckes, R. Pippan, Investigation of fracture properties of magnetron-sputtered TiN films by means of a FIB-based cantilever bending technique, Acta Mater. 57 (2009) 1768–1776. https://doi.org/10.1016/j.actamat.2008.12.018.

[67] S.W. Freiman, P.L. Swanson, Fracture of polycrystalline ceramics, in: Deform. Process. Miner. Ceram. Rocks, vol. 1, Springer, Dordrecht, 1990: pp. 72–83. https://doi.org/10.1007/978-94-011-6827-4_4.

[68] C. Kainz, M. Pohler, M. Tkadletz, C. Czettl, N. Schalk, The influence of bias voltage on structure, thermal stability and mechanical properties of arc evaporated

$Cr_{0.69}Ta_{0.20}B_{0.11}N$ coatings, Surf. Coatings Technol. 428 (2021) 127867. https://doi.org/10.1016/j.surfcoat.2021.127867.

Publication IV

Investigation of the microstructure of a graded ZrN/Ti$_{0.33}$Al$_{0.67}$N multilayer coating using cross-sectional characterization methods

Florian Frank, Michael Tkadletz, Christian Saringer, Christoph Czettl, Markus Pohler, Manfred Burghammer, Juraj Todt, Jakub Zalesak, Jozef Keckes, Nina Schalk

Investigation of the microstructure of a graded ZrN/Ti$_{0.33}$Al$_{0.67}$N multilayer coating using cross-sectional characterization methods

Florian Frank[1], Michael Tkadletz[2], Christian Saringer[1], Christoph Czettl[3], Markus Pohler[3], Manfred Burghammer[4], Juraj Todt[2,5], Jakub Zalesak[2,5], Jozef Keckes[2,5], Nina Schalk[1]

[1] Christian Doppler Laboratory for Advanced Coated Cutting Tools at the Department of Materials Science, Montanuniversität Leoben, Franz–Josef–Strasse 18, 8700 Leoben, Austria

[2] Department of Materials Science, Montanuniversität Leoben, Franz–Josef–Strasse 18, 8700 Leoben, Austria

[3] Ceratizit Austria GmbH, Metallwerk–Plansee–Strasse 71, 6600 Reutte, Austria

[4] European Synchrotron Radiation Facility, Cedex 9, 38043 Grenoble, France

[5] Erich Schmid Institute for Materials Science, Austrian Academy of Sciences, Leoben, Austria

Abstract

An approach to enhance the performance of protective hard coatings for cutting applications is to modify the coating architecture by combining two inherently different materials in a multilayer. Besides the choice of the materials, the thickness of the individual layers strongly influences the coating microstructure and consequently also its properties. Within this work, a graded ZrN/Ti$_{0.33}$Al$_{0.67}$N multilayer coating with constant Ti$_{0.33}$Al$_{0.67}$N and stepwise increasing ZrN layer thickness was investigated in detail by a combinatorial approach of cross-sectional X-ray nanodiffraction, electron backscatter diffraction and transmission electron microscopy. The primary aim was to obtain a profound understanding of the microstructure of the coating as well as of the residual

stress state. (Semi-)coherent grain growth was observed independently of the ZrN layer thickness. Changes in the multilayer architecture were found to affect not only the grain size, but also the residual stress state of the coating. While the grain size increased with increasing ZrN layer thickness, the residual stress decreased. This work contributes to a deeper understanding of the influence of the multilayer architecture on the microstructure and stress state of heteroepitactic multilayer coatings.

Keywords: X-ray nanodiffraction, residual stress, multilayers, ZrN, TiAlN, hard coatings, arc evaporation

1.   Introduction

Multilayer coatings with two or more alternating layer materials have been reported to show superior machining performance compared to their single-layer counterparts [1,2]. There, not only the materials used for the multilayer coatings, but also the layer architecture significantly influences the properties [3,7]. The improved mechanical and thermal properties of cathodic arc evaporated (CAE) ZrN/TiAlN multilayer coatings, compared to their single-layer counterparts, can be attributed to the coherency between the ZrN and TiAlN layers, as well as alterations in grain size, texture and interface density, depending on the bilayer period [5,7–9]. Xu et al. observed a correlation between higher hardness and coherency as a result of alternating stress fields of the two coherently grown materials with different lattice parameters, an effect that was also observed by other researchers for multilayer coatings with different layer materials [5,6,10–12]. However, not only the lattice parameters of the different materials, but also the thickness of the individual layers were reported to affect the coherency and thus the stress state of the coating [5]. In order to optimize the multilayer architecture, detailed knowledge about the residual stress state is of significant importance, as e.g. high stresses can lead to coating failure due to delamination and plastic deformation, especially at high

thermal or mechanical loads [9,13]. Also, microstructural gradients can form within the individual layers of a multilayer coating, affecting the functional properties of the coating also on a macroscopic level [14]. Although the influence of the bilayer period of ZrN/TiAlN multilayer coatings on the coherency and the mechanical properties has already been investigated [5,7–9], a detailed study is still missing, of how the individual layer thickness affects the stress state of both layers, as well as a detailed investigation of microstructural gradients that form during coating synthesis.

Thus, within this work a graded $ZrN/Ti_{0.33}Al_{0.67}N$ multilayer coating was synthesized, with from the substrate towards to surface gradually increasing ZrN sublayer and constant $Ti_{0.33}Al_{0.67}N$ sublayer thickness. Starting with a $ZrN:Ti_{0.33}Al_{0.67}N$ thickness ratio <1 at the interface to the substrate, the thickness ratio was gradually increased to >1 towards the surface and the effect on coherency, as well as the grain size and the stress state were investigated in detail. The complementary application of different investigation methods allowed to evaluate the microstructure and stress state on different length scales, starting on a macroscopic level, using laboratory X-ray diffraction (XRD), scanning electron microscopy (SEM) and electron backscatter diffraction (EBSD). Cross-sectional X-ray nanodiffraction (CSnanoXRD) was applied to study gradients in phase composition, residual stress, as well as crystallographic texture depth-resolved across the coating thickness with a local resolution of ~50 nm [14–19]. Furthermore, transmission electron microscopy (TEM) and energy dispersive X-ray spectroscopy (EDS) were applied.

2. Experimental details

2.1. Coating deposition

A graded $ZrN/Ti_{0.33}Al_{0.67}N$ multilayer coating, with constant $Ti_{0.33}Al_{0.67}N$ layer thickness and increasing ZrN layer thickness, was deposited using a commercially available CAE deposition chamber by Oerlikon Balzers, using two Zr and four $Ti_{0.33}Al_{0.67}$ targets. Cemented carbide cutting inserts in SNUN 120412 geometry (ISO 1832 [20]) with

a composition of 92 wt.% WC, 6 wt.% Co and 2 wt.% mixed carbides served as substrate material. The substrates were mounted on a rotational substrate holder, enabling two-fold rotation of the substrates during deposition. The bias voltage and the temperature were kept constant at -40 V and 425 °C, respectively. A mixture of N_2 and Ar was used to synthesize the nitride multilayer coating. A schematic of the architecture of the graded ZrN/$Ti_{0.33}Al_{0.67}N$ coating is displayed in Fig. 1a. A $Ti_{0.33}Al_{0.67}N$ base layer was deposited on the substrate before the deposition of the multilayer blocks, followed by nine blocks of different ZrN/$Ti_{0.33}Al_{0.67}N$ bilayer thickness. Within each block, the layer thickness ratio was kept constant and the total block thickness was designed to lie between 400-600 nm. In blocks 1-4, the multilayers were formed due to the rotation of the substrates. As the ZrN layer thickness that can be achieved is limited by the maximum applied current to the Zr targets, blocks 5-9 with ZrN layer thickness >24 nm were deposited by opposed cyclic activation and deactivation of the Zr and TiAl targets, while maintaining the substrate rotation. The ZrN layer thickness was controlled by increasing the working time of the Zr target for each successive block. To guarantee an almost constant thickness of the individual $Ti_{0.33}Al_{0.67}N$ layers of 13-17 nm, the TiAl target working time was kept constant throughout the deposition process. In addition to the graded ZrN/$Ti_{0.33}Al_{0.67}N$ multilayer coating, ZrN and $Ti_{0.33}Al_{0.67}N$ single-layer coatings were deposited from the same targets and at the same deposition conditions as the multilayer coating. The single-layer coatings were deposited on cemented carbide substrates and mild steel foils.

2.2. *Coating characterization*

The coated mild steel foils were dissolved in nitric acid to obtain a coating powder, which was used to determine the unstrained lattice parameter of ZrN and $Ti_{0.33}Al_{0.67}N$ single-layer coatings without the influence of the substrate material. Furthermore, the elemental composition of the single-layer coatings was investigated by glow discharge optical emission spectroscopy (GDOES) using a Horiba GD-Profiler 2 spectrometer.

A Hitachi IM4000+ ion milling system was used to prepare a cross-section of the ZrN/Ti$_{0.33}$Al$_{0.67}$N multilayer coating, which was investigated using a Zeiss GeminiSEM 450. The EBSD analysis was conducted in the same SEM with an accelerating voltage of 10 kV and a step size of 20 nm, utilizing an Oxford Symmetry EBSD camera.

An FEI Helios NanoLab 660 workstation was used to prepare a thin lamella of the cross-section of the coating for the TEM investigations. The lamella was thinned down to an electron-transparent thickness using accelerating voltages from 30 to 2 kV and ion currents ranging from 20 nA to 40 pA. TEM investigations were performed on an FEI Titan Themis system, operated at 300 kV in scanning TEM (STEM) mode, using a probe current of 1 nA. EDS was conducted applying an FEI SUPER-X spectrometer with 4x30mm^2 windowless silicon drift detectors (SDD).

The phase composition of the coating was investigated using a Bruker D8 Advance diffractometer with a Cu-Kα source (λ = 0.15406 nm) and an energy-dispersive Sol-X detector. A detailed investigation of the residual stress, texture and the unstrained lattice parameter was conducted on a Bruker D8 Advance DaVinci diffractometer using Cu-Kα radiation and a position sensitive LynxEye XE-T detector. The residual stress was determined using the ZrN 200 and Ti$_{0.33}$Al$_{0.67}$N 200 peaks employing the sin$^2\psi$ method in side-inclination mode with tilt angles ψ between 0-82° and X-ray elastic constants $\frac{1}{2}s_2^{hkl}$, as described at the end of this section. XRD pole figures (PFs) were recorded for the 111, 200 and 220 reflections of the fcc-ZrN and fcc-Ti$_{0.33}$Al$_{0.67}$N phase with tilt angles from 0-84°. To determine a reference unstrained lattice parameter, X-ray diffractograms of powdered single-layer ZrN and Ti$_{0.33}$Al$_{0.67}$N coatings were recorded in Bragg-Brentano geometry and evaluated applying a Pawley-refinement using the software Topas 6.

In order to enable the CSnanoXRD experiments, a 150 μm thick lamella of the substrate/coating compound was cut out using a diamond cutting wheel, mounted on a Struers Accutom-5R precision saw, and further thinned down to a thickness of ~45 μm using focused ion beam (FIB) milling. CSnanoXRD experiments were performed at the

nanofocus extension of the ID13 beamline at the European Synchrotron Radiation Facility (ESRF) in Grenoble, France [14]. The raw data can be found under ref. [21]. The monochromatic X-ray beam with a photon energy of 13 keV and a point focus with a diameter of ~50 nm was directed at the lamella parallel to the sample surface. The cross-section of the sample was scanned along the substrate normal direction in transmission geometry by moving the sample through the beam with a step size of 25 nm. For each scan step, a two-dimensional diffraction pattern was recorded using a Dectris Eiger X 4M detector. The patterns were evaluated using the pyFAI software package [22,23]. The in-plane residual strain ε^{hkl} and in-plane stress σ^{hkl} for the ZrN and $Ti_{0.33}Al_{0.67}N$ 200 diffraction peaks were evaluated using the method described in refs. [15,24]. For this, each ring, resulting from the diffraction on {200} lattice planes of the ZrN or $Ti_{0.33}Al_{0.67}N$ phase, was divided into 36 equal segments of 10° that were integrated and the resulting peaks were fitted using a pseudo-Voigt function to determine the d-spacing as a function of the azimuthal orientation [14,15,24]. According to refs. [17,24,25], additionally, the stress-free d-spacing (d_0^{hkl}) was evaluated using the Poisson's ratio ν^{hkl}. The stress-free lattice parameter (a_0) was then calculated from d_0^{hkl}. The X-ray elastic constants $\frac{1}{2}s_2^{hkl}$ and ν^{hkl} needed to calculate σ^{hkl} were determined using the Hill grain interaction model [26], employing single-crystal elastic constants from literature as input [27,28]. For the 200 reflection, $\frac{1}{2}s_2^{200} = 2.74 \cdot 10^{-12}\,Pa^{-1}$ and $\nu^{200} = 0.207$ were calculated for fcc-ZrN and $\frac{1}{2}s_2^{200} = 3.03 \cdot 10^{-12}\,Pa^{-1}$ and $\nu^{200} = 0.234$ for fcc-$Ti_{0.33}Al_{0.67}N$.

3. Results

3.1. Architecture, microstructure and elemental composition

In Fig. 1a, the architecture of the ZrN/$Ti_{0.33}Al_{0.67}N$ multilayer coating is schematically shown. The 9 blocks are numbered in ascending order, starting from the $Ti_{0.33}Al_{0.67}N$ base layer. The ZrN layer thickness is constant within the respective blocks, but increases with increasing block number, while the $Ti_{0.33}Al_{0.67}N$ layer thickness is

constant over the whole coating thickness. For each block the individual layer thicknesses are given in Fig. 1a. In the SEM image in Fig. 1b, the ZrN and $Ti_{0.33}Al_{0.67}N$ layers are clearly distinguishable due to their differences in the elemental contrast, where brighter layers correspond to ZrN and darker ones to $Ti_{0.33}Al_{0.67}N$. The EBSD band contrast image in Fig. 1c shows that grain growth is not interrupted by the $ZrN/Ti_{0.33}Al_{0.67}N$ interfaces, leading to the assumption that the individual layers grow coherently or semi-coherently. Even at smaller bilayer thicknesses in blocks 1-3 the grains are larger than the single layers. The influence of the bilayer thickness on the grain size is also visible; it can be seen that the grain size increases with the bilayer thickness. Especially in blocks 5-9 a gradual increase of the grain size with the bilayer thickness can be observed. In the EBSD inverse pole figure (IPF) map in growth direction (Y-direction), shown in Fig. 1d, the grain orientation is displayed. In blocks 1-4 only a small number of grains with a sufficiently large grain size can be indexed, making an estimation of the grain orientation with this method impossible. However, larger grains from block 5 towards the surface display a tendency towards a <100> out-of-plane preferred orientation, although the texture is not that pronounced. All indexed grains exhibited a face-centered cubic (fcc) crystal structure.
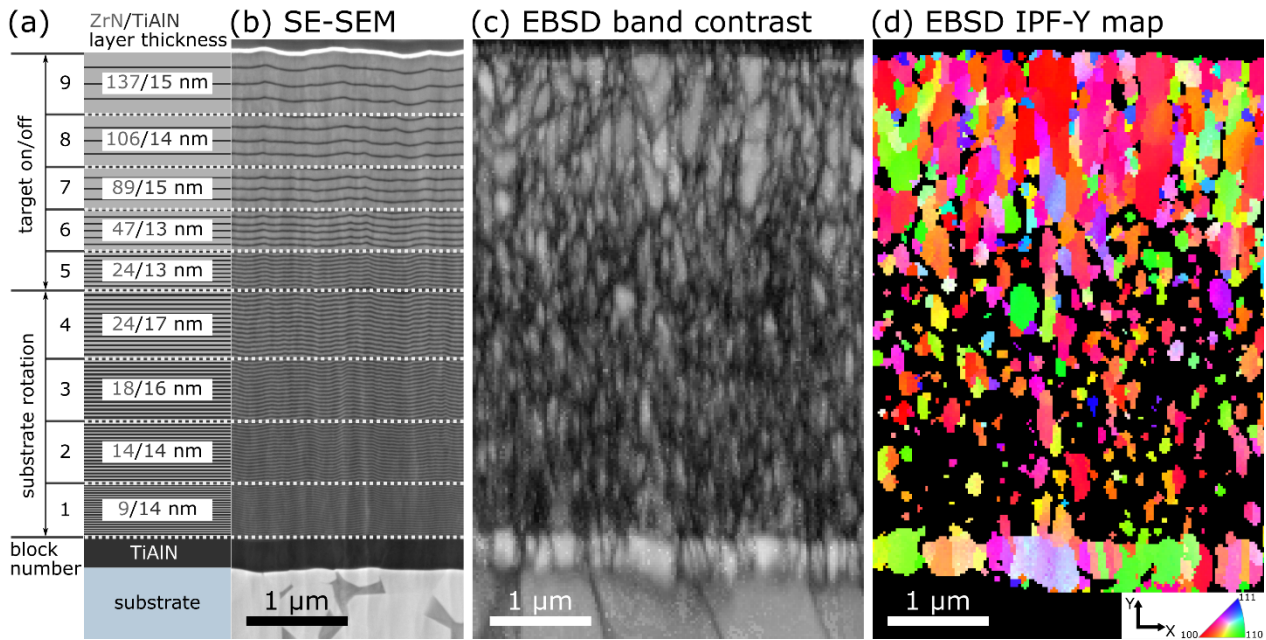
Fig. 1: (a) Schematic sketch of the graded coating architecture and (b) secondary electron SEM (SE-SEM) image of the FIB prepared cross-section of the graded ZrN/Ti$_{0.33}$Al$_{0.67}$N coating. (c) EBSD band contrast image displaying the grains and (d) EBSD inverse pole figure (IPF) map in growth direction showing the grain orientation.

The TEM micrographs in Fig. 2a and b show an overview of the cross-section of the coating. At the interface between blocks 4 and 5, the Ti$_{0.33}$Al$_{0.67}$N layer appears thicker than the other Ti$_{0.33}$Al$_{0.67}$N layers. This can be related to the change in deposition mode from substrate rotation to target on/off. In the annular dark-field (ADF) image it can be seen that the grain size increases in blocks 1-9 and complex variations of the contrast in the image might indicate dislocations along the cross-section. Due to the high elemental contrast (Z-contrast) in the high-angle ADF (HAADF) image, the brighter ZrN and darker Ti$_{0.33}$Al$_{0.67}$N are clearly visible and seem to be well separated. EDS maps show a clear distinction between the Zr in the ZrN layers and the Ti and Al in the Ti$_{0.33}$Al$_{0.67}$N layers. Although the N content appears homogeneous for blocks 1-5, it seems to increase in the Ti$_{0.33}$Al$_{0.67}$N layers and decrease in the ZrN layers in blocks 6-9, where the ZrN layer thickness is significantly larger than the Ti$_{0.33}$Al$_{0.67}$N layer thickness. This effect can be attributed to an overestimation of the N content in Ti$_{0.33}$Al$_{0.67}$N layers, due to the vicinity

of the Ti-Lα and N-Kα lines in the EDS spectrum [3]. In order to quantify the chemical composition, GDOES investigations of the single-layer ZrN and $Ti_{0.33}Al_{0.67}N$ coatings, which were deposited under the same conditions as the ZrN/$Ti_{0.33}Al_{0.67}N$ multilayer coating, were conducted and revealed a N content of ~50 at.% for both, the ZrN and the $Ti_{0.33}Al_{0.67}N$ coating. The Ti and Al content of the $Ti_{0.33}Al_{0.67}N$ coating were ~16 at.% and ~33 at.%, respectively. These findings show that the coatings were stoichiometric regarding their metal/non-metal ratio and that the Ti:Al ratio in the coating matches well with the Ti:Al ratio of the target, which can also be assumed for the multilayer coatings.
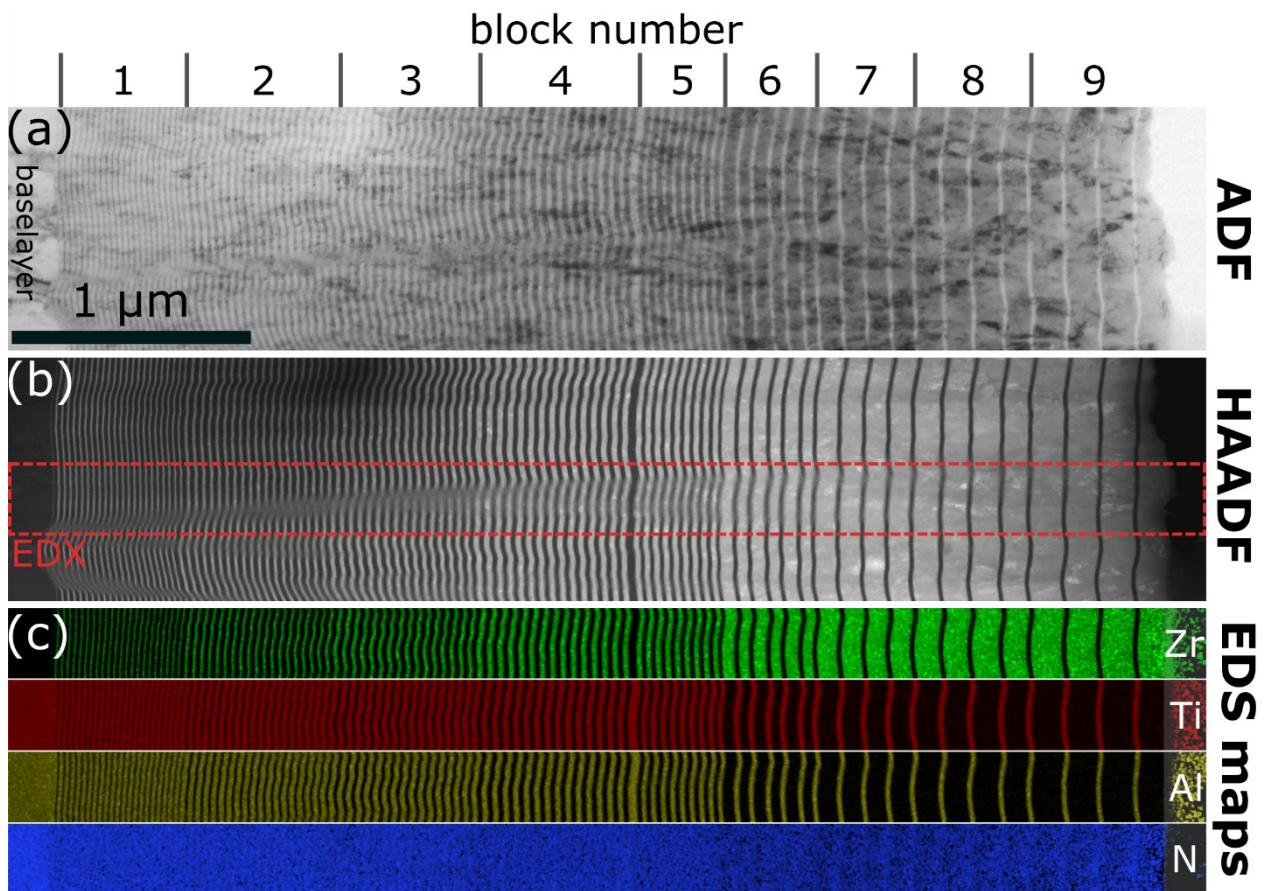

Fig. 2: (a) ADF and (b) HAADF images of the ZrN/$Ti_{0.33}Al_{0.67}N$ cross-section. (c) The EDS maps display Zr, Ti, Al and N and were recorded from the region highlighted in the HAADF image.

The X-ray diffractogram in Fig. 3a indicates an fcc structure for both, ZrN and $Ti_{0.33}Al_{0.67}N$ phases. While several distinct ZrN peaks are visible, only the $Ti_{0.33}Al_{0.67}N$ 200

peak can be observed clearly. This can be related to the smaller diffracting volume of the thinner $Ti_{0.33}Al_{0.67}N$ layers compared to thicker ZrN layers and to the higher atomic form factor of Zr compared to Ti and Al, which leads to a more intense signal from ZrN than from $Ti_{0.33}Al_{0.67}N$ [29]. The $Ti_{0.33}Al_{0.67}N$ 200 peak is situated between the reference positions for fcc-TiN and fcc-AlN, indicating the formation of a $Ti_{0.33}Al_{0.67}N$ solid solution. Also for ZrN the most pronounced peak is the 200 peak, suggesting a <100> preferred orientation. The additionally recorded XRD pole figures of the ZrN (Fig. 3b) and $Ti_{0.33}Al_{0.67}N$ (Fig. 3c) 111, 200 and 220 peaks corroborate a strong <100> fiber texture for both phases. The texture seems aligned for both phases, confirming the coherent or semi-coherent layer growth. However, no conclusions can be drawn as to whether the variation of the individual layer thickness as a function of the coating thickness leads to a change in preferred orientation of the crystallites.
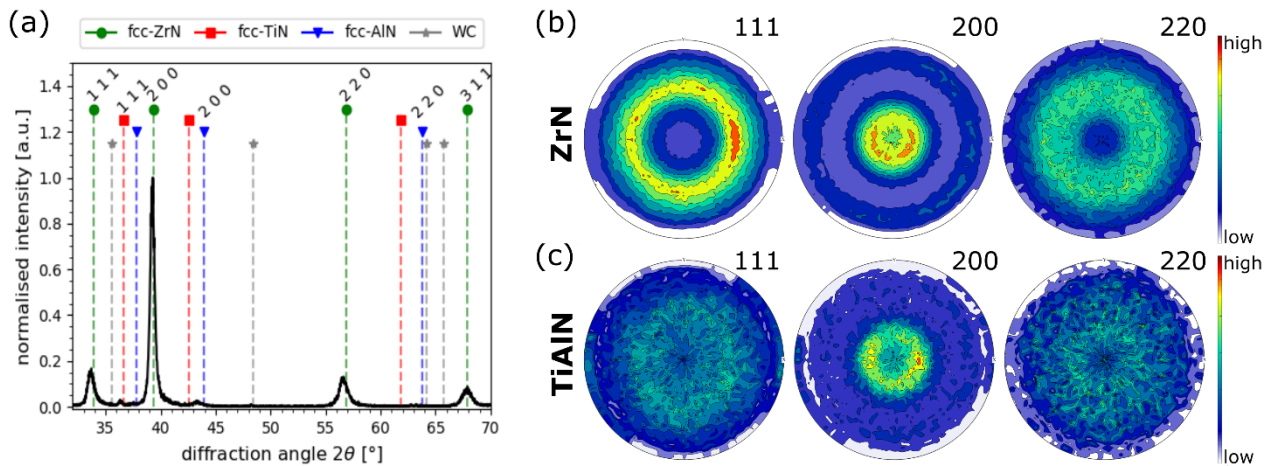

Fig. 3: (a) X-ray diffractogram of the ZrN/Ti₀.₃₃Al₀.₆₇N multilayer coating. The reference positions for fcc-ZrN (PDF 00-035-0753), fcc-TiN (PDF 00-038-1420), fcc-AlN (PDF 00-025-1495) and WC from the substrate (PDF 00-003-1096) are indicated with dashed lines [30]. XRD pole-figures of the (b) ZrN and (c) TiAlN 111, 200 and 220 peaks.

3.2. CSnanoXRD analysis

To investigate the effect of the layer architecture on the microstructure of the $ZrN/Ti_{0.33}Al_{0.67}N$ multilayer coating, position-resolved CSnanoXRD investigations as a

function of the film thickness were conducted. In Fig. 4a, the phase evolution along the cross-section is displayed. For this, the two-dimensional Debye-Scherrer rings were integrated azimuthally in the range of 0-360° and the resulting radial XRD patterns are plotted for each measured position along the cross-section. It can be seen that the phase composition does not change with increasing ZrN layer thickness and blocks 1-9 show an fcc structure for both, ZrN and $Ti_{0.33}Al_{0.67}N$ phases. Besides the phase composition, CSnanoXRD allows to investigate the crystallographic texture of the coating. In Fig. 4b, the out-of-plane component of the Debye-Scherrer rings is shown. The intensity of the ZrN 200 peak is the highest and the intensities of the different peaks do not change with respect to each other over the whole coating thickness, indicating that <100> is the preferred crystal orientation, independent of the bilayer thickness. Analogously, $Ti_{0.33}Al_{0.67}N$ also displays a <100> preferred orientation over the whole coating thickness.

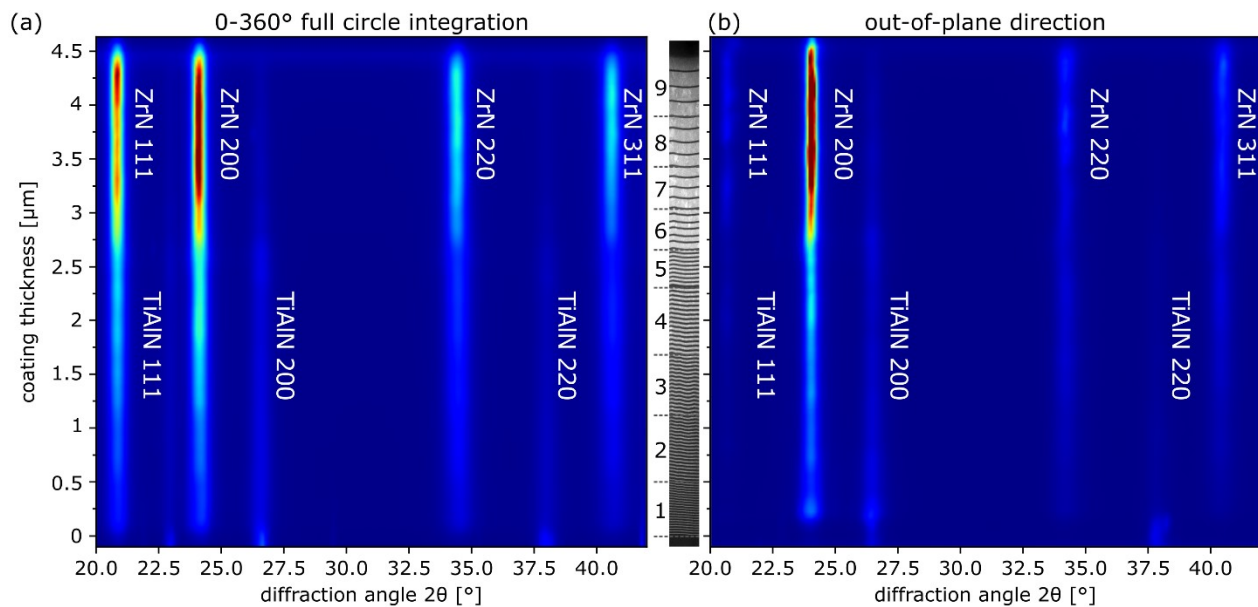*Fig. 4: (a) Phase plot of the $ZrN/Ti_{0.33}Al_{0.67}N$ multilayer coating for a full circle (0-360°) integration of the Debye-Scherrer related to a STEM HAADF image and indicated blocks as reference for the coating architecture. (b) Phase plot in out-of-plane direction (integration range out-of-plane direction ± 5°).*

In addition to the phase composition and the texture, the in-plane biaxial X-ray elastic strain and residual stress state of the ZrN and $Ti_{0.33}Al_{0.67}N$ phases were determined from the distortion of Debye-Scherrer rings and are presented in Fig. 5a and b. The in-plane elastic strain in Fig. 5a is directly determined from the distorted Debye-Scherrer rings and only ν is required for the calculation, while for the in-plane residual stress the X-ray elastic constants are needed [14,15]. For simplicity it was assumed that both, ν and the X-ray elastic constants do not change along the cross-section [14,15,17]. It can be seen that the trends in elastic strain and residual stress are comparable. Thus, the discussion focuses on the evolution of the residual stress.

The average residual strain and stress of the multilayer coating including the standard deviation, obtained by laboratory XRD and the $\sin^2\psi$ method, is also added to Fig. 5a and b, respectively. The considerably higher standard deviation of $Ti_{0.33}Al_{0.67}N$ compared to ZrN can be related to the weaker diffraction intensity of $Ti_{0.33}Al_{0.67}N$ peaks. It can be seen that the average stress correlates well with the apparent mean stress over the whole coating thickness determined from the CSnanoXRD analysis for both, ZrN and $Ti_{0.33}Al_{0.67}N$. Independent of the layer thickness, a compressive residual stress state is observed over the whole coating thickness for ZrN and $Ti_{0.33}Al_{0.67}N$. A trend can be observed, where the residual stress decreases in blocks 1-9 for both phases. The highest stress is observed in the vicinity of the base layer in blocks 1 and 2 and is approximately −5 and −3.5 GPa for ZrN and $Ti_{0.33}Al_{0.67}N$, respectively. The difference between ZrN and $Ti_{0.33}Al_{0.67}N$ diminishes gradually with increasing coating thickness, as the residual stress drops faster in the ZrN than in $Ti_{0.33}Al_{0.67}N$ layers. In blocks 6-9 the stresses are roughly equal for both layers and further decrease towards the surface. In block 5, the residual stress in the ZrN layer rises by ~1 GPa, which is most probably related to the change in the deposition mode from substrate rotation to target on/off.

In Fig. 5c the stress-free lattice parameter a_0 evaluated from the ZrN and $Ti_{0.33}Al_{0.67}N$ 200 peaks, is displayed with respect to the coating thickness. In addition, the

reference positions of the unstrained lattice parameter are shown, determined from the powders of the ZrN and Ti$_{0.33}$Al$_{0.67}$N single-layer coatings, which are 4.58 Å and 4.16 Å, respectively. The Ti$_{0.33}$Al$_{0.67}$N a_0 does not change significantly over the coating thickness and is in good agreement with the a_0 of the single-layer coating. The ZrN a_0 displays minor deviations from the reference a_0 over the whole coating thickness, which are more pronounced in the surface and base layer near regions.

The evaluation of the full-width at half maximum of the 200 diffraction peaks ($fwhm^{200}$), determined from the 360°-integrated Debye-Scherrer rings, allows to draw conclusions on the size of the coherently diffracting domains, which correlates with the grain size [31–34], and the density of structural defects such as dislocations that induce stresses of second and third order. In Fig. 5d, the $fwhm^{200}$ for ZrN and Ti$_{0.33}$Al$_{0.67}$N are shown with respect to the coating thickness. Both phases show a decreasing $fwhm^{200}$ with increasing coating thickness up to the surface-near region in block 9. For Ti$_{0.33}$Al$_{0.67}$N, only a minor $fwhm^{200}$ decrease with increasing coating thickness is observed. For blocks 7-9, the $fwhm^{200}$ error increases in the Ti$_{0.33}$Al$_{0.67}$N layers, which can be attributed to a decreasing relative volume of the Ti$_{0.33}$Al$_{0.67}$N layers compared to the increasing volume of the ZrN layers.
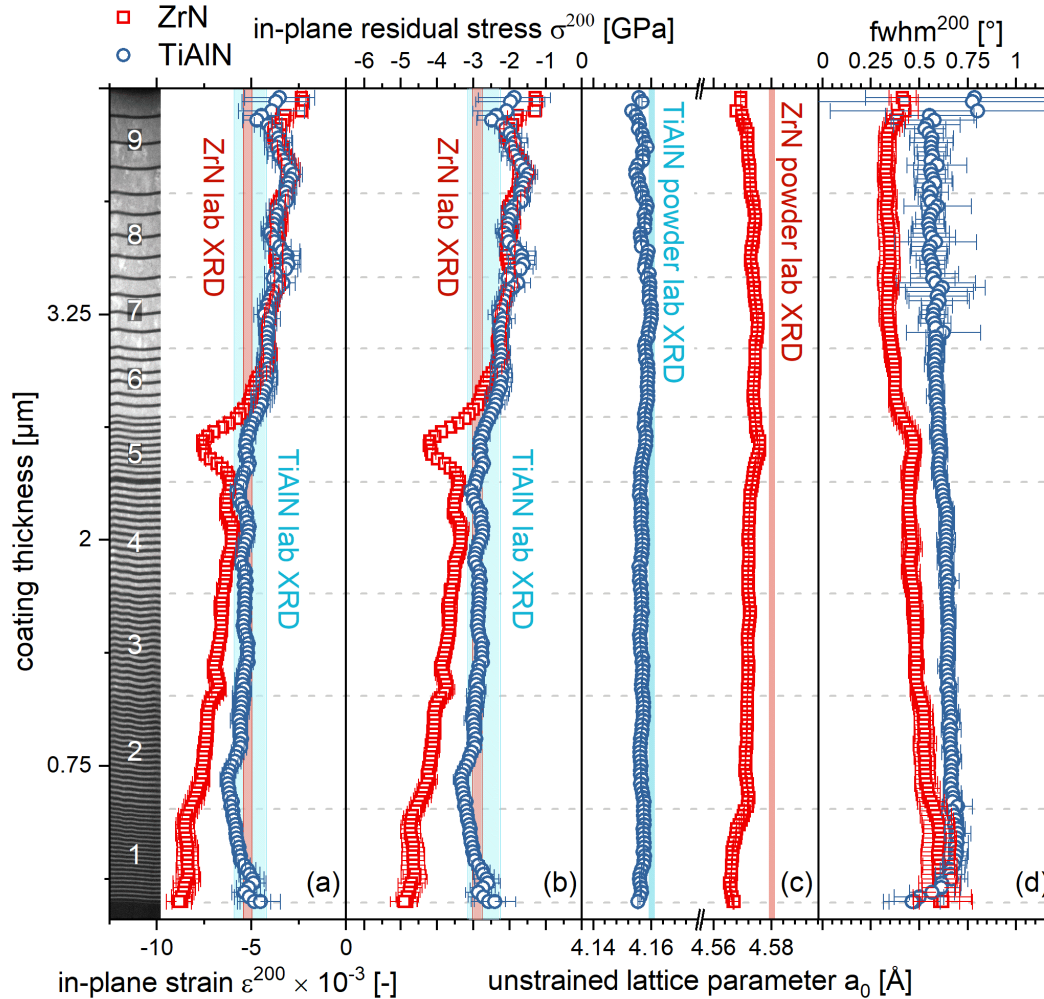
Fig. 5: Evolution of the (a) in-plane strain ε^{200}, (b) in-plane residual stress σ^{200}, (c) unstrained lattice parameter a_0 and (d) full width at half maximum ($fwhm^{200}$) as a function of the coating thickness for the ZrN and $Ti_{0.33}Al_{0.67}N$ layers of the $ZrN/Ti_{0.33}Al_{0.67}N$ multilayer coating, determined by CSnanoXRD. The average residual strain and stress, determined on a laboratory XRD including the standard deviation is also displayed in (a) and (b), respectively. Reference positions for a_0, determined from powdered single-layer ZrN and $Ti_{0.33}Al_{0.67}N$ coatings, are added in (c).

4. Discussion

In the SEM and EBSD images in Figs. 1b and c, as well as in the TEM ADF image in Fig 2a it can be seen that grains grow through the interfaces between the ZrN and $Ti_{0.33}Al_{0.67}N$ layers, showing the formation of heteroepitactic multilayers with

(semi-)coherent interfaces. Furthermore, the texture alignment of ZrN and $Ti_{0.33}Al_{0.67}N$ in Fig. 3b and Fig 4b also corroborates coherency of the multilayers. The <100> fiber texture observed in the XRD pole figures (Fig. 3b) is prevalent throughout the whole coating thickness, as can be seen in the CSnanoXRD texture evaluation (Fig. 4b). This texture develops due to the combination of a low bias voltage and moderate deposition temperature, which favors <100> out-of-plane oriented grains [35,36]. The EBSD band contrast image (Fig. 1c) clearly shows that the grain size increases from the substrate towards the surface with increasing ZrN layer thickness, which is also reflected by a decreasing $fwhm^{200}$ (Fig. 5d). An increasing grain size with increasing bilayer thickness in multilayer coatings was observed by other authors as well [3,4,37,38]. The lattice mismatch of ~9.2 % between ZrN and $Ti_{0.33}Al_{0.67}N$ can be overcome either by a strained interface or by misfit dislocations or a combination thereof. It is suggested that most grains grow (semi-)coherent, due to the isostructurality of the fcc-ZrN and the fcc-TiAlN [8]. Thus, with the increasing number of interfaces also the number of dislocations increases. These interfacial defects are assumed to lead to grain re-nucleation and a smaller grain size [35].

Xu et al. have shown, supported by density functional theory calculations, that the level of coherency increases with the ZrN:TiAlN layer thickness ratio [5]. The driving force behind the formation of coherent interfaces is the minimization of interfacial energy. Usually, the coherency strain energy is high for a lattice mismatch of 9.2 % and the formation of coherent $ZrN/Ti_{0.33}Al_{0.67}N$ multilayers is thermodynamically not stable under equilibrium conditions [5]. However, due to the formation of dislocations at the interface and due to the nonequilibrium deposition process, this strain energy barrier can be overcome and locally coherent interfaces can be stabilized [5]. As the development of semi-coherent interfaces can be assumed in this coating, coherency strain/stress fields develop at the interface that reach several nm into the individual layers, which also influence the in-plane residual strain/stress state in the coating [13]. The main components

contributing to the total residual stress are the thermal ($\sigma_{thermal}$), intrinsic ($\sigma_{intrinsic}$) and extrinsic ($\sigma_{extrinsic}$) stress [39]. $\sigma_{thermal}$ develops during cooling down from the deposition temperature of 425 °C, due to differences in the coefficient of thermal expansion (CTE) between the individual coating layers and between the coating and the substrate material. This contribution is tensile, since the CTEs of ZrN and TiAlN are ~7.2 × 10^{-6} K^{-1} [40] and ~8.1 × 10^{-6} K^{-1} [41], respectively and thus higher than the one of the cemented carbide substrate (~5.7× 10^{-6} K^{-1} [42]) The main contributions to $\sigma_{intrinsic}$ are ion irradiation-induced growth stress and the grain size [39]. The irradiation-induced stress develops due to the ion bombardment of the coating that generates defects during coating growth, leading to a volume increase of the lattice and thus to compressive residual stress [43–45]. The grain size contributes to $\sigma_{intrinsic}$ in a way that a decreasing grain size leads to an increase in the volume fraction of grain boundaries. Since the atoms in the grain boundary are weaker bonded and disordered compared to the atoms inside the grains, adatoms can more easily penetrate into the grain boundary, leading to an increase in the specific grain boundary volume that also increases the compressive residual stress in the grains [39,46]. And finally the relevant contribution of the $\sigma_{extrinsic}$ can be related to structural misfits at the interface, leading to coherency strain/stress [39,46]. The changes in the residual stress state along the cross-section (Fig. 5b) can be attributed to the coating architecture and accompanying changes in the microstructure. The changing bilayer thickness affects the absolute values of the respective stress contributions [47,49]. The in-plane residual stress is similar for the ZrN and Ti$_{0.33}$Al$_{0.67}$N layers for an individual ZrN layer thickness >24 nm (blocks 6-9), which is an indication that the residual stress state in this region mainly depends on the deposition conditions, e.g. $\sigma_{thermal}$ and irradiation-induced residual stress, and coherency strain/stress only plays a minor role. The divergence of the residual strain/stress between ZrN and Ti$_{0.33}$Al$_{0.67}$N in blocks 1-5, however, is assumed to be related to coherency strain/stress. As a result of the larger d-spacing of ZrN compared to Ti$_{0.33}$Al$_{0.67}$N, the ZrN layers are additionally stressed compressively and due to the low

individual ZrN layer thickness of <24 nm the coherency stress cannot relax into the ZrN layer and the layers are dominated by this coherency stress. This leads to an increase in the compressive residual stress in the ZrN layers compared to the $Ti_{0.33}Al_{0.67}N$ layers. As the $Ti_{0.33}Al_{0.67}N$ individual layer thickness is constant, the coherency strain/stress has the same influence on the measured residual strain and stress over the whole thickness.

5. Conclusions

Within this work, a graded $ZrN/Ti_{0.33}Al_{0.67}N$ multilayer coating with constant $Ti_{0.33}Al_{0.67}N$ and stepwise increasing ZrN layer thickness was synthesized by cathodic arc evaporation, in order to study the influence of the individual layer thickness on the microstructure and strain as well as residual stress state. Microstructural investigations by electron backscatter diffraction and transmission electron microscopy revealed an increasing grain size with higher individual ZrN layer thickness and (semi-)coherent growth of the layers. A <100> fiber texture over the whole coating thickness was observed for both, ZrN and $Ti_{0.33}Al_{0.67}N$ phases which further corroborated the (semi-)coherent layer growth. Investigations of the residual stress state by cross-sectional X-ray nanodiffraction showed compressive stress in the range of −5 to −1 GPa for ZrN and −3.5 to −2 GPa for $Ti_{0.33}Al_{0.67}N$. Both phases show declining stresses with increasing ZrN layer thickness, which can mainly be explained by an increasing grain size and thus, a lower density of grain boundaries. Furthermore, ZrN exhibits higher stress than $Ti_{0.33}Al_{0.67}N$ for ZrN layers <24 nm, but nearly identical stress for ZrN layers >24 nm. This effect can be attributed to dominating coherency stress for thinner ZrN layers. The present work contributes to the establishment of a fundamental understanding of the microstructure of a $ZrN/Ti_{0.33}Al_{0.67}N$ multilayer coating and the effect of the bilayer thickness on the residual stress state of the coating.

6. Acknowledgement

7. References

[1]   A. Knutsson, M.P. Johansson, L. Karlsson, M. Odén, Machining performance and decomposition of TiAlN/TiN multilayer coated metal cutting inserts, Surf. Coatings Technol.   205   (2011)   4005–4010. https://doi.org/https://doi.org/10.1016/j.surfcoat.2011.02.031.

[2]   S. Chowdhury, B. Bose, K. Yamamoto, S.C. Veldhuis, Effect of Interlayer Thickness on Nano-Multilayer Coating Performance during High Speed Dry Milling of H13 Tool   Steel,   Coatings.   9   (2019). https://doi.org/https://doi.org/10.3390/coatings9110737.

[3]   F. Frank, C. Kainz, M. Tkadletz, C. Czettl, M. Pohler, N. Schalk, Microstructural and micro-mechanical investigation of cathodic arc evaporated ZrN/TiN multilayer coatings with varying bilayer thickness, Surf. Coatings Technol. 432 (2022) 128070. https://doi.org/10.1016/j.surfcoat.2021.128070.

[4]   C. Kainz, N. Schalk, M. Tkadletz, C. Mitterer, C. Czettl, Microstructure and mechanical properties of CVD TiN/TiBN multilayer coatings, Surf. Coatings Technol. 370 (2019) 311–319. https://doi.org/10.1016/j.surfcoat.2019.04.086.

[5]   Y.X. Xu, L. Chen, F. Pei, K.K. Chang, Y. Du, Effect of the modulation ratio on the interface structure of TiAlN/TiN and TiAlN/ZrN multilayers: First-principles and experimental   investigations,   Acta   Mater.   130   (2017)   281–288. https://doi.org/10.1016/j.actamat.2017.03.053.

[6]   L. Geyang, H. Zenghu, T. Jiawan, X. Junhua, G. Mingyuan, Alternating stress field and superhardness effect in TiN/NbN superlattice films, J. Vac. Sci. Technol. A Vacuum, Surfaces, Film. 20 (2002) 674–677. https://doi.org/10.1116/1.1460887.

[7]   Z. Lei, Y. Liu, F. Ma, Z. Song, Y. Li, Oxidation resistance of TiAlN/ZrN multilayer coatings, Vacuum. 127 (2016) 22–29. https://doi.org/10.1016/j.vacuum.2016.02.004.

[8]   Y.O. Kravchenko, E. Coy, B. Peplińska, I. Iatsunskyi, K. Załęski, M. Kempiǹski, V.M. Beresnev, A. V. Pshyk, A.D. Pogrebnjak, Micro-mechanical investigation of $(Al_{50}Ti_{50})N$ coatings enhanced by ZrN layers in the nanolaminate architecture, Appl. Surf. Sci. 534 (2020). https://doi.org/10.1016/j.apsusc.2020.147573.

[9]   D.J. Li, M. Cao, X.Y. Deng, X. Sun, W.H. Chang, W.M. Lau, Multilayered coatings with alternate ZrN and TiAlN superlattices, Appl. Phys. Lett. 91 (2007) 7–10. https://doi.org/10.1063/1.2826284.

[10]   K. Yalamanchili, F. Wang, H. Aboulfadl, J. Barrirero, L. Rogström, E. Jiménez-Pique, F. Mücklich, F. Tasnadi, M. Odén, N. Ghafoor, Growth and thermal stability of TiN/ZrAlN: Effect of internal interfaces, Acta Mater. 121 (2016) 396–406. https://doi.org/10.1016/j.actamat.2016.07.006.

[11]   L. Chen, Y.X. Xu, L.J. Zhang, Influence of TiN and ZrN insertion layers on the microstructure, mechanical and thermal properties of Cr-Al-N coatings, Surf. Coatings Technol. 285 (2016) 146–152. https://doi.org/10.1016/j.surfcoat.2015.11.033.

[12]   L. Chen, Y.X. Xu, Influence of interfacial structure on the mechanical and thermal properties of CrAlN/ZrN multilayer coatings, Mater. Des. 106 (2016) 1–5. https://doi.org/10.1016/j.matdes.2016.05.082.

[13]   R. Daniel, K.J. Martinschitz, J. Keckes, C. Mitterer, The origin of stresses in magnetron-sputtered thin films with zone T structures, Acta Mater. 58 (2010) 2621–2633. https://doi.org/10.1016/j.actamat.2009.12.048.

[14]   J. Keckes, R. Daniel, J. Todt, J. Zalesak, B. Sartory, S. Braun, J. Gluch, M. Rosenthal, M. Burghammer, C. Mitterer, S. Niese, A. Kubec, 30 nm X-ray focusing correlates

oscillatory stress, texture and structural defect gradients across multilayered TiN-SiO$_x$ thin film, Acta Mater. 144 (2018) 862–873. https://doi.org/10.1016/j.actamat.2017.11.049.

[15] J. Keckes, M. Bartosik, R. Daniel, C. Mitterer, G. Maier, W. Ecker, J. Vila-Comamala, C. David, S. Schoeder, M. Burghammer, X-ray nanodiffraction reveals strain and microstructure evolution in nanocrystalline thin films, Scr. Mater. 67 (2012) 748–751. https://doi.org/10.1016/j.scriptamat.2012.07.034.

[16] N. Schalk, M. Tkadletz, V.L. Terziyska, M. Deluca, I. Letofsky-Papst, J. Keckes, C. Mitterer, Evolution of microstructure and mechanical properties of a graded TiAlON thin film investigated by cross-sectional characterization techniques, Surf. Coatings Technol. 359 (2019) 155–161. https://doi.org/10.1016/j.surfcoat.2018.12.058.

[17] J. Zalesak, M. Bartosik, R. Daniel, C. Mitterer, C. Krywka, D. Kiener, P.H. Mayrhofer, J. Keckes, Cross-sectional structure-property relationship in a graded nanocrystalline Ti$_{1-x}$Al$_x$N thin film, Acta Mater. 102 (2016) 212–219. https://doi.org/10.1016/j.actamat.2015.09.007.

[18] J. Todt, H. Hammer, B. Sartory, M. Burghammer, J. Kraft, R. Daniel, J. Keckes, S. Defregger, X-ray nanodiffraction analysis of stress oscillations in a W thin film on through-silicon via, J. Appl. Crystallogr. 49 (2016) 182–187. https://doi.org/10.1107/S1600576715023419.

[19] M. Meindlhumer, N. Jäger, S. Spor, M. Rosenthal, J.F. Keckes, H. Hruby, C. Mitterer, R. Daniel, J. Keckes, J. Todt, Nanoscale residual stress and microstructure gradients across the cutting edge area of a TiN coating on WC-Co, Scr. Mater. 182 (2020) 11–15. https://doi.org/10.1016/j.scriptamat.2020.02.031.

[20] Indexable inserts for cutting tools - Designation, ISO 1832:2017, 2017. https://standards.iteh.ai/catalog/standards/iso/af10a357-79be-4c54-b963-59800aeb8545/iso-1832-2017.

[21] J. Keckes, J. Todt, M. Meindlhumer, 25 nm X-ray nanodiffraction mapping of residual strain distributions at the cross-sections of a MOSFET transistor, European Synchrotron Radiation Facility (ESRF), 2021. https://doi.org/10.15151/ESRF-ES-452641605.

[22] J. Kieffer, D. Karkoulis, PyFAI, a versatile library for azimuthal regrouping, J. Phys. Conf. Ser. 425 (2013). https://doi.org/10.1088/1742-6596/425/20/202012.

[23] G. Ashiotis, A. Deschildre, Z. Nawaz, J.P. Wright, D. Karkoulis, F.E. Picca, J. Kieffer, The fast azimuthal integration Python library: PyFAI, J. Appl. Crystallogr. 48 (2015) 510–519. https://doi.org/10.1107/S1600576715004306.

[24] M. Stefenelli, J. Todt, A. Riedl, W. Ecker, T. Müller, R. Daniel, M. Burghammer, J. Keckes, X-ray analysis of residual stress gradients in TiN coatings by a Laplace space approach and cross-sectional nanodiffraction: A critical comparison, J. Appl. Crystallogr. 46 (2013) 1378–1385. https://doi.org/10.1107/S0021889813019535.

[25] M. Bartosik, R. Daniel, C. Mitterer, I. Matko, M. Burghammer, P.H. Mayrhofer, J. Keckes, Cross-sectional X-ray nanobeam diffraction analysis of a compositionally graded CrN_x thin film, Thin Solid Films. 542 (2013) 1–4. https://doi.org/10.1016/j.tsf.2013.05.102.

[26] R. Hill, The elastic behaviour of a crystalline aggregate, Proc. Phys. Soc. Sect. A. 65 (1952) 349–354. https://doi.org/10.1088/0370-1298/65/5/307.

[27] V.I. Ivashchenko, P.E.A. Turchi, V.I. Shevchenko, First-principles study of elastic and stability properties of ZrC-ZrN and ZrC-TiC alloys, J. Phys. Condens. Matter. 21 (2009) 395503. https://doi.org/10.1088/0953-8984/21/39/395503.

[28] I.A. Abrikosov, A. Knutsson, B. Alling, F. Tasnádi, H. Lind, L. Hultman, M. Odén, Phase stability and elasticity of TiAlN, Materials (Basel). 4 (2011) 1599–1618. https://doi.org/10.3390/ma4091599.

[29] P.J. Brown, A.G. Fox, E.N. Maslen, M.A. O'Keefe, B.T.M. Willis, Intensity of diffracted intensities, in: Int. Tables Crystallogr., Wiley, Chichester, 2006: pp. 554–595. https://doi.org/10.1107/97809553602060000600.

[30] S. Gates-Rector, T. Blanton, The Powder Diffraction File: A quality materials characterization database, Powder Diffr. 34 (2019) 352–360. https://doi.org/10.1017/S0885715619000812.

[31] C. Kainz, M. Pohler, G.C. Gruber, M. Tkadletz, A. Sophie, C. Czettl, N. Schalk, Influence of bias voltage on microstructure, mechanical properties and thermal stability of arc evaporated $Cr_{0.74}Ta_{0.26}N$ coatings, Surf. Coatings Technol. 417 (2021) 127212. https://doi.org/10.1016/j.surfcoat.2021.127212.

[32] Y. Moritz, C. Kainz, M. Tkadletz, C. Czettl, M. Pohler, N. Schalk, Microstructure and mechanical properties of arc evaporated Ti(Al,Si)N coatings, Surf. Coatings Technol. 421 (2021) 127461. https://doi.org/10.1016/j.surfcoat.2021.127461.

[33] Y. Kim, Y. Cho, S. Hong, S. Bühlmann, H. Park, D.K. Min, S.H. Kim, K. No, Correlation between grain size and domain size distributions in ferroelectric media for probe storage applications, Appl. Phys. Lett. 89 (2006). https://doi.org/10.1063/1.2363942.

[34] W. Cao, C.A. Randall, Grain size and domain size relations in bulk ceramic ferroelectric materials, J. Phys. Chem. Solids. 57 (1996) 1499–1505. https://doi.org/10.1016/0022-3697(96)00019-4.

[35] G. Abadias, Y.Y. Tse, P. Guérin, V. Pelosin, Interdependence between stress, preferred orientation, and surface morphology of nanocrystalline TiN thin films deposited by dual ion beam sputtering, J. Appl. Phys. 99 (2006) 113519. https://doi.org/10.1063/1.2197287.

[36] C. V Thompson, Structure Evolution During Processing of Polycrystalline Films, Annu. Rev. Mater. Sci. 30 (2000) 159–190.

[37] J.M. González-Carmona, J.D. Triviño, Gómez-Ovalle, C. Ortega, J.M. Alvarado-Orozco, H. Sánchez-Sthepa, A. Avila, Wear mechanisms identification using Kelvin probe force microscopy in TiN, ZrN and TiN/ZrN hard ceramic multilayers coatings, Ceram. Int. 46 (2020) 24592–24604. https://doi.org/10.1016/j.ceramint.2020.06.248.

[38] M. Tkadletz, A. Lechner, N. Schalk, B. Sartory, M. Winkler, C. Mitterer, Reactively sputtered TiN/SiO$_2$ multilayer coatings with designed anisotropic thermal conductivity – From theoretical conceptualization to experimental validation, Surf. Coat. Technol. 393 (2020) 125763. https://doi.org/10.1016/j.surfcoat.2020.125763.

[39] R. Daniel, J. Keckes, I. Matko, M. Burghammer, C. Mitterer, Origins of microstructure and stress gradients in nanocrystalline thin films: The role of growth parameters and self-organization, Acta Mater. 61 (2013) 6255–6266. https://doi.org/10.1016/j.actamat.2013.07.009.

[40] H.O. Pierson, Handbook of Refractory Carbides and Nitrides: Properties, Characteristics, Processing and Applications, 1st ed., Noyes Publications, New York, 1996.

[41] M. Bartosik, D. Holec, D. Apel, M. Klaus, C. Genzel, J. Keckes, M. Arndt, P. Polcik, C.M. Koller, P.H. Mayrhofer, Thermal expansion of Ti-Al-N and Cr-Al-N coatings, Scr. Mater. 127 (2017) 182–185. https://doi.org/10.1016/j.scriptamat.2016.09.022.

[42] R. Stylianou, D. Velic, W. Daves, W. Ecker, M. Tkadletz, N. Schalk, C. Czettl, C. Mitterer, Thermal crack formation in TiCN/α-Al$_2$O$_3$ bilayer coatings grown by thermal CVD on WC-Co substrates with varied Co content, Surf. Coatings Technol. 392 (2020) 125687. https://doi.org/10.1016/j.surfcoat.2020.125687.

[43] F.M. D'Heurle, J.M.E. Harper, Note on the origin of intrinsic stresses in films deposited via evaporation and sputtering, Thin Solid Films. 171 (1989) 81–92. https://doi.org/10.1016/0040-6090(89)90035-7.

[44] C.A. Davis, A simple model for the formation of compressive stress in thin films by ion bombardment, Thin Solid Films. 226 (1993) 30–34. https://doi.org/10.1016/0040-6090(93)90201-Y.

[45] G. Abadias, E. Chason, J. Keckes, M. Sebastiani, G.B. Thompson, E. Barthel, G.L. Doll, C.E. Murray, C.H. Stoessel, L. Martinu, Review Article: Stress in thin films and coatings: Current status, challenges, and prospects, J. Vac. Sci. Technol. A Vacuum, Surfaces, Film. 36 (2018) 020801. https://doi.org/10.1116/1.5011790.

[46] R. Daniel, D. Holec, M. Bartosik, J. Keckes, C. Mitterer, Size effect of thermal expansion and thermal/intrinsic stresses in nanostructured thin films: Experiment and model, Acta Mater. 59 (2011) 6631–6645. https://doi.org/10.1016/j.actamat.2011.07.018.

[47] R. Ali, M. Sebastiani, E. Bemporad, Influence of Ti-TiN multilayer PVD-coatings design on residual stresses and adhesion, Mater. Des. 75 (2015) 47–56. https://doi.org/10.1016/j.matdes.2015.03.007.

[48] S. Spor, N. Jäger, M. Meindlhumer, H. Hruby, M. Burghammer, F. Nahif, C. Mitterer, J. Keckes, R. Daniel, Evolution of structure, residual stress, thermal stability and wear resistance of nanocrystalline multilayered $Al_{0.7}Cr_{0.3}N$-$Al_{0.67}Ti_{0.33}N$ coatings, Surf. Coatings Technol. 425 (2021) 127712. https://doi.org/10.1016/j.surfcoat.2021.127712.

[49] N. Jäger, S. Klima, H. Hruby, J. Julin, M. Burghammer, J.F. Keckes, C. Mitterer, R. Daniel, Evolution of structure and residual stress of a fcc/hex-AlCrN multi-layered system upon thermal loading revealed by cross-sectional X-ray nano-diffraction, Acta Mater. 162 (2019) 55–66. https://doi.org/10.1016/J.ACTAMAT.2018.09.031.

"For the Quest is achieved, and now all is over. I am glad you are here with me. Here at the end of all things, Sam."

Frodo Baggins in The Lord of the Rings by J.R.R. Tolkien.